STRUCTURES AND THERMAL BEHAVIOUR OF SOME MONOOXALATO AND DIOXALATO METAL COMPLEXES

Submitted in fulfilment
of the requirements of the
degree of Master of Science
of RHODES UNIVERSITY

by
JOHN BACSA

July 1995

Acknowledgements

I would like to express my gratitude to my two supervisors, Professors M.E. Brown and D.J. Eve for the help, advice and encouragement that they have given me during the project. I would also like to express my appreciation to:

The late Dr R.B. English for his help with the X-ray crystallographic studies.

Dr D. Levendis, Department of Chemistry, University of the Witwatersrand, for help with plotting the molecular structures.

Dr P.S. White, Department of Chemistry, University of New Brunswick, Canada for the UNIX version of NRC VAX.

Mrs Erika Bacsa, for tracing and stencilling various diagrams.

CONTENTS

Abstract

The crystal structure of $Ba[Cu(C_2O_4)_2(H_2O)].5H_2O$ has been determined using single crystal X-ray diffractometry. It crystallises in the triclinic system, space group $P\bar{1}$, with a = 6.539(2) Å, b = 9.211(3) Å, c = 10.928(3) Å, α = 85.42(3)°, β = 79.22(3)°, γ = 80.30(3)°, V = 636.08(8) Å^3 and Z = 2. The structure consists of $[Cu(C_2O_4)_2(H_2O)]^{2-}$ ions weakly bridged by barium ions and water molecules. The copper(II) ions are in a tetragonally elongated square-pyramidal environment with some trigonal distortion. The two oxalate groups occupy the equatorial positions and a water molecule occupies the axial position. The barium ion is surrounded by nine oxygens: five oxygens from water molecules and four oxygens from oxalate groups.

The thermal behaviour of $Ba[Cu(C_2O_4)_2(H_2O)].5H_2O$ in N_2 has been examined using thermogravimetry (TG) and differential scanning calorimetry (DSC). The dehydration starts at relatively low temperatures (~80°C), but continues until the onset of the decomposition (~280°C). The decomposition takes place in two major stages. The mass of the intermediate after the first stage corresponded to the formation of barium oxalate and copper metal and, after the second stage, to the formation of barium carbonate and copper metal. The enthalpy for the dehydration was found to be 311 ±30 kJ mol^{-1}. The overall enthalpy change for the decomposition of $Ba[Cu(C_2O_4)_2]$ in N_2 was estimated from the combined area of the peaks of the DSC curve as -347 kJ mol^{-1}.

The kinetics of the thermal dehydration and decomposition were studied using isothermal TG. The dehydration was strongly deceleratory and the α-time curves could be described by the three-dimensional diffusion (D3) model. The values of the activation energy and the pre-exponential factor for the dehydration were 125 ±4 kJ mol^{-1} and (1.38 ±0.08)x10^{15} min^{-1}, respectively. The decomposition was complex, consisting of at least two concurrent processes. The decomposition was analysed in terms of two overlapping deceleratory processes. One process was fast and could be described by the contracting-geometry model with n = 5. The other process was slow and could also be described by the contracting-geometry model, but with n = 2.

The values of E_a and A were 206 ±23 kJ mol^{-1} and (2.2 ±0.5)x10^{19} min^{-1}, respectively, for the fast process, and 259 ±37 kJ mol^{-1} and (6.3 ±1.8)x10^{23} min^{-1}, respectively, for the slow process.

The crystal structure of zinc oxalate dihydrate ($[Zn(C_2O_4)(H_2O)_2]_n$) has also been determined by X-ray diffraction methods. It crystallises in the monoclinic system, space group $C2/c$ with a = 11.786(2) Å, b = 5.397(1) Å, c = 9.712(1) Å, β = 126.19(5)°, V = 498.58(8) Å^3, Z = 4 and R = 0.037 for 435 absorption-corrected independent reflections and 50 parameters. The asymmetric unit consists of half the monomeric unit $[Zn(C_2O_4)(H_2O)_2]$. The structure consists of infinite, linear chains of zinc ions bridged by oxalate groups. The geometry of the coordination polyhedron surrounding the zinc ion is octahedral, with the oxalate oxygens occupying the equatorial positions and water molecules occupying the axial positions.

LIST OF FIGURES

LIST OF TABLES

CHAPTER 1

INTRODUCTION

1.1 Aims of this research

The thermal stability of solid materials is of great importance and theoretical interest. The research described in this thesis is an attempt to extend the quantitative information available on the structural and other factors which determine thermal stability, through examination and comparison of the structures and thermal behaviour of some metal oxalates and oxalato complexes.

1.2 Structure and reactivity

A longstanding goal of solid state chemistry has been to determine relationships, wherever possible, between the crystal structures and the reactions of solids. Establishment of such relationships has not been simple since many factors which influence the reactivity of solids are generally non-typical of the bulk structures. Information on the presence and role of crystal imperfections is generally not accessible by X-ray diffraction methods, which average the information available over a vast number of structural units.

One of the most convenient measures of the reactivity of a solid is its thermal behaviour, studied either under the programmed temperature conditions of thermal analysis, or at selected isothermal temperatures. Much detailed information on the subject has been obtained through studies of the thermal dehydration of crystalline hydrates. The thermal decompositions of metal salts of the oxalates have also provided a means of comparing the influence of the metal ion on the decomposition. Such comparisons are not straightforward, since, as discussed below, these salts can take up several different crystal structures. In addition, these structures may include various proportions of crystal water and this water is generally lost in dehydration processes which precede the decomposition processes.

Many of the metal oxalates have been subject to detailed kinetic analysis and the results have been used in establishing the theoretical concepts applicable to solid state reactions.

Since the majority of these compounds are insoluble in water, crystals suitable for X-ray structure determination are difficult or impossible to prepare. Therefore detailed, accurate, information of the crystal structures of most of these compounds is not available, so structure-reactivity relationships have been limited and a possible solution to this problem has been the preparation of the mixed metal oxalates [1] where one metal is varied to give a range of similar compounds expected, under ideal circumstances, to vary in thermal behaviour due to the influence of the second metal. Oxalate complexes are generally classified with respect to the number of oxalate groups coordinated to the metal ion. The majority of the thermal studies, up to now, have been of the monooxalato complexes and dioxalato complexes of divalent metal ions.

In the literature the monoxalato complexes are usually referred to as the metal oxalates and the dioxalato complexes as oxalato complexes. However, both the monooxalates and the dioxalates can be treated as coordination complexes.

1.3 A review of the structures of some monooxalato complexes of divalent metal ions

1.3.1 The structures of $[M(C_2O_4)(H_2O)_2]_n$, M = Mg, Mn, Fe, Co, Ni, and Zn

The structure of the mineral humboldtine $[Fe(C_2O_4)(H_2O)_2]_n$ was solved by Caric [2]. Humboldtine crystallises in the monoclinic system, space group *C2/c*. Powder diffraction data shows that the other oxalates of this group also crystallise in this space group but with slightly different lattice parameters [3]. The structure of zinc oxalate dihydrate was found to be isostructural with humboldtine and is discussed in detail further on in this research project. A brief description of the structure of humboldtine will be given here. Humboldtine consists of infinite, linear chains of $[Fe(C_2O_4)(H_2O)_2]$ units with bridging oxalate groups. These chains lie along 2-fold symmetry axes, parallel to the *b*-axis, and are planar within experimental error (Figure 1.1).

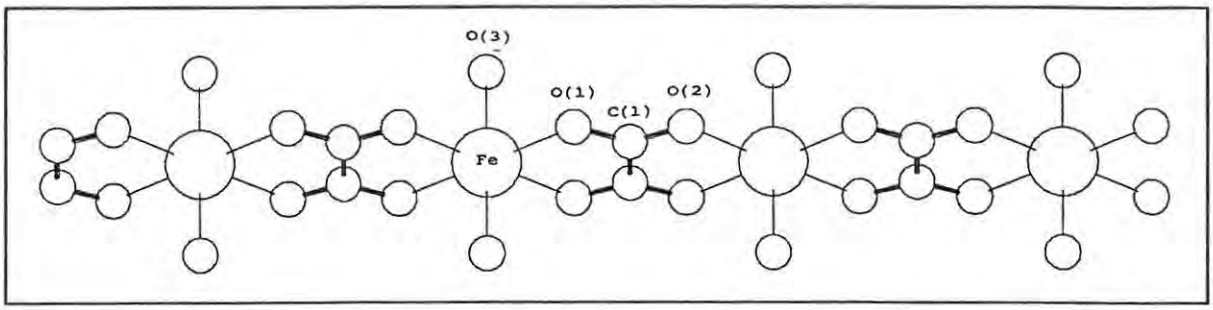

Figure 1.1 A portion of the bonding structure of humboldtine

The coordination geometry of the metal ions in humboldtine is almost perfectly octahedral, all of the bond angles are close to the octahedral values and the metal-oxygen bond lengths are very similar. All the carbon-oxygen bond lengths are identical. Since the other oxalates of this group produce similar diffraction patterns, and have nearly identical lattice parameters it is assumed that their bonding pattern is nearly identical, but with slightly different bond lengths.

1.3.2 The structure of copper(II) oxalate, $CuC_2O_4.xH_2O$, x = 0 to 1

The powder diffraction pattern of copper oxalate is different from the patterns of the oxalates of the group described above. Since single crystals suitable for X-ray analysis have not been prepared, unambiguous detailed information of the bonding structure of copper oxalate does not exist. However, there is strong evidence [4,5] to support a model structure which consists of infinite chains of $[Cu(C_2O_4)]$ units following a particular crystallographic direction. The antiferromagnetic properties are consistent with a linear chain structure bridged by oxalate ligands. The oxalate ion is now known as one of the most effective ligands in transmitting magnetic effects.

The XRD pattern of copper(II) oxalate is difficult to interpret. One peak in the diffraction pattern is much stronger than the others, and therefore might contain several reflections gathered together. Most of the other bands are weak and diffuse. The X-ray powder diffraction pattern of copper oxalate has been indexed by Schmittler [6] using an orthorhombic cell with a = 5.35, b = 5.63, c = 2.56 Å and one formula unit per unit cell.

A structure consistent with these dimensions consists of copper(II) ions at the corner of each unit cell, and linear chains of $[Cu(C_2O_4)]$ units following the *b*-axis. Because the cell is orthorhombic, the copper(II) ions would be stacked directly above each other, along the *c*-axis. This structure is unlikely to be the correct structure since there would be significant repulsion between the copper(II) ions along the *c*-axis and a lack of van der Waals contacts between the linear chains. It is thus likely that the authors have mistakenly deduced that copper(II) oxalate has an orthorhombic cell with these dimensions.

Gliezes and coworkers [7] deduced a model structure for copper oxalate by applying the crystallographic shear operation 1/4 [-1 2 -1](0 1 0), of periodicity *b*, to the structure of $Na_2[Cu(C_2O_4)_2].2H_2O$. This operation removes the Na^+ ions and one out of every two water molecules, and creates linear chains of $[Cu(C_2O_4)]_n$ units. These chains are stacked in such a way that the coordination geometry of the copper(II) ions is elongated-octahedral, with the oxygen atoms from neighbouring chains occupying the axial positions of the copper(II) coordination sphere. The predicted copper-copper separation in this structure (5.16 Å) is close to the copper-copper separation determined by EXAFS studies (5.14 Å) [7]. Further removal of water molecules would lead in the limit to the structure of anhydrous copper(II) oxalate in which the linear chains are held together by van der Waals contacts between the oxygen atoms. The resulting model structure of anhydrous copper oxalate is shown in Figure 1.2.

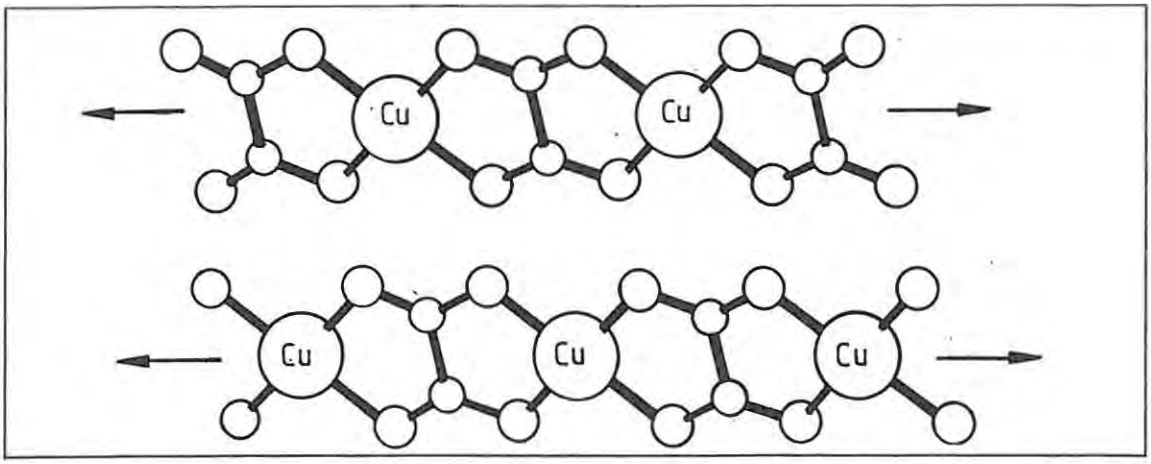

Figure 1.2 A proposed structure of anhydrous copper(II) oxalate viewed along the stacking direction

Copper oxalate, however, exists neither as a monohydrate nor as an anhydrous compound. There are small, non-stoichiometric amounts of water its lattice. Samples of copper oxalate are poorly crystallised which may be a result of the non-stoichiometric water which would prevent the chains from packing together properly [7].

There are programs available which could be used to produce a theoretical powder diffraction pattern from the model structure proposed by Gliezes and coworkers. If the calculated powder pattern turns out to be similar to the observed powder pattern, then this structure is likely to be the correct structure and it then could be refined by minimising the differences in the observed pattern and calculated pattern by a least squares method.

1.3.3 The structures of the mixed metal copper oxalates, $MCu(C_2O_4)_2.3H_2O$, M = Fe, Co, and Ni

The complexes $MCu(C_2O_4)_2.3H_2O$, were prepared by dropwise addition of dilute aqueous solutions of the soluble metal salt to an aqueous solution of an equimolar quantity of dioxalato copper(II) ($[Cu(C_2O_4)_2]^{2-}(aq)$) [1]. The X-ray powder diffraction patterns of these oxalates, and hence their crystals structures, were similar to those of the oxalates $[M(C_2O_4)(H_2O)_2]_n$ and different to that of copper oxalate, $CuC_2O_4.xH_2O$. Thus the coordination of the metal ion, M^{2+}, is same as the parent metal

oxalate, and the copper(II) ion is likely to be pentacoordinate, the axial position being occupied by the third water molecule.

XPS (X-ray photoelectron spectroscopy) showed that the electron density surrounding the copper(II) ion increased in the following order: $NiCu(C_2O_4)_2.3H_2O$, CuC_2O_4, $CoCu(C_2O_4)_2.3H_2O$, $FeCu(C_2O_4)_2.3H_2O$

Since the metal ion, M^{2+} affected the environment of the copper ion, it is likely that the metal ions in the mixed metal copper oxalates are mixed at a molecular level. These complexes decompose at relatively low temperatures to produce mixed oxides and, hence, could be useful precursors for the preparation of binary mixed metal oxides related to superconductors.

1.4 The structures of dioxalato complexes of divalent transition metal ions

The dioxalato complexes of divalent transition metal ions can be formulated as $A_x[M(C_2O_4)_2(H_2O)_y].zH_2O$ where A = NH_4^+, or a Group I or II cation and M = transition metal ion. There are several important structural differences between the monooxalato complexes and the dioxalato complexes, the main difference being the mode of coordination of the oxalate ligand. The oxalate ion in the dioxalato complexes usually acts as a bidentate non-bridging ligand whereas in the monooxalato complexes it acts as a quadridentate bridging ligand. The monooxalates, $[M(C_2O_4)(H_2O)_2]_n$, are therefore polynuclear complexes and the dioxalato complexes are usually mononuclear complexes. Two distinct types of carbon-oxygen bonds can be observed in the dioxalato complexes: carbon-oxygen single bonds and carbon-oxygen double bonds, whereas only one distinct type of carbon-oxygen bond is observed in the monooxalates, corresponding to a hybrid of a double and a single bond. The water present in the crystals of the monooxalato complexes is usually coordinated to the metal ion. In dioxalato complexes the water is present as crystal water or a combination of crystal water and coordinated water. The dioxalato complexes exhibit a wide variation in their crystal structures. When one considers the structures of these compounds the importance of the size of the cation, A emerges. The size

influences the packing of the dioxalato units and the degree of hydration of these compounds. If the cation, A, is small (e.g. A = Na^+), the crystal usually consists columnar chains of dioxalato units stacked above one another (Figure 1.3).

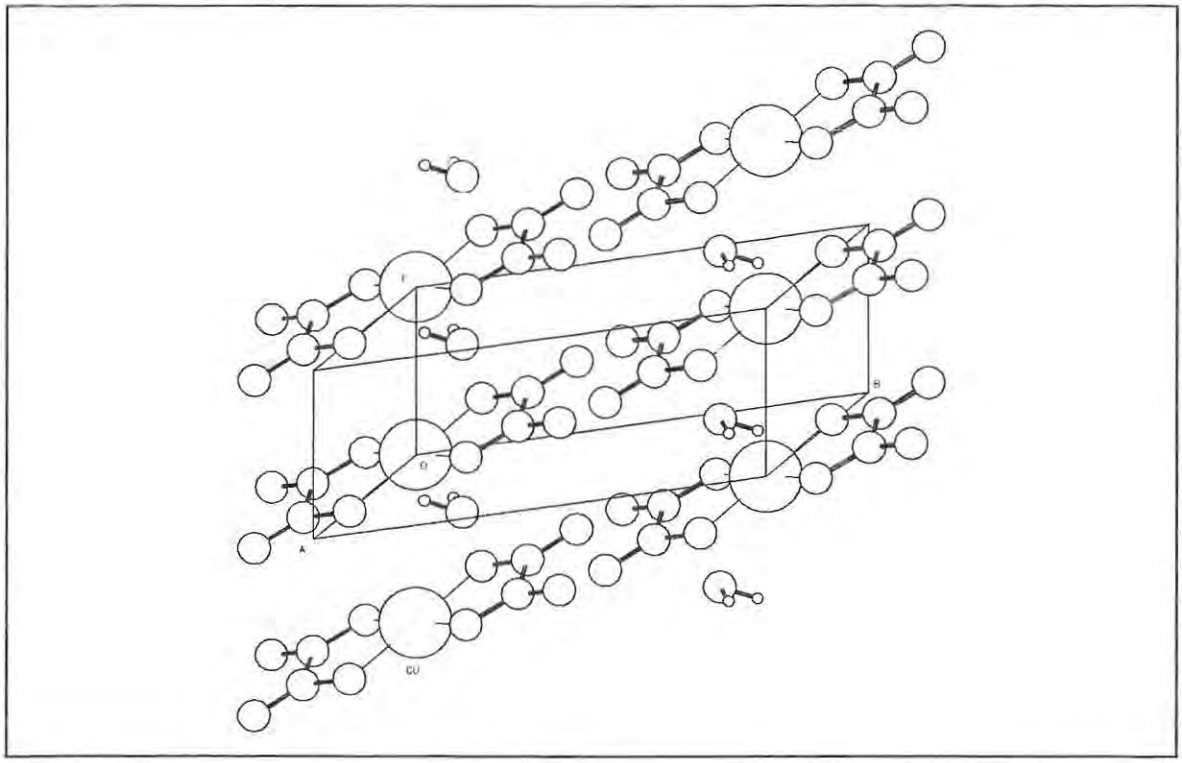

Figure 1.3 The stacking of the $Cu(C_2O_4)_2^{2-}$ units in $Na_2[Cu(C_2O_4)_2].2H_2O$

If the cation, A, is large (e.g. K^+, Cs^+, Sr^{2+}, Ba^{2+}, NH_4^+), the stacking of the dioxalato ions is inhibited and different arrangments are observed.

1.4.1 The structure of dioxalato complexes of copper(II)

The structures of $K_2[Cu(C_2O_4)_2].2H_2O$ and $(NH_4)_2[Cu(C_2O_4)_2].2H_2O$ have long been known [8]. $K_2[Cu(C_2O_4)_2].2H_2O$ and $(NH_4)_2[Cu(C_2O_4)_2].2H_2O$ are isostructural. The unit cell contains two non-equivalent dioxalato copper(II) units. Unlike $Na_2[Cu(C_2O_4)_2].2H_2O$ the dioxalato units are not stacked above each other. The crystal structure of $Na_2[Cu(C_2O_4)_2].2H_2O$ has been refined using single crystal X-ray data until a final *R* factor of 2.7% was obtained [7] and its bond lengths and angles are known to a great degree of precision. An illustration of the

structure viewed parallel to the *c*-axis is shown in Figure 1.4.

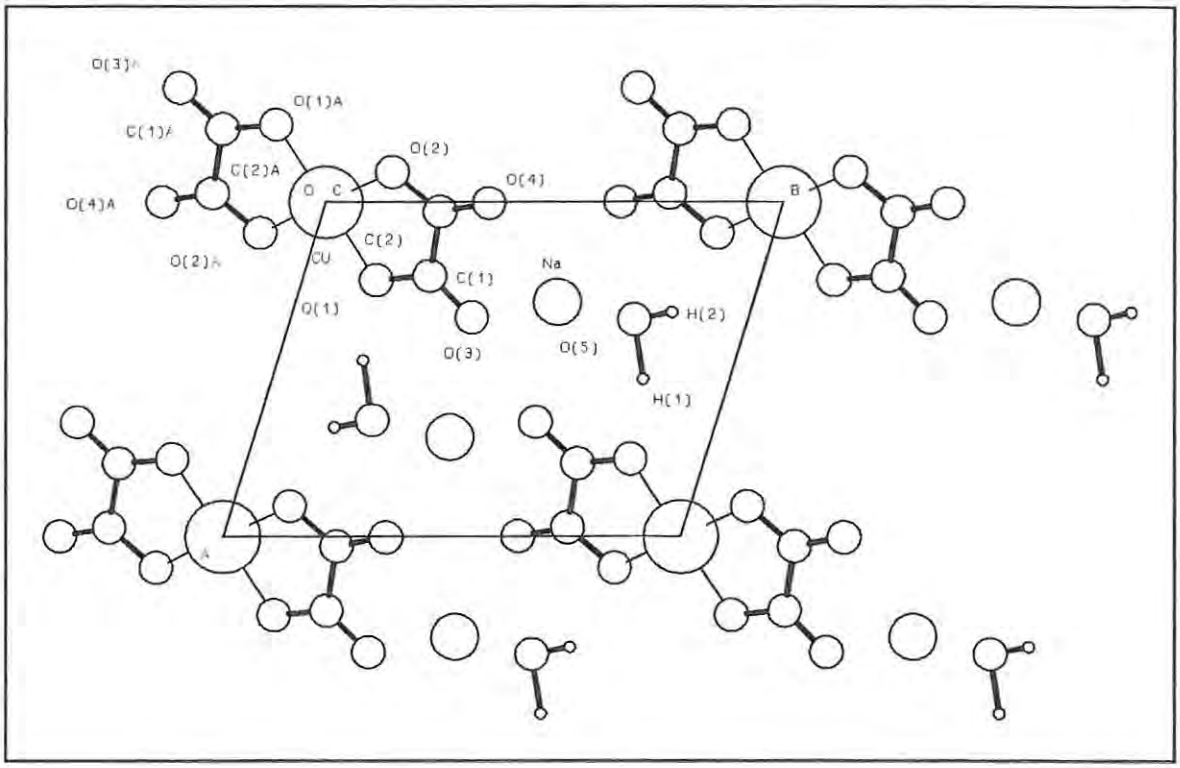

Figure 1.4 The structure of $Na_2[Cu(C_2O_4)_2].2H_2O$ viewed along the *c*-axis

The structure is made up of columnar stacks of planar $Cu(C_2O_4)_2^{2-}$ units. The columns follow the the *c*-axis. The water molecules bridge the $Cu(C_2O_4)_2^{2-}$ units via hydrogen bonds. Thus the structure contains infinite chains of $[Cu(C_2O_4)_2\ (H_2O)_2]$ units which follow the *a*-axis.

The copper(II) ion of the $Cu(C_2O_4)_2^{2-}$ anion lies at a centre of symmetry and consequently the asymmetric unit contains half the dioxalato unit, i.e. one oxalate group and two equatorial copper-oxygen bonds. The two independent equatorial copper-oxygen bonds are almost identical: 1.929(1) and 1.930(1) Å. In addition to the equatorial bonds the axial coordination sites of the copper(II) ion are occupied by the oxygen atoms from neighbouring units stacked above and below the copper(II) ion. The axial copper-oxygen bond distances are both equal to 2.803(2) Å. The axial copper-oxygen bonds are not perpendicular to the plane defined by the four equatorial copper oxygen bonds but are

tilted at an angle of 8°. The independent oxalate group of the dioxalato unit contains two pairs of carbon-oxygen bonds: those which coordinate to the copper(II) ion and those which do not. The two carbon-oxygen bonds which coordinate to the copper(II) ions are longer (1.279(2) and 1.286(2) Å) than those which do not (1.220(2) and 1.225(2) Å). The lengths of the carbon-oxygen bonds which do not coordinate are the standard values for carbon-oxygen double bonds but the remaining carbon-oxygen bonds are appreciably shorter than the standard C-O single bond length.

The sodium ion is surrounded by seven oxygen atoms: two from water molecules and four from oxalate groups. The NaO_7 coordination polyhedron has the geometry of an irregular monocapped trigonal prism. The sodium-oxygen distances range from 2.37 to 2.59 Å.

1.5 A review of the thermal behaviour of some oxalato complexes of divalent metals

1.5.1 The thermal dehydrations of $[M(C_2O_4)(H_2O)_2]_n$

Previous work on the thermal dehydration of these oxalates is reviewed below and the relationships between the crystal structures and the dehydration mechanisms are examined.

The crystal structures of these compounds are isomorphous, so the mechanisms which describe the thermal dehydrations could be expected to be similar.

The kinetics of the isothermal dehydration of $[Mg(C_2O_4)(H_2O)_2]_n$ have been studied in detail by Masuda and coworkers [10]. The two-dimensional phase boundary rate law (R2) was found to give a good description of the kinetics of this reaction. At low temperatures, the dehydration is affected by the nucleation process, and the α-time curves shows slightly sigmoidal character, so that the R2 model does not describe the dehydration during the initial period.

The isothermal dehydrations of $[Fe(C_2O_4)(H_2O)_2]_n$ and $[Ni(C_2O_4)(H_2O)_2]_n$, as well as of the mixed oxalates $FeCu(C_2O_4)_2.3H_2O$, $CoCu(C_2O_4)_2.3H_2O$ and $NiCu(C_2O_4)_2.3H_2O$, have been studied recently by Coetzee and coworkers [11]. The dehydrations

of these oxalates were also found to proceed as two-dimensional phase boundary reactions.

The kinetics of the non-isothermal dehydration of $[Co(C_2O_4)(H_2O)_2]_n$ are reported to obey the first-order rate law (F1) [11]. However it is difficult to distinguish the first-order rate law from the two-dimensional phase boundary rate law (R2), especially from non-isothermal data. Isothermal runs could well show that the two-dimensional phase boundary model is more applicable. The kinetic parameters for the isothermal dehydrations of these oxalates are set out in Table 1.1 for comparison.

Table 1.1 The activation energies and pre-exponential factors for the isothermal dehydration of the oxalates $[M(C_2O_4)(H_2O)_2]_n$ and $MCu(C_2O_4)_2.3H_2O$

Oxalate	Model	E_a/kJ mol^{-1}	A/s^{-1}	Ref
$[Mg(C_2O_4)(H_2O)_2]_n$	R2	11	3.4×10^9	[10]
$[Ni(C_2O_4)(H_2O)_2]_n$	R2	68	1.8×10^4	[11]
$[Fe(C_2O_4)(H_2O)_2]_n$	R2	87	1.5×10^7	[11]
$FeCu(C_2O_4)_2.3H_2O$	R2	90	5.5×10^{14}	[11]
$CoCu(C_2O_4)_2.3H_2O$	R2	109	1.1×10^{17}	[11]
$NiCu(C_2O_4)_2.3H_2O$	R2	101	8.4×10^{14}	[11]

Since the dehydrations of these oxalates are generally best described by the contracting area rate law (R2), the following generalisations can be made about the dehydrations of the oxalates, $[M(C_2O_4)(H_2O)_2]_n$:

1) The diffusion of water molecules through the product layer is so rapid that it does not affect the overall rate of the dehydration.

2) The rate determining step in the dehydration is the advance of the reactant/product interface through the crystal.

3) The movement of the reactant/product interface is more accurately described as a contracting-area (two-dimensional

model) than a contracting-volume (three-dimensional model). Thus the reaction interface moves preferentially along certain crystallographic planes. Various stages of the dehydration of magnesium oxalate dihydrate have been observed by optical microscopy by Masuda and coworkers [10]. The optical micrographs showed that the crystals of $[Mg(C_2O_4)(H_2O)_2]_n$ had perfect cleavage planes parallel to the (1 0 0) planes. The nuclei appear on the edges and along the cleavage planes. The nuclei grow until an interface builds up, and then the interface moves towards the centre of the surface. They also observed, from consideration of its crystal structure, that the water molecules lie on planes parallel or along the cleavage planes. It is reasonable to assume that the dehydration takes place on these planes. The studies by Masuda [10] and the crystal structure reported by Caric [2] are important observations that may be relevant to the dehydration routes.

4) Nucleation processes generally occur so rapidly that they do not affect the overall rate of the reaction. At low temperatures, however, nucleation processes can become rate determining during the initial period of the dehydration [10].

Since the water molecules of these oxalates are directly bonded to the metal ions, the enthalpies and onset temperatures for the thermal dehydrations are likely to depend on the strength of the metal-oxygen(water) bond. If the bonding is purely ionic, the relative strength of the metal-oxygen(water) bond will depend on the size of the metal ion. The ionic radii of these metal ions decrease in the following order [12]:

Zn^{2+}(0.75 Å), Mg^{2+}(0.72 Å), Ni^{2+}(0.70 Å), Mn^{2+}(0.67 Å), Co^{2+}(0.65 Å), Fe^{2+}(0.61 Å)

Transition metal ions, however, have vacant d-orbitals, so covalent interactions are also likely to be important in determining the strength of the metal-oxygen bond. The ligand field splitting energy, obtained from electronic spectra, is the difference in energy between the highest energy bonding orbitals (t_{2g}) and the lowest energy antibonding orbitals (e_g^*) of the transition metal ion. The ligand field splitting energy is thus assumed to be a measure of the relative amount of covalent

bonding in these complexes. Since the occupation of the outer orbitals varies in the transition metal oxalates, an increase in the ligand field splitting energy does not necessarily mean an increase in the contribution of covalent interactions to the overall metal-oxygen bond energy. The magnitude of the ligand field stabilisation energy (LFSE) increases in the following order:

Zn^{2+}, Mn^{2+}, Fe^{2+}, Co^{2+}, Ni^{2+}

The onset temperatures and enthalpies for these oxalates increases in the following order (data for $[Mn(C_2O_4)(H_2O)_2]_n$ were not available) [1]:

Fe^{2+}, Zn^{2+}, Co^{2+}, Ni^{2+}

There thus appears to be no simple correlation between the LFSE, ionic radii and the dehydration of these complexes.

1.5.2 The thermal dehydration of $K_2[Cu(C_2O_4)_2].2H_2O$

The thermal dehydration of $K_2[Cu(C_2O_4)_2].2H_2O$ has been studied using isothermal and non-isothermal TG [13]. The dehydration of $K_2[Cu(C_2O_4)_2].2H_2O$ was found to take place in one step. The individual particles retained their original shape throughout the dehydration, but underwent a change from clear, blue, translucent crystals to darker, opaque particles. The kinetics of the dehydration were studied using isothermal TG at temperatures between 75 and 90°C. The α-time curves were sigmoidal, and the Avrami-Erofeev equation with $n = 2$ generally gave the best fits. The rate constants, from the Avrami-Erofeev equation yielded E_a = 116 kJ mol^{-1} and $A = 1.12 \times 10^{16}$ min^{-1}.

1.5.3 Thermal decomposition of divalent transition metal oxalates

The first step in the decomposition of all metal oxalates has been proposed to be the rupture of the carbon-carbon bond [14]. Once the carbon-carbon bond breaks, the oxalate ion can rearrange in three different ways [11]:

1) $2CO_2^- \rightarrow 2CO_2 + 2e$

2) $2CO_2^- \rightarrow [OCOCO_2]^{2-} \rightarrow CO_3^{2-} + CO$

3) $2CO_2^- \rightarrow [OCOCO_2]^{2-} \rightarrow O^{2-} + CO + CO_2$

The preferred mechanism of the rearrangment of the oxalate ion in the metal oxalates will depend on the ionisation potential of the metal ion relative to the oxalate ion, the ionic radius of the metal ion and electronic effects such as d-orbital participation. Route (1) is associated with the reduction of the metal ion to the metallic state. Therefore route (1) will not be associated with the alkali, and alkali earth metal ions since these ions are extremely difficult to reduce but is often associated with the transition metals since they are easier to reduce. Routes (2) and (3) occur without reduction of the metal ion. The Group II metals tend to form carbonates, whereas the transition metals (if not reduced) form oxides.

The electronic interaction between the carboxylate groups of the oxalate anion and the metal cation is thought have an important influence on the temperatures for the onset of the oxalate decomposition. The electronic repulsion between the two carboxylate groups of the oxalate anion weakens its carbon-carbon bond. Electronic interactions between the metal ion and the oxalate ligand remove some of the negative charge present on the carboxylate groups, thereby reducing the repulsion. The least repulsion will occur when the electronic interactions between the metal and the oxalate ions are at a maximum. Since the first step in the decompositions of all oxalates is proposed to be the rupture of the C-C bond, higher temperatures for the onset of decomposition can be expected for metal oxalates with strong electronic interaction between the metal ion and the oxalate ligand. The amount of electronic interaction in the ionic metal oxalates depends on the size of the metal ion and the sum of the ionisation potentials for the metal atom. Quantitative relationships linking these quantities with the onset temperatures for the decompositions of ionic oxalates have been proposed [15]. Transition metal oxalates show substantial electron delocalisation as a result of d-orbital participation and quantitative relationships linking the properties of the metal ion with the decomposition onset temperatures for transition metal oxalates have not been determined.

The C-C bond in oxalate groups

Since the feature common to the decomposition of metal oxalates is the rupture of the C-C bond, it is worthwhile to examine the C-C bond in oxalates. The structure of oxalic acid has been extensively studied using X-ray and neutron diffraction techniques [16] and the bond angles and lengths are known to a great degree of precision. The bond lengths and bond angles of the oxalic acid molecule are shown in Figure 1.5.

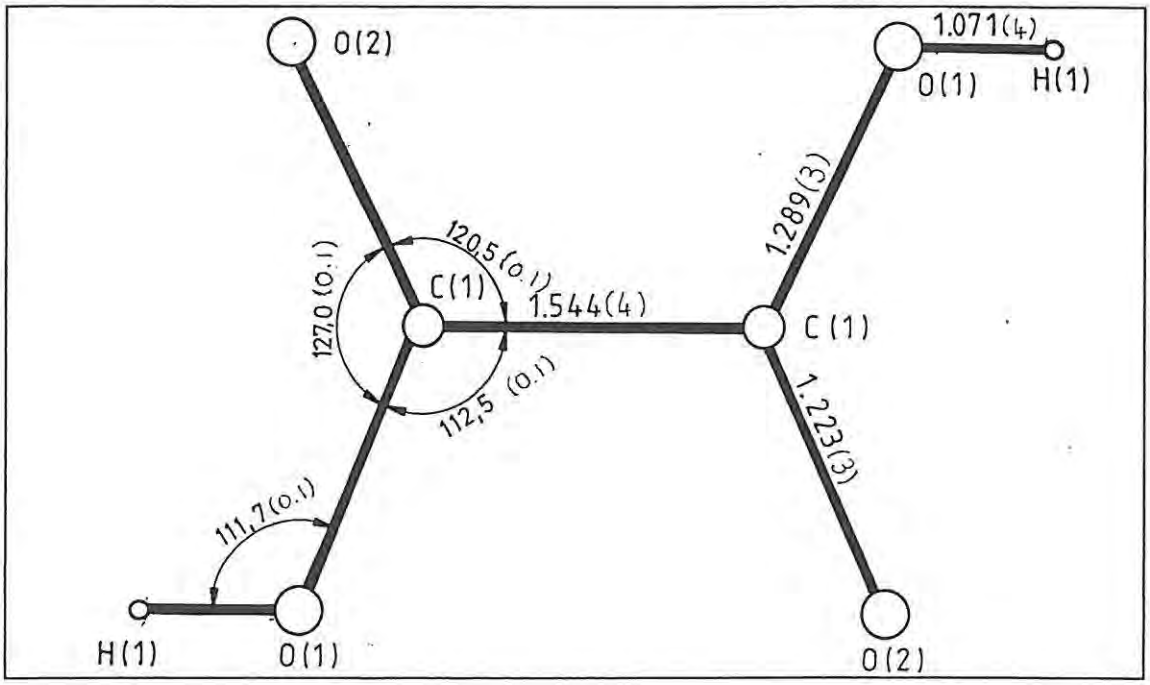

Figure 1.5 The bond lengths (Å) and angles (°) of the oxalic acid molecule

The oxalic acid molecule is planar which suggests the existence of delocalised π-bonding. Deformation density studies of oxalic acid [16] have shown that the C-C bond has significant π-character. The final difference electron density maps revealed a significant electron density maximum at the centre of the carbon-carbon bond, elongation of this peak indicates that the C-C bond has significant π-character. On the other hand, the length of the C-C bond is 1.544(4) Å, which is substantially longer than the normal C-C single bond found in aliphatic compounds [17]. The bond order of the C-C bond of oxalic acid has been computed [18]. The π-orbitals were found to make a

small contribution to the strength of the C-C bond. The bond order of C-C bond is 0.831, of which 98% is due to σ-overlap and 2% is due to π-overlap. This low bond order has been attributed to the presence of the electronegative oxygen atoms, which reduces some of the σ-bonding electron density of the C-C bond and transfers it into the orbitals of the C-O groups. In most oxalato-complexes the oxalate species exists in the dianionic or dibasic form. The dimensions and bond angles of the oxalate ion of zinc oxalate dihydrate are shown in Figure 1.6.

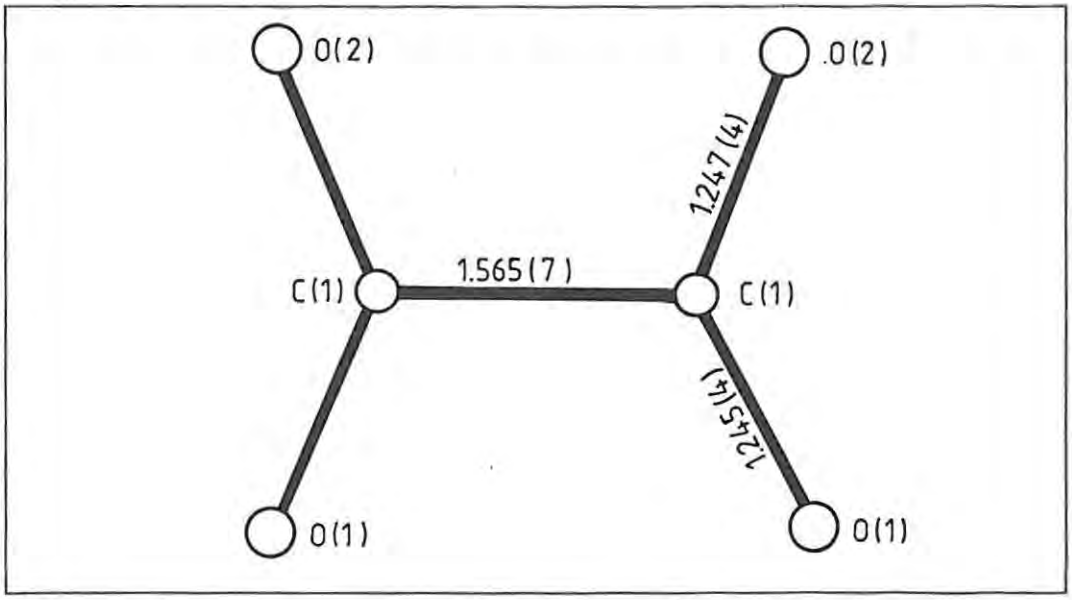

Figure 1.6 The bond lengths (Å) of the oxalate anion of zinc oxalate dihydrate

Again, the oxalate ion is completely planar, which suggests that π-delocalisation is occurring. The C-C bond length in zinc oxalate dihydrate (1.565(7) Å) is even longer than the C-C bond length in oxalic acid (1.544(4) Å). The longer C-C bond in the $C_2O_4^{2-}$ anion can be attributed to the electronegative oxygen atoms and electronic repulsion between the negative charges of the carboxylate groups. It can also be caused by delocalisation of the oxygen 2p electrons into the antibonding σ-orbital between the carbon-carbon bond. The two C-O bonds are almost identical. The similarity of the C-O bonds implies that there is complete resonance between the following two structures:

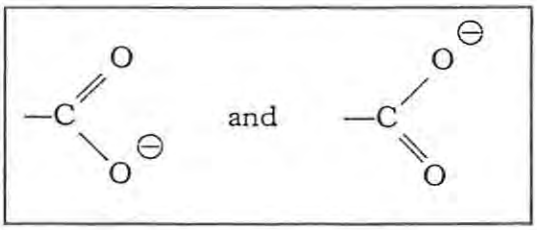

The strong reducing properties of the oxalate ion and the low onset temperatures of decomposition of the metal oxalates can be attributed to the weakness of the C-C bond and the ease with which the fragments are oxidised to CO_2 [18].

1.5.4 The thermal decomposition of barium oxalate

The thermal decomposition of $BaC_2O_4.0.5H_2O$ in N_2 is reported to take place in three major stages:

1) $BaC_2O_4.0.5H_2O(s) \rightarrow BaC_2O_4(s) + 0.5H_2O(g)$ (50-110°C)
2) $BaC_2O_4(s) \rightarrow BaCO_3(s) + CO(g)$ (330-550°C)
3) $BaCO_3(s) \rightarrow BaO(s) + CO_2(g)$

The temperature range for the dehydration (50-110°C) is significantly lower than those found for the other monooxalates. This might be due to the weaker electrostatic field generated by the barium ion.

Stage (2) is accompanied by the formation of carbon, via the Boudouard reaction:

$2CO(g) = CO_2(g) + C(s)$

Between 670 and 725°C the residual carbon reacts with the $BaCO_3$ to form BaO and 2CO. The onset temperature for the carbonate decomposition was found to increase with the CO_2 partial pressure. In N_2, the carbonate decomposition started at 703°C, whereas in pure CO_2 it started at 1348°C.

Two phase transitions of $BaCO_3$ were detected in the temperature range used (812°C and 976°C).

The authors [19] did not estimate the enthalpies for each stage from their DSC results. The oxalate decomposition was initially exothermic but then became strongly endothermic. Tanaka and Koga [20] have given a value of 41.8 kJ mol^{-1} for the enthalpy change for the oxalate decomposition.

The kinetics of the thermal decomposition of BaC_2O_4 to $BaCO_3$

have been investigated by Tanaka and Koga [20] using both isothermal and non-isothermal methods. An onset temperature of 400°C for the decomposition was reported by these authors. The zero-order rate equation gave the best fit for the isothermal decomposition of BaC_2O_4 in the temperature range, 393-421°C. The activation energy, E_a, derived from the isothermal analysis was 181.0 kJ mol^{-1}. The authors also studied the decomposition of CaC_2O_4 and SrC_2O_4 and reported that the Avrami-Erofeev (n = 1.5) equation, $[-\ln(1 - \alpha)]^{1/n} = kt$, gave the best fit for the decomposition of CaC_2O_4 and the contracting-geometry (n = 1.54) equation, $[1 - (1 - \alpha)^{1/n}] = kt$, gave the best fit for the decomposition of SrC_2O_4.

1.5.5 The thermal decomposition of copper oxalate

The thermal decomposition of copper oxalate has been studied recently by Coetzee *et al.* [11]. The decomposition, in N_2, started at about 260°C and took place in one stage. The mass of the solid product from the decomposition corresponded to the formation of Cu_2O. Evolved gas analysis showed that both CO_2 and CO are evolved during the decomposition. The proportion of CO in the evolved gas was greatest during the initial period of the decomposition and declined steadily as the reaction proceeded. The DSC results showed that (unlike the oxalates $[M(C_2O_4)(H_2O)_2]_n$) the decomposition of copper oxalate in N_2 is exothermic with an enthalpy change of -33 kJ mol^{-1}.

The kinetics of the thermal decomposition of copper oxalate have been studied by Galwey and Mohamed [21]. The α-time curves for the decomposition were found to be sigmoidal. The acceleratory stage ($0 < \alpha < 0.3$) could be described by the exponential rate law, $\ln(\alpha) = kt$. A wide range of the reaction ($0.24 < \alpha < 0.91$) could be described by the first-order rate equation (F1). The final stages, however, were considerably more deceleratory than expected for first-order behaviour. The proportion of Cu(II) and Cu(I) in the solid, at various stages of the reaction, showed that the decomposition proceeded with stepwise reduction of the copper(II) ions.

1.5.6 The thermal decompositions of the mixed metal copper oxalates, $MCu(C_2O_4)_2.3H_2O$, M = Fe, Co, and Ni

The thermal behaviour of these compounds differed from that of the individual metal oxalates and copper(II) oxalate. The dehydrations of the three mixed oxalates have been described above. They were deceleratory processes (R2) which take place in one stage. The onset temperatures for the dehydration, from DSC experiments, increased in the following order:
$FeCu(C_2O_4)_2.3H_2O$ (~139°C), $CoCu(C_2O_4)_2.3H_2O$ (~141°C),
$NiCu(C_2O_4)_2.3.5H_2O$ (202 ±10°C)

The mass losses for the dehydrations of $CoCu(C_2O_4)_2$ and $FeCu(C_2O_4)_2$ suggested that there were three moles of water per mole of mixed metal oxalate. The mass loss for the dehydration of $NiCu(ox)_2$, in N_2, suggested that there were 3.5 moles of water per mole of $NiCu(ox)_2$. However, since the samples were dried at room temperature, the sample may not have been completely dry, and the extra water (0.5 mole) may not be part of the crystal lattice.

The decompositions were endothermic processes and took place in two overlapping stages. The mixed oxalates, $MCu(ox)_2.3H_2O$, do not show the exothermic behaviour characteristic of copper(II) oxalate. The percentage mass of the residue from the decomposition of $FeCu(C_2O_4)_2.3H_2O$, in N_2, corresponded to that calculated for the formation of FeO and Cu_2O by loss of CO and CO_2. The percentage mass of the decomposition products of $CoCu(C_2O_4)_2.3H_2O$ and $NiCu(C_2O_4)_2.3H_2O$, in N_2, was closest to formation of Co and Cu, and Ni and Cu with the evolution of four moles of CO_2 per mole of reactant.

The onset temperatures for the decomposition, in N_2, from DSC experiments, increased in the order:
$CoCu(C_2O_4)_2.3H_2O$ (~345°C), $FeCu(C_2O_4)_2.3H_2O$ (~351°C),
$NiCu(C_2O_4)_2.3.5H_2O$ (~362°C)

The authors [11] studied the kinetics of the thermal dehydrations and decompositions using isothermal experiments. The dehydrations, like the oxalates $[M(C_2O_4)(H_2O)_2]_n$, could be described by the contracting-area equation (R2). The isothermal rate vs. time curves showed that the decompositions were complex,

there were at least two overlapping processes taking place. The shapes of the peaks indicated that both processes were initially acceleratory, and then deceleratory. The isothermal rate was assumed to be made up of weighted contributions from individual processes which could be described by the Avrami-Erofeev equation. Calculated rate vs time curves were then compared with the experimental curves and the differences between these curves were minimised by adjustment of n_j (the Avrami-Erofeev exponents), k_j (the rate constants), w_j (the weighting factors) and, if necessary, t_o. Values of k were then used in Arrhenius plots to calculate E_a and A.

1.5.7 Thermal decomposition of nickel(II)-cobalt(II) oxalate coprecipitate

The thermal decomposition of this solid solution system was studied using TG and TM [22]. A series of the mixed binary Ni(II)-Co(II) oxalate samples were prepared at 25% (atom) intervals across the system. Physical mixtures were also prepared by mixing the pure end members. The DTG and DTM curves showed that the decomposition occurs in two overlapping stages. Since the two stages of the decomposition overlapped with each other, the kinetics of the two step decomposition was not studied. From the DTG curves, the authors stated that the physical mixtures behaved as individual oxalates while the coprecipitate decomposed as a single entity. The TM curves showed that the products formed from the physical mixture and the coprecipitate were distinctly different. The magnetic behaviour of the product from the coprecipitate was consistent with the behaviour predicted for a Ni-Co alloy, but the products from the physically mixed oxalate do not show the transition temperature predicted for an alloy.

1.6 Preliminary experiments

The similarity of the powder diffraction patterns of $MCu(C_2O_4)_2.3H_2O$ to those of the complexes $[M(C_2O_4)(H_2O)_2]_n$ suggests that doping the structure of copper oxalate with other metal ions induces a change in the crystal structure and a structure

isomorphous with $[M(C_2O_4)(H_2O)_2]_n$ is obtained. In continuation of the study of mixed metal copper oxalates, $MCu(C_2O_4)_2$, further complexes were prepared with metal ions which were chosen with large or small ionic sizes relative to the copper(II) ion (ionic radius Cu^{2+} = 0.70 Å) in the hope that a change in the crystal structure would occur. An unsuccessful attempt was made to prepare the complex, $MgCu(C_2O_4)_2$ (ionic radius Mg^{2+} = 0.65 Å) although the syntheses of $MgCo(C_2O_4)_2$ (ionic radius Co^{2+} = 0.74 Å) and $MgNi(C_2O_4)_2$ (ionic radius Ni^{2+} = 0.72 Å) were successful. An attempt to prepare $BaCu(C_2O_4)_2$ (ionic radius Ba^{2+} = 1.35 Å) also proved to be unsuccessful. However, during preparative experiments (described in Chapter 2) blue crystals of the compound $Ba[Cu(C_2O_4)_2(H_2O)].5H_2O$ were obtained.

All previous attempts to prepare crystals of copper oxalate suitable for single crystal analysis have failed. Recently, naturally occurring copper oxalate was discovered in Australia [23], but not even this mineral was sufficiently crystalline for structure determination by X-ray crystallography. In an abortive attempt to make mixed copper(II) acetate-oxalate, microcrystalline copper oxalate was obtained with single crystals being visible under a light microscope. The crystals were like flattened discs or rounded plates; one crystallographic axis is considerably shorter than the other two and the edges are circular. The diameters of these discs are typically 10 μm. This is consistent with a model structure which consists of infinite chains following a particular direction. The appearance of this sample and the size of the crystallites are almost identical to those of the naturally occuring copper oxalate.

Another attempt to make single crystals of copper oxalate was made using a supercritical water as a solvent for recrystallisation. The critical constants of water are 218 bar and 374°C. A preliminary experiment was done in a brass reaction vessel with a pressure of about 500 bar but at a temperature below 100°C.
Fortuitously, the copper(II) ions present in the copper oxalate slowly oxidised the zinc present in the brass reaction vessel. The rate of this reaction was slow enough for crystals of

extremely insoluble zinc oxalate dihydrate to form, perhaps mimicking a natural geochemical reaction. These crystals were used to determine the structure of zinc oxalate dihydrate. The only other oxalate of this group, of which suitable crystals for single crystal structure determination are reported to exist, is the mineral humboldtine ($[Fe(C_2O_4)(H_2O)_2]_n$). Presumably crystals of this compound form over geological time scales.

This thesis deals with the crystal structures of $[Zn(C_2O_4)(H_2O)_2]_n$ and $Ba[Cu(C_2O_4)_2(H_2O)].5H_2O$. The thermal behaviour of $Ba[Cu(C_2O_4)_2(H_2O)].5H_2O$ was then studied in detail for correlation with the crystal structure. This class of compound is of interest as possible precursors for mixed metal oxides with interesting properties such as superconductivity.

CHAPTER 2

EXPERIMENTAL

2.1 Preparation of $Ba[Cu(C_2O_4)_2(H_2O)].5H_2O$ and $[Zn(C_2O_4)(H_2O)_2]_n$

$Ba[Cu(C_2O_4)_2(H_2O)].5H_2O$ was synthesised as follows: 100 mL of 0.10 M aqueous solution of $K_2C_2O_4.H_2O$ was heated to 35°C and maintained at that temperature and stirred while 50 mL of 9.2×10^{-2} M $CuCl_2.2H_2O$ solution was added dropwise from a burette. The resulting solution of $[Cu(C_2O_4)_2]^{2-}$ ions was made slightly acidic by adding 0.25 mL of glacial acetic acid. 20 mL of a 1.7×10^{-1} M $BaCl_2.2H_2O$ was then slowly added from a burette to the stirred solution. A pale blue, crystalline precipitate rapidly formed. The precipitate was separated by filtration. The filtrate was left to stand, and dark blue crystals of the product appeared overnight (yield = 0.51 g).

$[Zn(C_2O_4)(H_2O)_2]_n$ was formed unexpectedly while subjecting a mixture of distilled water (20 mL) and copper oxalate (0.2 g) in a brass cylinder to high pressure (200 bar) at 70°C for 24 hours. The copper(II) ions present in copper oxalate slowly oxidised the zinc present in the brass and small, colourless crystals of zinc oxalate dihydrate were produced.

2.2 Apparatus

Infrared spectroscopy

Infrared spectra were recorded using Beckman IR 4260 and Perkin-Elmer IR 180 spectrophotometers in the λ range 4 000 -300 cm^{-1} using the KBr disc method.

Ultraviolet-visible spectroscopy

Diffuse reflectance spectra were recorded using a Beckman 5240 spectrophotometer, in the range 5 000 - 17 000 cm^{-1}.

Magnetic susceptibility

The magnetic susceptibility of $Ba[Cu(C_2O_4)_2(H_2O)].5H_2O$ was measured using a Faraday balance with $Hg[Co(CNS)_4]$ as calibrant.

Thermal analysis

Thermogravimetry (TG) and differential scanning calorimetry (DSC) were peformed using Perkin-Elmer Delta Series 7 instruments. An atmosphere of N_2, at a flow rate of 15 - 20 mL min^{-1}, and sample masses of between 3 and 5 mg were used.

instruments. An atmosphere of N_2, at a flow rate of 15 - 20 mL min^{-1}, and sample masses of between 3 and 5 mg were used. Aluminium sample pans, covered but not crimped, were used for the DSC experiments, and open platinum sample pans were used for the TG experiments.

X-ray powder diffractometry

X-ray powder patterns were obtained using a Philips powder diffractometer. Co Kα radiation (λ = 1.791 Å) was used. A powder diffraction photograph was also taken using a Stoe Reciprocal Lattice Explorer with Cu Kα radiation (λ = 1.5418 Å).

Single crystal X-ray diffractometry

The space group and the approximate unit cell dimensions were determined using precession methods. Precession photographs were taken with a Stoe Reciprocal Lattice Explorer using Ni filtered Cu Kα radiation (λ = 1.5418 Å).

A full set of intensities was collected at the University of Cape Town using a four-circle Enraf-Nonius CAD4 diffractometer with graphite monochromated Mo Kα radiation (λ = 0.7107 Å). Semi-empirical absorption corrections were carried out for Lorentz and backround effects. Accurate cell parameters were determined during the collection.

The structure solutions and data refinement were carried out on a MICROVAX 3100 computer at Rhodes University using the program SHELX-76 [24]. The program PLUTO was used to obtain molecular plots [25]. Several other computations were done using the NRC VAX crystal structure system [26].

CHAPTER 3

SPECTROSCOPIC CHARACTERISATION OF $Ba[Cu(C_2O_4)_2(H_2O)].5H_2O$ AND $Na_2[Cu(C_2O_4)_2].2H_2O$

3.1 Infrared spectroscopy

Nakamoto [27] has indexed the infrared absorption spectra of several metal dioxalato complexes using normal coordinate analysis. The infrared spectra of these oxalates were very similar to the ones measured here, and his results were used to index the different absorption bands of the infrared spectra of $Ba[Cu(C_2O_4)_2(H_2O)].5H_2O$ and $Na_2[Cu(C_2O_4)_2].2H_2O$ (Table 3.1)

Table 3.1 The indexed infrared absorptions of $Ba[Cu(C_2O_4)_2(H_2O)].5H_2O$ (A) and $Na_2[Cu(C_2O_4)_2].2H_2O$ (B)

ν/cm^{-1}(A)	ν/cm^{-1}(B)	Assignment
3550	3540	ν(O-H)
3400	3448	ν(O-H)
1676	1720	ν_{as}(C=O)
1636	1674	ν_{as}(C=O)
1425	1420	ν_s(C-O) + ν(C-C)
1300	1280	ν_s(C-O) + δ(O-C-O)
905,880	903	ν_s(C-O) + δ(O-C=O)
812	814	δ(O-C-O) + ν(Cu-O)
540	560	ν(Cu-O) + ν(C-C)
500	500	ring deformation
342	342	out of plane bend

3.2 Electronic spectroscopy

In this section an attempt was made to use a method developed by Krisnamurthy and Schaap [28] to estimate the energies of the 3d-orbitals of $Ba[Cu(C_2O_4)_2(H_2O)].5H_2O$ and $Na_2[Cu(C_2O_4)_2].2H_2O$. The results of these calculations are speculative since several assumptions were made and because there is a lack of reliable

quantitative spectroscopic data for copper(II) complexes.

Krisnamurthy and Schaap have calculated, using crystal field theory, the d-orbital energies of three primary groups of ligands from which nearly all the geometric structures of different complexes can be derived. The three primary groups are M-L (1 ligand on the z-axis), ML_2 (2 ligands 90° to each other in the xy-plane), and ML_4 (4 ligands situated at the corners of a regular tetrahedron). The energies of the d-orbitals of these three ligand groups are shown in Table 3.2.

Table 3.2 The d-orbital energies (in Dq) for the three primary ligand groups

Group	z^2	$x^2 - y^2$	xy	xz	yz
ML	5.14	-3.14	-3.14	0.57	0.57
ML_2	-2.14	6.14	1.14	-2.57	-2.57
ML_4	-2.67	-2.67	1.78	1.78	1.78

a) $Na_2[Cu(C_2O_4)_2].2H_2O$

The copper(II) ion in this complex is in an irregular octahedral environment. The two independent equatorial bonds are 1.929 and 1.930 Å long, and the independent axial bond (which is tilted by 8°) is 2.803 Å long. The sp^2 hybridised lone pair of the axial oxygen is not directed towards the copper(II) ion, but lies in the plane defined by the oxalate group. The axial bond is substantially longer than the equatorial bond. The strength of a coordinate bond has been said to be roughly inversely proportional to the fifth power of the separation [29]. The ligand field generated by the axial ligands was thus ignored, and the copper(II) ion was treated as a square-planar complex. The d-orbital energies of a square-planar complex is twice that of the ML_2 ligand group and are shown in Table 3.3.

Table 3.3 The estimated d-orbital energies (in Dq) for a square-planar ion

Orbital	z^2	$x^2 - y^2$	xy	xz	yz
Energy	-4.28	12.28	2.20	-5.14	-5.14

There are three possible d-d transitions for the above d-orbital energy system:

1) xz, yz → $x^2 - y^2$ ΔE = 17.42 Dq
2) z^2 → $x^2 - y^2$ = 16.56 Dq
3) xy → $x^2 - y^2$ = 10.00 Dq

Transitions (1) and (2) occur close together and are unlikely to be resolved in the experimental spectrum.

The experimental UV-visible spectrum for $Na_2[Cu(C_2O_4)_2].2H_2O$ contained, instead of three bands, one broad unsymmetrical band with an absorption maximum at 15500 cm^{-1}. Therefore the absolute values for the above transitions cannot be measured directly from the absorption spectrum. Assuming that 10 Dq for $Na_2[Cu(C_2O_4)_2].2H_2O$ is 9400 cm^{-1}, the three d-d spectral transitions for $Na_2[Cu(C_2O_4)_2].2H_2O$ might occur at the following wavelengths:

Table 3.4 Calculated d-d transitions for $Na_2[Cu(C_2O_4)_2].2H_2O$

Transition			E/Dq	ν/cm^{-1}	λ/nm
xz, yz	→	$x^2 - y^2$	17.42	16400	609
z^2	→	$x^2 - y^2$	16.56	15600	640
xy	→	$x^2 - y^2$	10.00	9400	1060

b) $Ba[Cu(C_2O_4)_2(H_2O)].5H_2O$

The coordination geometry of the copper(II) ion of $Ba[Cu(C_2O_4)_2(H_2O)].5H_2O$ is a square-pyramidal with a small amount of trigonal distortion. The trigonal distortion was not taken into account. The energies of the 3d-orbitals were estimated by

adding a contribution by the axial ligand to the square-planar ligand field. The ligand field was assumed to decrease with the fifth power of separation. Then Dq(axial) = (1.955 Å/2.467 Å)^5 x Dq(ML).

Table 3.5 Estimated 3d-orbital energies (in Dq) for the copper(II) ion of $Ba[Cu(C_2O_4)_2(H_2O)].5H_2O$

Orbital	z^2	$x^2 - y^2$	xy	xz	yz
Energy	-2.22	11.02	1.02	-4.91	-4.91

By comparing the above table to Table 3.3 it is clear that, from these calculations, the splitting of the 3d-orbitals of $Ba[Cu(C_2O_4)_2(H_2O)].5H_2O$ is somewhat smaller than the splitting of the 3d-orbitals of $Na_2[Cu(C_2O_4)_2].2H_2O$. Again, there are three possible d-d transitions:

1) xz, yz → $x^2 - y^2$ ΔE = 15.93 Dq
2) z^2 → $x^2 - y^2$ = 13.24 Dq
3) xy → $x^2 - y^2$ = 10.00 Dq

Assuming that 10 Dq for $Ba[Cu(C_2O_4)_2(H_2O)].5H_2O$ is 9400 cm^{-1} the three d-d spectral transitions for $Na_2[Cu(C_2O_4)_2].2H_2O$ might occur at the following wavelengths:

Table 3.6 Calculated d-d transitions for $Ba[Cu(C_2O_4)_2(H_2O)].5H_2O$

Transition			E/Dq	ν/cm^{-1}	λ/nm
xz, yz	→	$x^2 - y^2$	15.93	15000	670
z^2	→	$x^2 - y^2$	13.24	12400	810
xy	→	$x^2 - y^2$	10.00	9400	1060

The actual absorption spectrum contained one unresolved band with an absorption maximum at 14500 cm^{-1}.

3.3 Discussion

Since the spectra consisted of a single unresolved band with broad maxima, the calculations above cannot be readily tested. However, the calculations predict that the overall energy separation of the d-orbitals in $Na_2[Cu(C_2O_4)_2].2H_2O$ is greater than in $Ba[Cu(C_2O_4)_2(H_2O)].5H_2O$ which was observed in the spectra. The shift in the absorption maximum can also be understood by considering the relative effects of the equatorial and axial ligand fields. The equatorial ligand field tends to increase the overall splitting whereas the axial ligands (i.e. the ligands which belong to the ligand group (ML)) oppose the splitting by the equatorial ligands (ML_2) (Table 3.2). Therefore introducing axial ligands to the copper(II) sphere will tend to reduce the overall splitting. The equatorial copper-oxygen bonds are shorter (1.929 compared to 1.953 Å) and hence the equatorial ligand field is greater in $Na_2[Cu(C_2O_4)_2].2H_2O$. The axial ligand field in $Ba[Cu(C_2O_4)_2(H_2O)].5H_2O$ is stronger than the axial ligand field in $Na_2[Cu(C_2O_4)_2].2H_2O$.

The overall splitting of the d-orbitals of octahedral copper(II) complexes increases with the amount of Jahn-Teller distortion, but the separation between the xy and the $x^2 - y^2$ orbitals is unaffected by the distortion. Therefore, for a given ligand, the separation of the d-orbitals is greatest in a square-planar complex and smallest in an undistorted octahedral complex. One can conclude, therefore, the coordination geometry of the copper(II) ion in $Na_2[Cu(C_2O_4)_2].2H_2O$ is closer to the ideal square-planar geometry whereas the copper(II) ion of $Ba[Cu(C_2O_4)_2(H_2O)].5H_2O$ is closer to the regular octahedral geometry.

CHAPTER 4

DETERMINATION OF THE CRYSTAL STRUCTURE OF $Ba[Cu(C_2O_4)_2(H_2O)].5H_2O$

4.1 Density determination

The density of the crystals was determined using the flotation method. Mixtures of CCl_4 and $HCBr_3$ were used. The density measured was 2.59 g cm^{-3}.

4.2 Preliminary X-ray analysis

The space group and approximate cell dimensions were determined using the De Jong-Bouman method [31]. The crystals were needle-shaped and a suitable crystal with well-formed faces was chosen for the photographs. The needle axis was chosen as the rotation axis corresponding to the smallest lattice constant. The crystal was centred using optical methods. From the resulting photographs, the lattice parameters a^*, b^* and γ^* were obtained. A cone-axis photograph was also taken, from which the value of the lattice constant, c was derived. This information was used to reorientate the crystal so that higher layer de Jong-Bouman photographs could be taken. No systematic absences were present and no symmetry elements could be recognized from the photographs which indicated that the crystals belong to the centrosymmetric space group $P\bar{1}$ or the non-centrosymmetric space group $P1$, with two formula units in the unit cell. The structure was successfully refined in the former space group. The crystal data determined from the rotation photographs are listed in Table 4.1.

Table 4.1 Crystal data for $Ba[Cu(C_2O_4)_2(H_2O)].5H_2O$ determined from the rotation photographs

Crystal System	Triclinic
Space group	$P\bar{1}$
Laue symmetry	$\bar{1}$
Multiplicity of each site	2
a/Å	6.52
b/Å	9.20
c/Å	10.94
α/°	85.6
β/°	79.5
γ/°	80.3

4.3 Data Collection

A full three-dimensional data set was collected in the ω - 2θ scan mode with a variable scan speed. Accurate cell dimensions were determined during the data collection by a least squares analysis of the χ, φ, and 2θ angles of 25 reflections accurately centred on the diffractometer. The intensities of three reference collections were checked to see if any crystal decay occurred during the data collection. There was no significant increase in the absorption by the crystal. Absorption corrections were applied for polarisation and Lorenz effects. A reflection was said to be observed if $I_{rel} > 2\sigma(I_{rel})$, where $\sigma(I_{rel})$ is the standard error in the relative integrated intensity (I_{rel}). Of the 2505 reflections that were read, 284 were rejected, leaving 2221 unique reflections. The crystal data are shown in Table 4.2.

4.4 Solution and refinement of the structure

From the intensity data, the structure factor amplitudes, $|F|$, and hence the Patterson map were computed. The structure was solved using the heavy atom method. The scattering factors used in the refinement were from the International Tables of Crystallography [32].

Table 4.2 Experimental details of crystal, data collection, structure solution and refinement of $Ba[Cu(C_2O_4)_2(H_2O)].5H_2O$

Molecular Formula	$C_4H_{12}O_{14}BaCu$
M_r/g mol^{-1}	485.02
Space group	$P\bar{1}$
a/Å	6.539(2)
b/Å	9.211(3)
c/Å	10.928(3)
a/°	85.42(3)
$ß$/°	79.22(3)
γ/°	80.30(3)
V/Å^3	636.08(8)
Z	2
$F(000)$/e	467
μ(Mo Kα)	8.4
Absorption corrections	Semi-empirical
Size of the crystal/mm	2.0 × 0.5 × 0.1
ρ_c/g cm^{-3}	2.59
Scan mode	ω-2θ
Scan width in ω/deg	(0.85+0.35 tan θ)
Aperture width/mm	(1.12+1.05 tan θ)
Scan speed	variable, 40 s max.time
Crystal decay	none
No. reflections collected	2474
No. reflections with $I_{rel}>2\sigma I_{rel}$, N	2221
No. parameters, NP	182
$R = \Sigma(\|F_o\| - \|F_c\|)/\Sigma\|F_o\|$	0.0522
$R_w = \Sigma w^{1/2}(\|F_o\| - \|F_c\|)/\Sigma w^{1/2}\|F_o\|$	0.0573
Weighting factor, w	$1.000/(\sigma^2F+0.008805F^2)$

Solving the Patterson function

The Patterson map represents the superposition of all the interatomic vectors in the structure. The peak at the origin contains the vectors of each atom to itself (e.g. the vector Cu-Cu, the vector Ba-Ba). The relative height of the origin peak is thus equal to $2 \times 29^2 + 2 \times 56^2 + 28 \times 8^2 + 8 \times 6^2 = 10358$ units. The expected heights of the other large peaks on the map are:

Ba - Ba peak $\quad 56 \times 56 \times \frac{1000}{10358} \approx 300$ units

Ba - Cu peak $\quad 56 \times 29 \times \frac{1000}{10358} \approx 160$ units

Cu - Cu peak $\quad 29 \times 29 \times \frac{1000}{10358} \approx 80$ units

The most dominant scattering centre in the crystal is the barium ion. Since the space group is $P\bar{1}$, the two barium ions have the following atomic positions: $(x\ y\ z)$ and $(-x\ -y\ -z)$. Interatomic vectors corresponding to the differences in the coordinates of the various atomic positions expected are given in Table 4.3 :

Table 4.3 The expected positions of the interatomic vectors in $Ba[Cu(C_2O_4)_2(H_2O)].5H_2O$

	x	y	z	$-x$	$-y$	$-z$
$x\ \ y\ \ z$	$2x$	$2y$	$2z$	0	0	0
$-x\ -y\ -z$	0	0	0	$-2x$	$-2y$	$-2z$

The positions of the barium and the copper ions were located from the Patterson map. From these coordinates, the phases and the amplitudes of the diffracted beams were calculated. The coordinates of the copper and the barium ions were refined by reducing the difference between the observed structure factor amplitudes, $|F_o|$, and the calculated structure amplitudes, $|F_c|$. An approximate electron density map was determined by a Fourier summation of the observed structure factor amplitudes, $|F_o|$, with the calculated phases. The resulting difference electron density

map revealed the positions of all the remaining non-hydrogen atoms in the structure. The correctness of a structure is measured by the discrepancy indexes, R and R_w.

$R = \Sigma(|F_o| - |F_c|)/\Sigma|F_o| \quad R_w = \Sigma w^{1/2}(|F_o| - |F_c|)/\Sigma w^{1/2}|F_o|$

Full-matrix least-squares refinement was done, using the positions of the non-hydrogen atoms and the anisotropic temperature factors and the refinement converged to $R = 0.0522$ and $R_w = 0.0573$. The positions of the hydrogen atoms could not be determined from the final difference map. This was due to the large scattering factor of the barium ions. The maximum residual electron density in the final map was 3.0 e/Å and the shift/error ratio was less than 0.1.

The final atomic coordinates and equivalent isotropic temperature factors are presented in Table 4.4.

Table 4.4 Fractional atomic coordinates (x 10^5 for Ba and Cu, otherwise x10^4) and equivalent isotropic temperature factors (Å^2) for $Ba[Cu(C_2O_4)_2(H_2O)].5H_2O$ with their estimated standard deviations

	x/a	*y/b*	*z/c*	U_{eq}
Cu(1)	45697(14)	56148(9)	26672(7)	19(1)
Ba(1)	33685(5)	109328(3)	21548(3)	15(1)
O(1)	5056(7)	7631(6)	2163(5)	24(1)
O(2)	6384(8)	5109(5)	1062(4)	23(1)
O(3)	3240(7)	6066(5)	4367(4)	23(1)
O(4)	4042(7)	3615(4)	3163(4)	21(1)
O(5)	6498(7)	8898(4)	530(3)	23(1)
O(6)	7921(7)	6287(5)	-631(4)	27(1)
O(7)	1720(8)	4958(5)	6093(4)	28(1)
O(8)	2388(8)	2405(5)	4771(5)	33(1)
O(9)	1639(10)	9104(6)	4180(5)	44(1)
O(10)	6586(8)	9978(6)	3466(5)	41(1)
O(11)	6991(7)	12123(5)	864(4)	27(1)
O(12)	-752(8)	12221(6)	2899(5)	30(1)
O(13)	724(8)	9152(6)	1340(5)	33(1)
O(14)	1088(8)	6184(5)	2025(4)	25(1)
C(1)	6109(9)	7726(6)	1085(5)	15(1)
C(2)	6920(9)	6270(6)	412(5)	16(1)
C(3)	2602(8)	4915(6)	4995(5)	16(1)
C(4)	3024(10)	3516(6)	4295(6)	19(1)

$$U_{eq} = 1/3\Sigma_i\Sigma_j a_i^* a_j^* (\mathbf{a}_i . \mathbf{a}_j)$$

4.5 Additional calculations

Due to Jahn-Teller distortion, copper-oxygen bonds may be too long to be classified as bonds by SHELX. Close investigation of the atomic coordinates shows that an oxygen atom from the oxalate group of the adjacent assymetric unit (O(7)) lies beneath the vacant coordination site of the copper(II) ion. The distance between the copper(II) ion and this oxygen atom was calculated to determine whether this atom is part of the copper(II) coordination polyhedron. In addition, since copper(II) complexes frequently have antiferromagnetic properties associated with closely spaced copper(II) ions, the shortest copper-copper distance was also calculated.

In a triclinic system the orthogonal coordinates (X, Y, Z) are given by the following expressions:

$X = a \sin \beta \sin \gamma^* \times (x/a)$

$Y = -a \sin \beta \cos \gamma^* \times (x/a) + b \sin \alpha \times (y/b)$

$Z = -a \cos \beta \times (x/a) + b \cos \alpha \times (y/b) + c \times (z/c)$

where:

$\sin \gamma^* = (1- \cos^2 \gamma^*)^{1/2}$

$\cos \gamma^* = (\cos \alpha \cos \beta - \cos \gamma)/(\sin \alpha \sin \beta)$

The distance, r between the two orthogonalised coordinates can then be calculated.

The closest separation between two copper(II) ions:

Since the space group is centrosymmetric, there are two copper(II) ions in the unit cell. These two copper ions which have the following atomic positions:

Cu(A): (0.4570 0.5615 0.2667) = (x/a y/b z/c)

Cu(B): (0.5430 0.4385 0.7333) = ($-x/a$ $-y/b$ $-z/c$)

The lattice dimensions are:

a = 6.539Å b = 9.211Å c = 10.928Å

Therefore the orthogonal coordinates are:

Cu(A): (2.899 5.615 3.884) = ($X(A)$ $Y(A)$ $Z(A)$)

Cu(B): (3.445 4.573 8.994) = ($X(B)$ $Y(B)$ $Z(B)$)

The distance, r between Cu(A) and Cu(B) is

$= ((X(A) - X(B))^2 + (Y(A) - Y(B))^2 + (Z(A) - Z(B)))^{1/2}$

= 5.244 Å

Thus the two copper(II) ions are relatively widely spaced.

The separation between the oxygen atom, O(7) and the closest copper(II) ion

The symmetry equivalent copper(II) ion (Cu(b)) and the oxygen atom (O(7)) have the following atomic coordinates:

Cu(*B*): (0.5430 0.4385 0.7333) = (*-x/a -y/b -z/c*)

O(7): (0.1720 0.4958 0.6093) = (*x/a y/b z/c*)

The corresponding orthogonal coordinates of this copper(II) ion are:

$X(B) = 3.445$, $Y(B) = 4.573$, $Z(B) = 8.994$

And the orthogonal coordinates of the oxygen atom O(7) are:

$X(7) = 1.0912$, $Y(7) = 4.7255$, $Z(7) = 7.2286$

The distance, r between Cu(*B*) and O(7) is then

$$r = ((X(7) - X(B))^2 + (Y(7) - Y(B))^2 + (Z(7) - Z(B))^2)^{1/2}$$
$$= 2.947 \text{ Å}$$

This distance is significantly longer than the axial copper-oxygen bond, Cu-O(14) (2.467 Å) and is not at right angles to the plane defined by the two equatorial copper-oxygen bonds (Cu-O(1) and Cu-O(4)) but makes an angle of 7° to the orthogonal axis of the plane defined by these two bonds. The sp^2 hybridised lone pair of O(7), unlike the 2 sp^3 lone pairs of the axially bonded H_2O molecule, is not directed towards the copper ion, but lies in the plane defined by the oxalate group. This oxygen atom was thus not treated as part of the copper(II) coordination polyhedron. Interaction between this oxygen atom with the copper ion cannot, however, be completely ruled out.

4.6 Description of the structure of $Ba[Cu(C_2O_4)_2(H_2O)].5H_2O$

The interatomic lengths and angles are presented in Tables 4.5 and 4.6 respectively.

A packing diagram is shown in Figure 4.1. The structure contains chains of monomeric $[Cu(C_2O_4)_2(H_2O)]^{2-}$ units weakly linked by barium ions. The coordination polyhedron around the copper(II) ion has square-pyramidal geometry (*C4/v* symmetry). The two oxalate groups occupy the equatorial positions and the and the axial position is occupied by a water molecule. The axial copper-oxygen bond (2.467(4) Å) is much longer than the equatorial bonds (mean length = 1.953(4) Å). There is a small

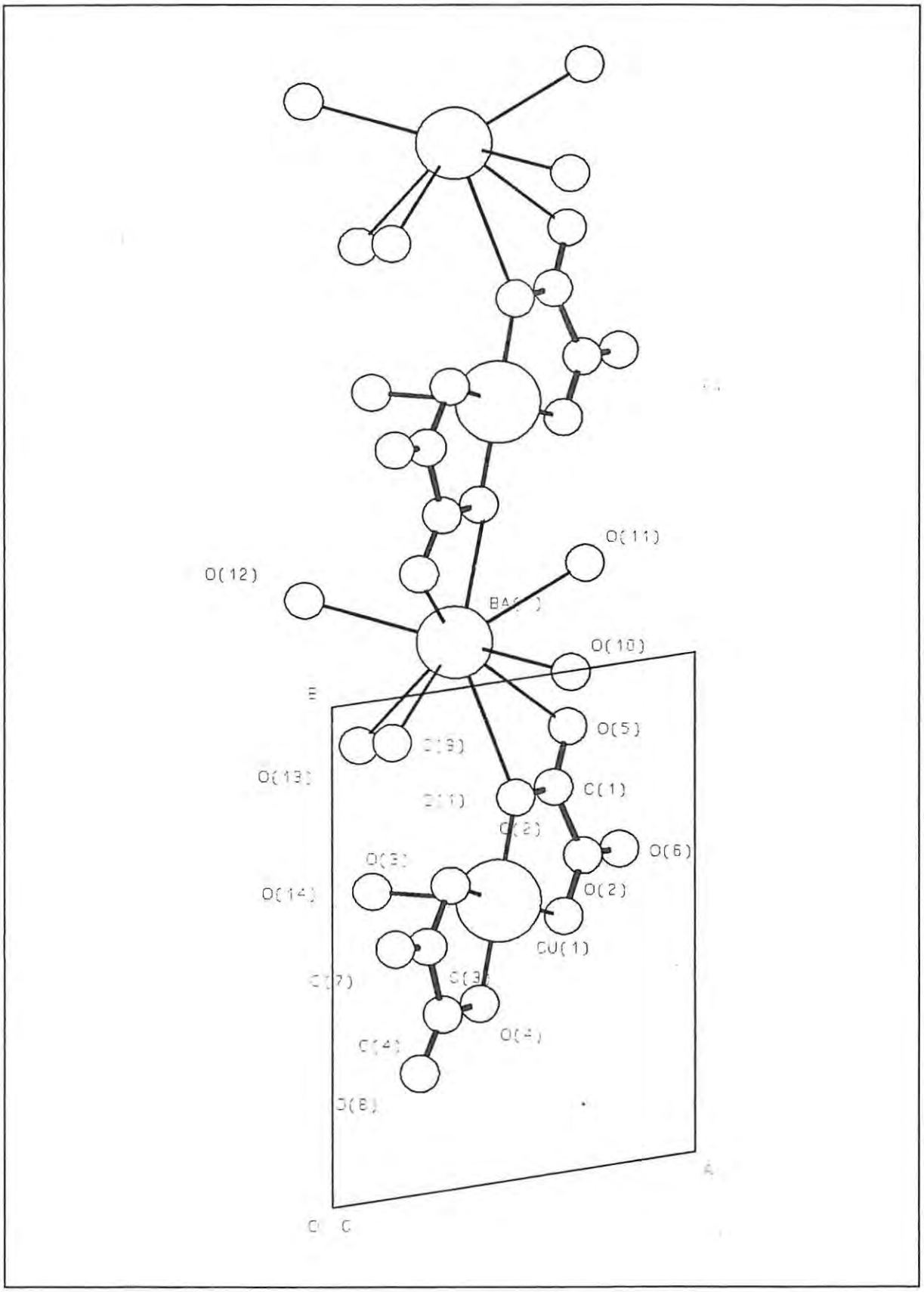

Figure 4.1 Packing diagram of $Ba[Cu(C_2O_4)_2(H_2O)].5H_2O$

amount of trigonal distortion, the O(1)-Cu-O(4) angle is 179° but the O(3)-Cu-O(2) angle is only 170°. The two oxalate groups are therefore twisted relative to each other. The axial copper-oxygen bond (Cu-O(14)) is approximately 90° to the plane defined by O(1)-Cu-O(4). All of the equatorial Cu-O bond lengths are different. The bonds, Cu-O(1) and Cu-O(2), are longer (1.955(4) and 1.966(4) Å) than the other two equatorial Cu-O bonds (1.942(4) and 1.947(4) Å). The mean equatorial copper-oxygen bond length (1.953(4) Å) of this complex is longer than the mean equatorial copper-oxygen bond length in $Na_2[Cu(C_2O_4)_2].2H_2O$ (1.929(1) Å). The oxalate ions are, therefore, more tightly held to the copper(II) ion in $Na_2[Cu(C_2O_4)_2].2H_2O$ than in $Ba[Cu(C_2O_4)_2(H_2O)].5H_2O$. A ball-and-spoke diagram of the $[Cu(C_2O_4)_2(H_2O)]^{2-}$ anion is shown in Figure 4.2. This anion is far less symmetrical than the $[Cu(C_2O_4)_2]^{2-}$ anion of $Na_2[Cu(C_2O_4)_2].2H_2O$. Unlike $Na_2[Cu(C_2O_4)_2].2H_2O$, which has many centrosymmetric related bonds, all the bond lengths of the dioxalato unit of $Ba[Cu(C_2O_4)_2(H_2O)].5H_2O$ vary.

The carbon-oxygen bonds which do not coordinate to the copper(II) ion in $Ba[Cu(C_2O_4)_2(H_2O)].5H_2O$ might be expected to be similar. However, these bonds range from 1.203(7) to 1.237(7) Å, the dimension, 1.203(7) Å, being shorter than the typical C=O bond. The carbon-oxygen bonds which do coordinate to the copper(II) ion in $Ba[Cu(C_2O_4)_2(H_2O)].5H_2O$ range from 1.252(7) to 1.302(7) Å. This is in contrast to $Na_2[Cu(C_2O_4)_2].2H_2O$ in which the carbon-oxygen bonds which coordinate to the copper(II) ion are similar (1.279(2) and 1.286(2) Å) and those which do not coordinate to copper(II) ion are also similar (1.220(2) and 1.225(2) Å).

The two carbon-carbon bonds of the $[Cu(C_2O_4)_2]^{2-}$ anion are significantly different. The carbon-carbon bond C(1)-C(2) (1.547(7) Å) is the usual length for carbon-carbon bonds for oxalate species but the carbon-carbon bond C(3)-C(4) (1.509(8) Å) is much shorter.

The coordination number of the barium ion is nine, with four oxygens from oxalate groups and five oxygens from water molecules. The barium-oxygen distances range from 2.748(5) to

3.171(4) Å. The oxygens of the water molecules are closer (2.748(5) to 2.869(6) Å) than the oxygens of the oxalate groups (2.914(4) to 3.171(4) Å). The oxygens are not symmetrically arranged around the barium ion. The barium-oxygen angles are apparently dictated by hydrogen bonding and ligand repulsions.

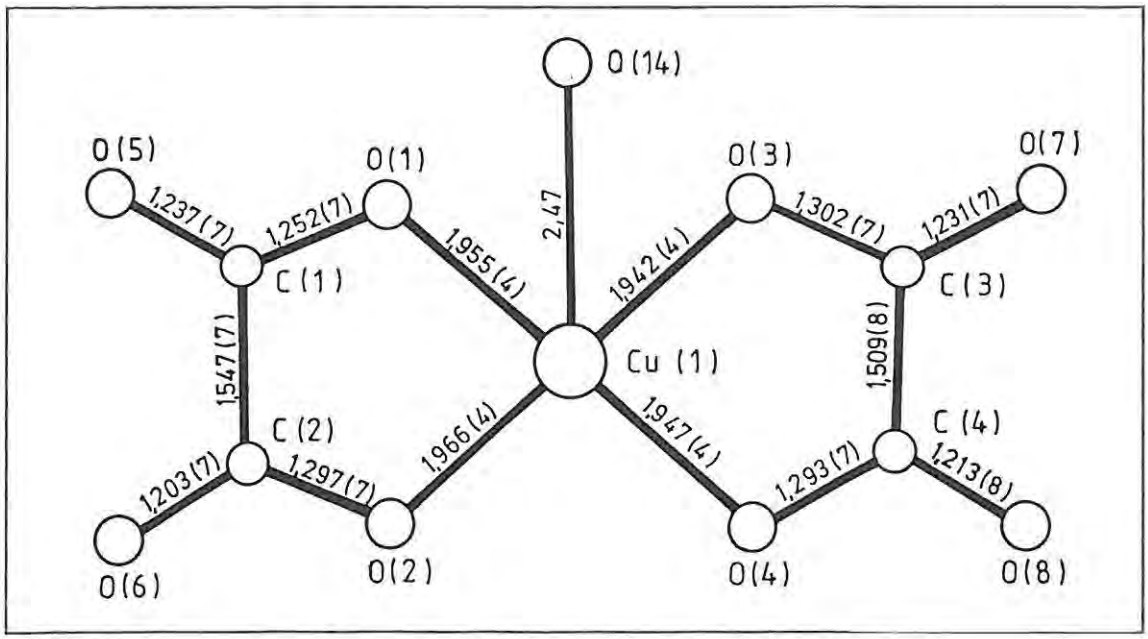

Figure 4.2 Ball-and-spoke diagram of the $[Cu(C_2O_4)_2(H_2O)]^{2-}$ anion of $Ba[Cu(C_2O_4)_2(H_2O)].5H_2O$

Table 4.5 Interatomic distances (Å) in $Ba[Cu(C_2O_4)_2(H_2O)].5H_2O$ with their estimated standard deviations ($x10^3$ Å)

a) Copper(II) coordination polyhedron	
Cu - O(1)	1.955(4)
Cu - O(2)	1.966(4)
Cu - O(3)	1.942(4)
Cu - O(4)	1.947(4)
Cu - O(14)	2.467(4)
b) Oxalate 1	
C(1) - O(1)	1.252(7)
C(1) - O(5)	1.237(7)
C(1) - C(2)	1.547(7)
C(2) - O(2)	1.297(7)
C(2) - O(6)	1.203(7)
c) Oxalate 2	
C(3) - O(3)	1.302(7)
C(3) - O(7)	1.231(7)
C(3) - C(4)	1.509(8)
C(4) - O(4)	1.293(7)
C(4) - O(8)	1.246(8)
c) Barium ion	
Ba - O(1) (oxalate 1)	3.056(4)
Ba - O(4) (oxalate 2)	2.914(4)
Ba - O(5) (oxalate 1)	2.955(4)
Ba - O(8) (oxalate 2)	3.171(4)
Ba - O(9) (H_2O)	2.849(6)
Ba - O(10) (H_2O)	2.748(5)
Ba - O(11) (H_2O)	2.853(5)
Ba - O(12) (H_2O)	2.754(5)
Ba - O(13) (H_2O)	2.869(6)

Table 4.6 Bond angles (°) in $Ba[Cu(C_2O_4)_2(H_2O)].5H_2O$ with their estimated standard deviations (x10°)

a) Copper(II) coordination polyhedron	
O(1) - Cu - O(2)	84.7(2)
O(1) - Cu - O(3)	94.8(2)
O(1) - Cu - O(4)	179.1(2)
O(1) - Cu - O(14)	89.8(2)
O(2) - Cu - O(3)	169.9(2)
O(2) - Cu - O(4)	95.6(2)
O(2) - Cu - O(14)	100.5(2)
O(3) - Cu - O(4)	85.1(2)
O(3) - Cu - O(14)	89.6(2)
O(4) - Cu - O(14)	89.3(2)
b) Oxalate 1	
O(1) - C(1) - O(5)	124.3(5)
O(2) - C(2) - O(6)	125.9(5)
C(1) - C(2) - O(2)	114.0(5)
C(1) - C(2) - O(6)	120.2(5)
C(2) - C(1) - O(1)	116.9(5)
C(2) - C(1) - O(5)	118.8(5)
c) Oxalate 2	
O(3) - C(3) - O(7)	122.2(5)
O(4) - C(4) - O(8)	123.6(6)
C(3) - C(4) - O(4)	115.3(5)
C(3) - C(4) - O(8)	121.1(6)
C(4) - C(3) - O(3)	115.9(5)
C(4) - C(3) - O(7)	121.9(5)
d) Barium Ion (Selected Angles)	
O(9) - Ba - O(12)	73.7(2)
O(10) - Ba - O(12)	131.9(2)

CHAPTER 5

THE DETERMINATION OF THE CRYSTAL STRUCTURE OF $[Zn(C_2O_4)(H_2O)_2]_n$

5.1 Determination of the space group and approximate cell dimensions

The space group and approximate cell dimensions were determined from rotation photographs using the De Jong-Bouman method [31]. A suitable crystal with well-formed faces was chosen for the photographs. The crystal was centred using optical methods. From the resulting photographs, the lattice parameters a^*, b^* and γ^* were obtained. A cone-axis photograph was also taken, from which the value of the lattice constant, c was derived. The following systematic absences were present: $h\ k\ l$: $h + k = 2n + 1$, and $h\ 0\ l$: $l = 2n + 1$ which indicated that the crystals belong to the centrosymmetric space group $C2/c$ or Cc. The structure was successfully refined in the former space group. For $Z = 4$, the assymetric unit must consist of half the monomeric unit $[Zn(C_2O_4)(H_2O)_2]$. The crystal data determined from the rotation photographs are given in Table 5.1.

Table 5.1 Crystal data for $[Zn(C_2O_4)(H_2O)_2]_n$ determined from rotation photographs

Crystal System	Monoclinic
Space group	$C2/c$
Laue Symmetry	$2/m$
Multiplicity of a general site	8
a/Å	12.1
b/Å	5.42
c/Å	9.82
β/°	127.8

5.2 Data Collection

A full three-dimensional data set was collected in the $\omega - 2\theta$ scan mode with a variable scan speed. Accurate cell

dimensions were determined during the data collection by a least squares analysis the intensities of 25 reflections accurately centred on the diffractometer. The intensities of three reference collections were checked to see if any crystal decay occured during the data collection. There was no significant increase in the absorption by the crystal. Semi-empirical absorption corrections were applied for polarisation and Lorenz-effects during the collection. 1040 reflections were read and of these relections, 577 were rejected as being space group group equivalent. A further 28 reflections were rejected leaving 435 unique reflections for the structure determination. The crystal data are shown in Table 5.2.

5.3 Solution and refinement of the structure

From the intensity data, the Patterson map was determined. The structure was solved using the heavy atom method. The scattering factors used in the refinement were from the International Tables of Crystallography [32].

The zinc ion, in the special position (1/2, *y*, 1/4), was located from the Patterson map. Subsequent difference electron density maps revealed all the remaining non-hydrogen atoms and ZnO_6 octahedra were noticeable. The electron density difference map based on the refinement using the positions of all the non-hydrogen and their anisotropic temperature factors showed the positions of the hydrogen atoms.

Least squares refinement was done using the positions of all the atoms, including the hydrogen atoms, and the anisotropic temperature factors and final values of 0.0368 for R and 0.0366 for R_w were obtained. The maximum residual electron density in the final map was less 1.0 e $Å^{-3}$ and the shift/error ratio was less than 0.03. These low values are a consequence of the very high crystal quality.

The final atomic coordinates, thermal parameters, and additional crystallographic information are presented in Tables 5.3, 5.4, 5.5, and 5.6. The interatomic distances and angles are presented in Tables 5.7 and 5.8.

Table 5.2 Experimental details of crystal, data collection, structure solution and refinement of $[Zn(C_2O_4)(H_2O)_2]_n$

Molecular Formula	$C_2H_4O_4Zn$
M_r/g mol^{-1}	173.44
Space group	*C*2/*c*
a/Å	11.786(2)
b/Å	5.397(1)
c/Å	9.712(1)
ß/°	126.19(5)
V/Å^3	498.58(8)
Z	4
F(000)/e	343.94
μ(Mo Kα)	8.4
Absorption corrections	Semi-empirical
Size of the crystal/mm	2.0 × 0.5 × 0.1
Scan mode	ω-2θ
Scan width in ω/deg	(0.85+0.35 tan θ)
Aperture width/mm	(1.12+1.05 tan θ)
Scan speed	variable, 40 s max.time
Crystal decay	none
No. of reflections collected	463
No. reflections with $I_{rel}>2\sigma I_{rel}$, *N*	435
No. parameters, *NP*	50
Max./min. residual e density	1.0
Max. shift error ratio	0.03
$R = \Sigma(\|F_o\| - \|F_c\|)/\Sigma\|F_o\|$	0.0368
$R_w = \Sigma w^{1/2}(\|F_o\| - \|F_c\|)/\Sigma w^{1/2}\|F_o\|$	0.0366
Weighting factor, *w*	$1.000/(\sigma^2F+0.008805F^2)$

Table 5.3 The equivalent positions in $[Zn(C_2O_4)(H_2O)_2]_n$

x	*y*	*z*	-*x*	*y*	1/2 - *z*

Table 5.4 Fractional atomic coordinates for $[Zn(C_2O_4)(H_2O)_2]_n$ with their estimated standard deviations ($x10^4$)

	x/a	*y/b*	*z/c*
Zn(1)	5000	5733(7)	2500
O(1)	4132(2)	2804(4)	788(3)
O(2)	5870(2)	8683(4)	4217(3)
O(3)	6754(3)	5634(3)	2425(4)
C(1)	4499(4)	745(4)	1502(5)
H(1)	7443(56)	6064(76)	3217(67)
H(2)	6724(43)	6195(73)	1712(63)

Table 5.5 The symmetry equivalent atoms in $[Zn(C_2O_4)(H_2O)_2]_n$

	x/a	*y/b*	*z/c*			
O(1)′	5868	2804	4212	1 - *x*	*y*	0.5 - *z*
O(2)′	4130	8683	783	1 - *x*	*y*	0.5 - *z*
O(3)′	3246	5634	2575	1 - *x*	*y*	0.5 - *z*
C(1)′	5501	10745	3498	1 - *x*	1 + *y*	0.5 - *z*
O(2)′	4130	-1317	783	1 - *x*	-1 + *y*	0.5 - *z*
C(1)′	5501	745	3498	1 - *x*	*y*	0.5 - *z*

Table 5.6 Anisotropic thermal parameters ($Å^2x10^4$) for $[Zn(C_2O_4)(H_2O)_2]_n$ with their estimated standard deviations ($Å^2x10^4$)

	U_{11}	U_{22}	U_{33}	U_{13}	U_{12}	U_{23}
Zn(1)	222(5)	71(5)	128(5)	71(4)		
O(1)	228(13)	71(11)	100(12)	44(10)	1(7)	-9(7)
O(2)	259(13)	79(11)	103(12)	46(11)	17(10)	-6(10)
O(3)	222(16)	204(17)	126(14)	71(13)	-20(7)	18(8)
C(1)	148(17)	104(19)	103(19)	50(16)	6(8)	7(9)
H(1)	212(108)					
H(2)	185(92)					

The anisotropic temperature factors are defined as:

$T_{iso} = \exp[-2\pi^2(\Sigma_{ij}U_{i,j}h_ih_ja_i^*a_j^*)]$, where $i,j = 1,2,3$.

Table 5.7 Bond distances (Å) in $[Zn(C_2O_4)(H_2O)_2]_n$ with their estimated standard deviations ($x10^3$ Å)

a) Zinc(II) ion		
Zn(1)-O(1)	(C_2O_4)	2.074(2)
Zn(1)-O(1)′	(C_2O_4)	2.074(2)
Zn(1)-O(2)	(C_2O_4)	2.085(2)
Zn(1)-O(2)′	(C_2O_4)	2.085(2)
Zn(1)-O(3)	(H_2O)	2.112(3)
Zn(1)-O(3)′	(H_2O)	2.112(3)
b) Oxalate ion		
C(1)-O(1)		1.245(4)
C(1)-O(1)′		1.245(4)
C(1)-O(2)		1.247(4)
C(1)-O(2)′		1.248(3)
C(1)-C(1)′		1.565(7)
c) Water molecule		
H(1)-O(3)		0.753(52)
H(2)-O(3)		0.737(49)
d) Hydrogen bonds*		
H(1)...O(3)"		2.840(8)
H(2)...O(3)"		2.808(9)

*The O-H lengths are too short. This is because the hydrogen atoms scatter the X-rays poorly. It may have been preferable to fix the O-H bond lengths to 1.0 Å during the refinement.

Table 5.8 Bond angles (°) in $[Zn(C_2O_4)(H_2O)_2]_n$ with their estimated standard deviations (°)

a) Zinc(II) ion	
O(1)-Zn-O(1)'	80.7(0.1)
O(2)-Zn-O(2)'	80.4(0.1)
O(1)-Zn-O(2)	179.9(0.0)
O(1)-Zn-O(3)	89.0(0.1)
O(2)-Zn-O(3)	91.0(0.1)
O(3)-Zn-O(3)'	177.1(0.1)
b) Oxalate group	
O(1)-C(1)-O(2)	126.4(0.3)
O(1)-C(1)-O(2)'	126.4(0.3)
O(1)-C(1)-C(1)'	116.8(0.2)
O(1)'-C(1)-C(1)'	116.8(0.2)
O(2)-C(1)-C(1)'	116.9(0.2)
O(2)c-C(1)-C(1)'	116.8(0.2)
c) Water molecule	
H(1)-O(3)-H(2)	104.9(4.8)
d) Selected remaining bond angles	
C(1)-O(1)-Zn	112.9(0.2)
H(1)-O(3)-Zn	116.4(3.6)
H(2)-O(3)-Zn	121.1(3.2)

5.4 Description of the structure of $[Zn(C_2O_4)(H_2O)_2]_n$

The structure consists of infinite chains of $[Zn(C_2O_4)(H_2O)_2]$ units which lie on a two-fold symmetry axis parallel to the *b*-axis (Figure 5.1). The oxalate ions bridge the zinc ions and water molecules are bonded to the zinc ions at the axial positions. The chains are linked by hydrogen bonds via the water molecules. A portion of one of the linear chains is shown in Figure 5.2. Since the structure is so symmetrical, there are only two crystallographically unique equatorial zinc-oxygen bonds, one unique axial zinc-oxygen bond, two unique carbon-oxygen bonds, and one unique carbon-carbon bond. The two independent carbon-oxygen bonds are essentially the same (1.245(4) and 1.247(4) Å) indicating complete delocalisation of the negative charge over both C-O bonds. This is in contrast with $Na_2[Cu(C_2O_4)_2)].2H_2O$ in which the oxalate groups do not bridge, and there are two types of C-O bonds.
The $[Zn(C_2O_4)(H_2O)_2]_n$ system is remarkably planar, the O(2)-Zn-O(1) angle is 179.9°.

The bond lengths and bond angles of the ZnO_6 coordination polyhedron are reported in Tables 5.8 and 5.9 respectively. The two pairs of Zn-O equatorial bonds, Zn-O(1) and Zn-O(2) have slightly different bond lengths (2.074(2) and 2.085(2) Å). The axial Zn-O(H_2O) bonds (2.112 Å) are slighty longer than the equatorial bonds. The bond angles of the coordination polyhedron surrounding the Zn^{2+} ion are almost the perfect octahedral values although the axial Zn-O(H_2O) bond is 1° out. The axial bond is bent slightly since the water molecules take part in hydrogen bonding with water molecules of adjacent chains. There are two unique hydrogen bonds in the structure: H(1)...O(3)" (2.840(8)) and H(2)...O(3)" (2.808(9) Å).

The tetragonality, *T* where *T* = (mean equatorial bond length)/(mean axial bond length) of this complex is equal to 0.99. The zinc-oxygen bonds are slightly shorter than the iron-oxygen bonds of $[Fe(C_2O_4)(H_2O)_2]_n$, but longer than the copper-oxygen bonds of $Na_2[Cu(C_2O_4)].2H_2O$.

The carbon-carbon bonds of $[Zn(C_2O_4)(H_2O)]_n$ (1.565(7) Å) are slightly longer than those found in $[Fe(C_2O_4)(H_2O)]_n$ (1.546 Å) [2]

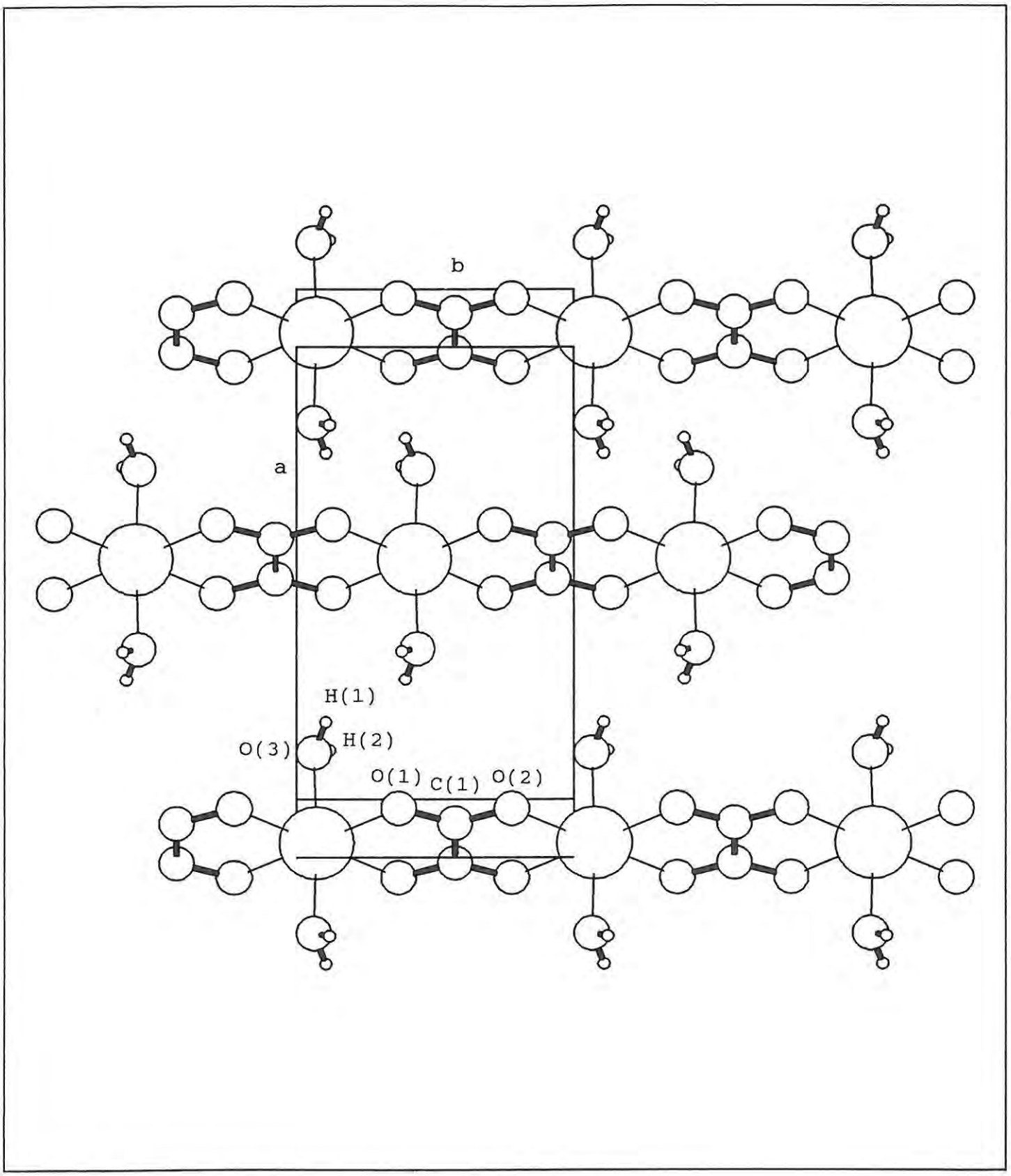

Figure 5.1 Packing diagram of $[Zn(C_2O_4)(H_2O)_2]_n$

and $Na_2[Cu(C_2O_4)].2H_2O$ (1.545 Å) [7]. A possible explanation is the Fe^{2+} and Cu^{2+} ions have vacant d-orbitals capable of accepting electron density from the oxalate ions, and this reduces the repulsion between the carboxylate groups which results in stronger C-C bonds whereas the Zn^{2+} ion does not posess vacant d-orbitals capable of accepting electron density from the oxalate groups.

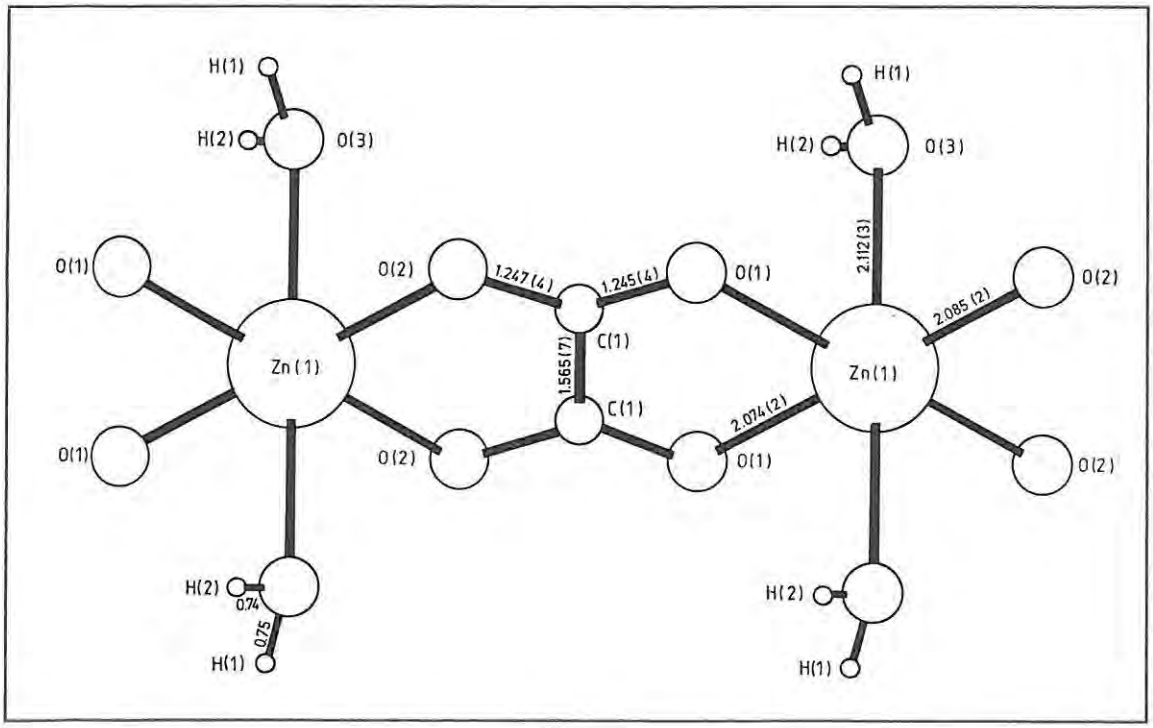

Figure 5.2 Ball-and-spoke diagram of a portion of one of the linear chains of $[Zn(C_2O_4)_2(H_2O)_2]_n$

CHAPTER 6

INDEXING THE POWDER DIFFRACTION PATTERNS OF THE MONOOXALATO COMPLEXES, $[M(C_2O_4)(H_2O)_2]_n$

In this section attempts were made to index the XRD patterns of the monoclinic monooxalates. Although several of the oxalates were indexed, including the mixed oxalates $MCu(C_2O_4)_2.3H_2O$, only the powder pattern of zinc oxalate dihydrate was indexed with certainty, but the general method is outlined here. Accurate powder data will be needed to continue this work.

The following equation can be used to index the XRD patterns of the monoclinic monooxalates $[M(C_2O_4)(H_2O)_2]_n$ [34]:

$$1/d^2 = (h^2/a^2 + l^2/c^2 + (2hl/ab)\cos\beta)/\sin^2\beta + k^2/b^2 \quad ...(1)$$

This equation contains four unknowns: a, b, c and β. However, the unit cell parameters a, b, c and β for $[Zn(C_2O_4)(H_2O)_2]_n$, were determined in Chapter 5 and can be used to index its powder pattern. Since the lattice dimensions of this group of oxalates can be expected to be similar, and their structures isomorphous, the powder pattern of $[Zn(C_2O_4)(H_2O)_2]_n$, once indexed, can be used to index the powder patterns of the other oxalates of this group.

Once the oxalates have been indexed, their lattice dimensions can be calculated. Although the above equation contains all four unknowns, it is a sum of several parts, and the calculation becomes simpler when one uses the pinacoid relections (h 0 0, 0 l 0, and 0 0 k). When l, k = 0 :

$$1/d^2(h\ 0\ 0) = (h^2/a^2)/\sin^2\beta \quad ....(2)$$

when h, k = 0:

$$1/d^2(0\ 0\ l) = (l^2/c^2)/\sin^2\beta \quad ....(3)$$

and when h, l = 0

$$1/d^2(0\ k\ 0) = k^2/b^2 \quad ....(4)$$

In the $C2/c$ space group, equation (4) cannot be used since the reflections (0 k 0) are forbidden. The lattice dimensions cannot be determined directly from the (h 0 0) and (0 0 l) reflections since equations (2) and (3) have two unknowns: the length of an edge of the unit cell and the interaxial angle, β. However, values for the lattice dimensions can be estimated, and then

checked by calculating *h k l* and comparing these values with the values of *h k l* determined from the diffraction pattern.

6.1 Indexing the powder pattern of zinc oxalate dihydrate

The unit cell parameters *a*, *b*, *c* and *ß* for $[Zn(C_2O_4)(H_2O)_2]_n$, determined in Chapter 5 are reproduced in Table 6.1. The relative intensities and positions of the powder diffraction lines of $[Zn(C_2O_4)(H_2O)_2]_n$ are shown in Table 6.2.

Table 6.1 Unit cell parameters for $[Zn(C_2O_4)(H_2O)_2]_n$

a/Å	11.786
b/Å	5.397
c/Å	9.712
ß/deg	126.19

The crystal structure of zinc oxalate dihydrate contains chains of $[Zn(C_2O_4)(H_2O)_2]$ units which lie parallel to the *b*-axis (Figure 6.1).

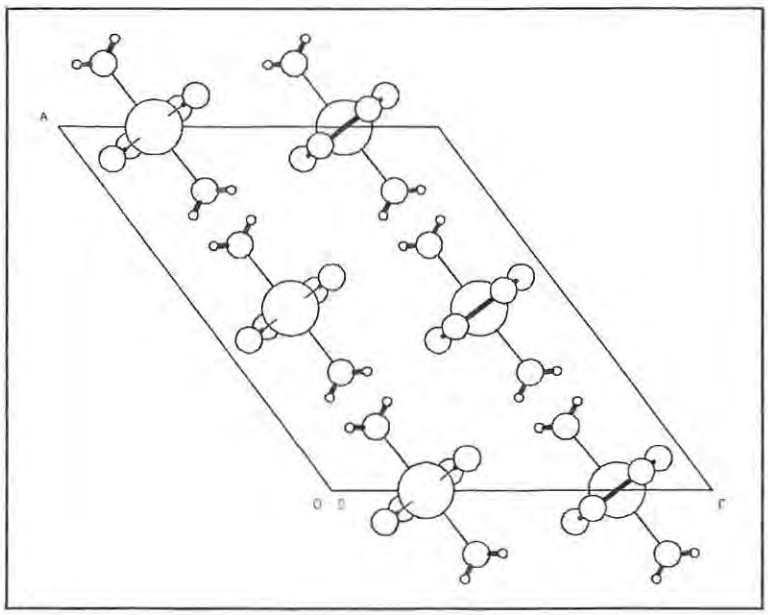

Figure 6.1 Packing diagram of $[Zn(C_2O_4)(H_2O)_2]_n$ viewed perpendicular to the stacking direction

Therefore the reflections *h* 0 0 are likely to be intense. The repeat distance of these planes is *a*/2 and the reflection (2 0 0) is likely to be the most intense. The spacing of these planes is:

$d(2\ 0\ 0) = \sin\beta/(2/a) = 4.756$ Å

The line at d = 4.76 Å (Table 6.2) is the most intense line in the diffraction pattern.

Equation (1) was transferred to a spreadsheet and the d-spacing of over 4 x 4 x 4 combinations of *h*, *k*, *l* were calculated. The calculated *d*-spacing of these planes were used to index the powder pattern of zinc oxalate dihydrate (Table 6.2).

Table 6.2 X-ray powder pattern of $[Zn(C_2O_4)(H_2O)_2]_n$

d/Å	*I*/*I*o x 100%	*h k l*	*d* calc./Å
4.76	100	2 0 0	4.756
3.92	20	0 0 2	3.919
3.55	5	-1 1 2	3.562
2.96	35	-4 0 2	2.946
2.70	5	0 2 0	2.699
2.55	20	0 2 1	2.551
2.22	10	0 2 2	2.223
2.08	7	-2 2 3	2.072
1.97	3	-5 1 4	1.983
1.92	7	-6 0 2	1.922
1.88	5	0 2 3	1.877
1.77	5	-1 3 1	1.766
1.59	4	4 2 1	1.594
1.48	4	-6 2 1	1.480
1.42	1	-5 3 3	1.424
1.33	2	0 4 1	1.330

CHAPTER 7

THE THERMAL ANALYSIS OF $Ba[Cu(C_2O_4)_2(H_2O)].5H_2O$

7.1 Stoichiometry of the thermal dehydration and decomposition

The masses of various possible products of the thermal decomposition of $Ba[Cu(C_2O_4)_2(H_2O)].5H_2O$, expressed as percentages of the starting material are shown in Table 7.1.

Table 7.1

Substance	Mass/ %
$Ba[Cu(C_2O_4)_2(H_2O)].5H_2O$	100
$Ba[Cu(C_2O_4)_2(H_2O)]$	81.4
$Ba[Cu(C_2O_4)_2]$	77.7
BaC_2O_4, CuC_2O_4	77.7
BaC_2O_4, Cu	59.6
BaC_2O_4, CuO	62.9
$BaCO_3$, Cu	53.8
$BaCO_3$, CuO	57.1
BaC_2O_4	46.5
$BaCO_3$	40.7
BaO, Cu	44.7
BaO, CuO	48.0
5 H_2O	18.6
H_2O	3.71
CO_2	9.07
CO	5.77

7.2 Non-isothermal thermogravimetry

The TG curve for $Ba[Cu(C_2O_4)_2(H_2O)].5H_2O$ heated at 10°C min^{-1} in flowing N_2 is shown in Figure 7.1. Dehydration starts at 79°C and reaches a maximum rate at 144°C. The low onset temperature is due to the presence of relatively weakly held water molecules in the crystal. At 179°C, 18.6 % of the sample mass has been lost, corresponding to loss of five water molecules per formula

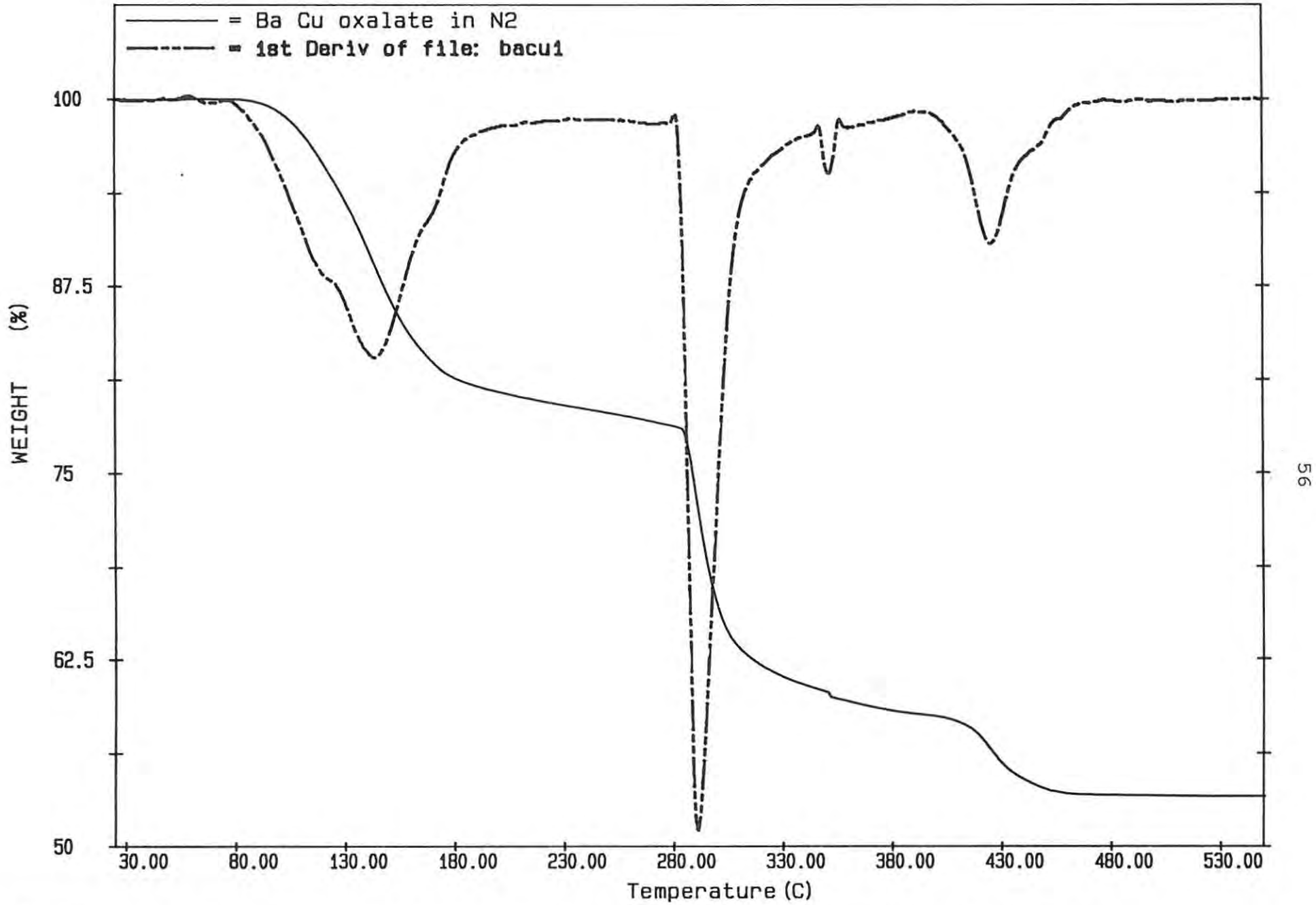

Figure 7.1 A TG curve for $Ba[Cu(C_2O_4)_2(H_2O)].5H_2O$ heated at 10°C min^{-1} in flowing N_2

unit. At this stage the rate of dehydration has slowed down considerably and the final water is lost in a much more gradual process between 179 and 280°C.

A photograph of the partially dehydrated crystals, together with crystals prior to the dehydration is shown in Figure 7.2. During the dehydration the crystals become opaque and lighter blue as the microstructure of the crystals is destroyed. Removal of the last stages of water coincides with the onset of the decomposition at 280°C. Initially the decomposition is rapid, and then decelerates to a gradual mass loss. At 380°C the sample mass is 59.6 % of its initial value. This mass corresponds to the formation of barium oxalate and copper metal (calculated mass = 59.5 %).

At 390°C a further decomposition stage occurs. A stable final mass of 53.4% of the initial mass is attained at 460°C. These results suggest that the decomposition, under these conditions, occurs in two major overlapping stages:

1) $Ba[Cu(C_2O_4)_2](s) \rightarrow BaC_2O_4(s) + Cu(s) + 2CO_2(g)$

2) $BaC_2O_4(s) \rightarrow BaCO_3(s) + CO(g)$

The final mass of the residue (53.7 %) compares well with the calculated mass (53.8 %) based on the formation of barium carbonate and copper metal. A photograph of the final residue is shown in Figure 7.3. The residue consists of small pseudo-crystals, typically 3 mm long. SEM showed that the surfaces of the these particles were extensively cracked (Figure 7.4) due to the contraction of the solid and escape of product gases during the decomposition. One of the product particles was lightly broken to observe the results of any phenomena that might have taken place beneath the surface. There were no obvious features such as large crystallites, or networks of cracks (Figure 7.5). At very high magnification, the crushed product appeared to be porous, and made up of extremely small particles (typically with diameters of 0.2 μm) (Figure 7.6).

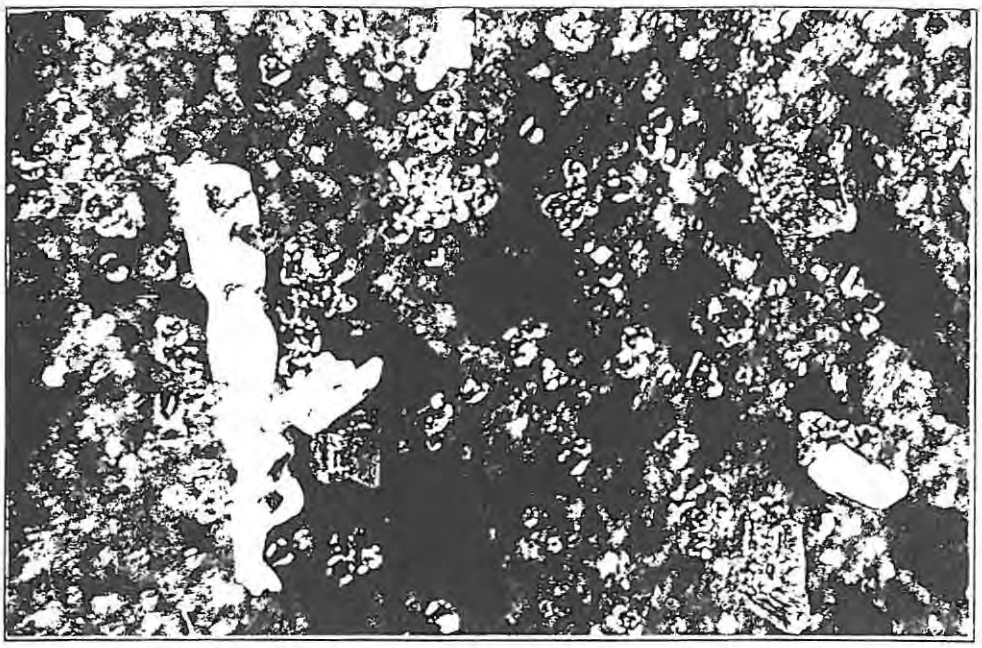

Figure 7.2 Crystals of barium bis(oxalato) cuprate(II) hydrate viewed using optical microscopy (x20). The clear, dark blue crystals are fully hydrated; the light blue, opaque crystals have been partially dehydrated

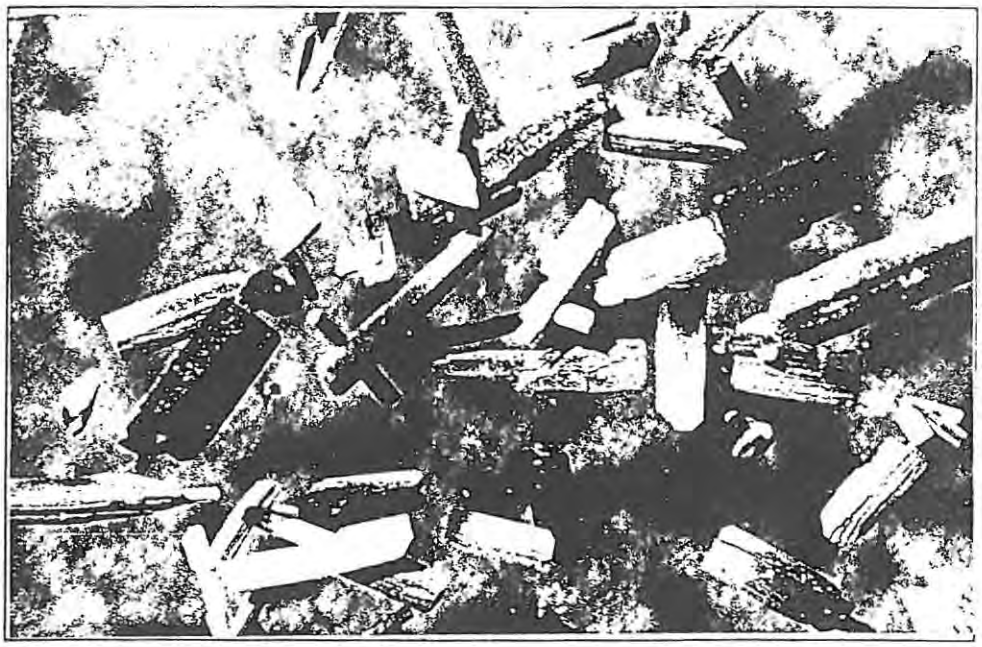

Figure 7.3 Optical micrograph of the solid product from the thermal decomposition of barium bis(oxalato) cuprate hydrate in N_2 (x20.)

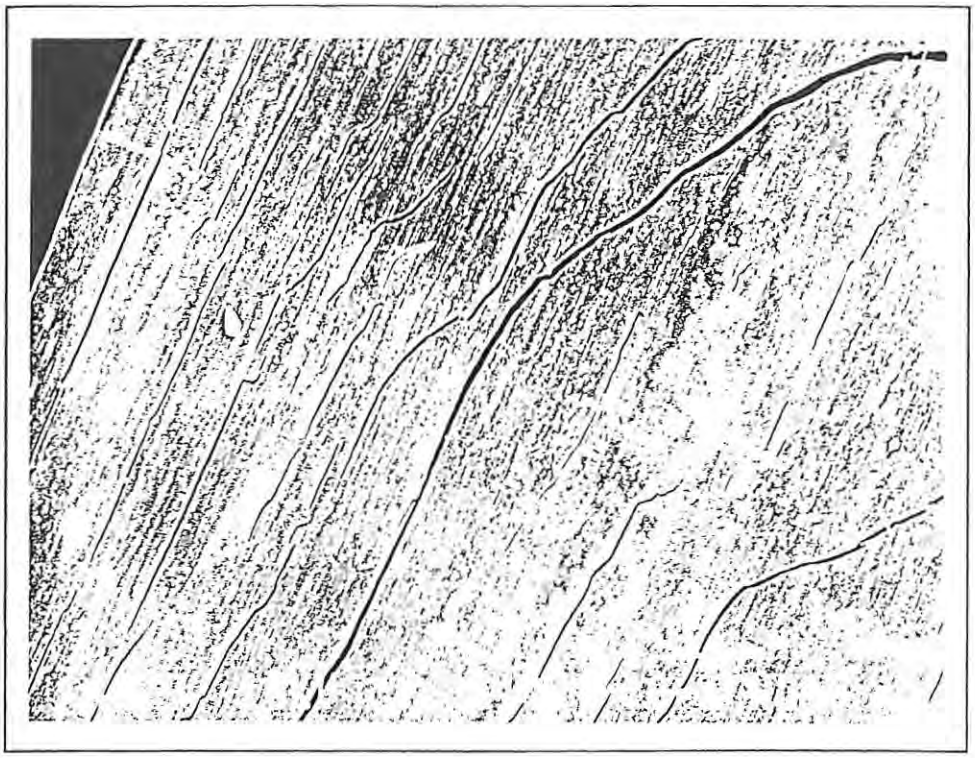

Figure 7.4 Scanning electron micrograph of the surface of a crystal after heating to 500°C at 20°C min^{-1}

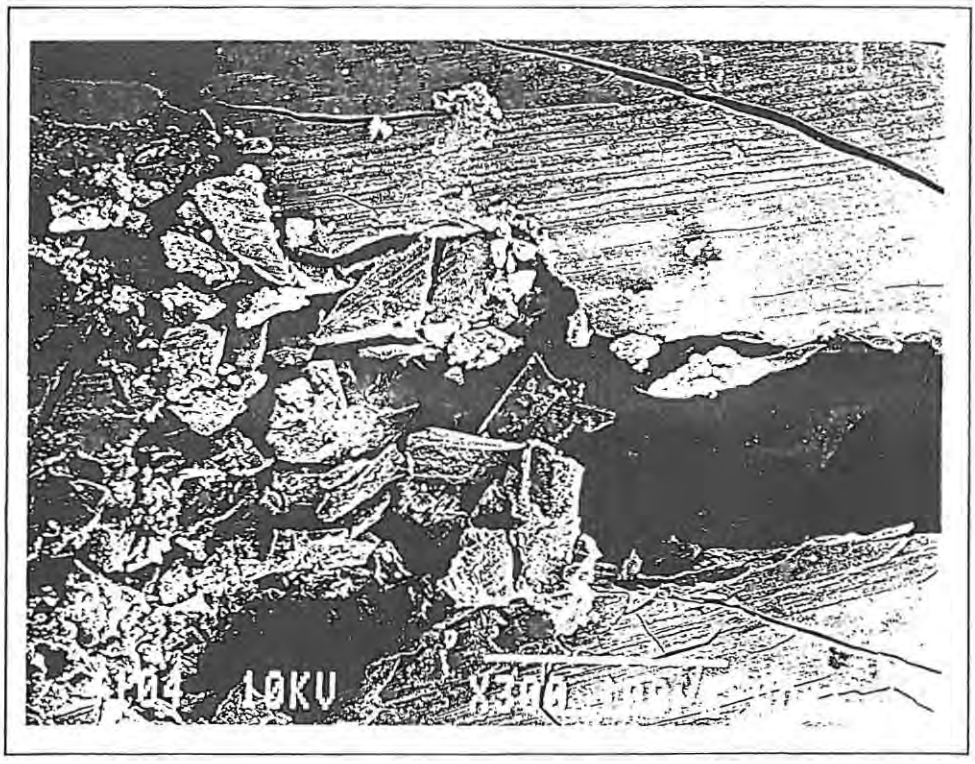

Figure 7.5 Scanning electron micrograph of a lightly crushed product particle

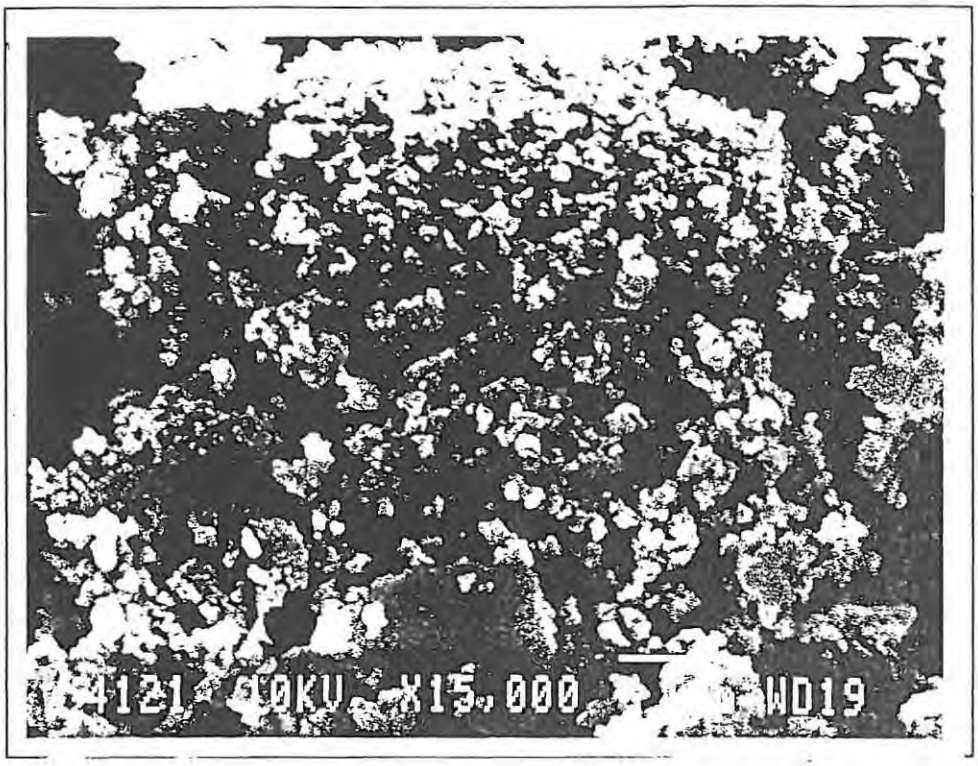

Figure 7.6 Scanning electron micrograph, at high magnification, showing the internal structure of the product particle shown above

The final residue from the decomposition and several solid intermediates were characterised by infrared spectroscopy (Chapter 8). The only infrared active material present in detectable concentrations in the final residue was ionic carbonate. The only possible counter ions are Ba^{2+} and Cu^{2+}. Copper(II) carbonate has a different infrared spectrum to barium (ionic) carbonate. The ionic carbonate is thus present as barium carbonate and this was confirmed by XRD. The infrared spectrum of the solid intermediate isolated at 380°C showed that bridging oxalate, barium carbonate and non-bridging oxalate were present. The infrared bands of the bridging oxalate were more similar to the bands of barium oxalate than copper oxalate. The temperature for the onset of the decomposition of barium oxalate is 400°C compared to 270°C for copper(II) oxalate. On the basis of the mass loss data, the bridging oxalate was more likely to be barium oxalate. This sample probably consists of barium carbonate, barium oxalate and unreacted bis(oxalato) cuprate(II). No estimate was made of the amount of each species present.

The DSC results, which are discussed below, also showed that the decomposition has several overlapping processes. The decomposition is thus complex, and cannot be clearly separated into two definite stages. The infrared spectrum of the intermediate obtained when the heating program was terminated at 320°C contained an absorption band due to the presence of the carbonate ion. The formation of barium carbonate (although perhaps in small quantities) thus occurs during the early stages of the decomposition. It is likely that stages (1) and (2), albeit at different rates, occur concurrently during the decomposition. The complex DSC curves for the decomposition support this.

As mentioned above, the crystal morphology was preserved during the entire reaction, but the collapse of the crystal structure occurs at a microscopic level during the dehydration. The final decomposition product (Figure 7.3) has a sooty appearance due to the presence of carbon formed by some disproportionation of carbon monoxide. The amount of carbon was probably not large, judging from the TG mass data.

7.3 Differential scanning calorimetry

The DSC curve for $Ba[Cu(C_2O_4)_2(H_2O)].5H_2O$ heated at 20°C min^{-1} in N_2 is shown in Figure 7.7. The curve shows an initial endothermic process with an onset temperature of 75°C, and the maximum is reached at 160°C. At 250°C a second small endothermic peak occurs, but is soon swamped by an exothermic process with overall maximum at 305°C. A second exothermic maximum occurs at about 410°C. The DSC and DTG (Figure 7.1) curves show some similarities.

The enthalpy for the dehydration, calculated from the area of the first peak, is 311 ±30 kJ mol^{-1}. The large uncertainty in this result arises from uncertainties in the baseline, since the dehydration continues until the onset of the decomposition. The second small endothermic peak (at 250°C), which precedes the large exothermic peak, was first thought to be due to the rupture of the copper-water coordinate bonds. The TG results show, however, that at this stage beyond five water molecules per formula unit have been lost. It was concluded, therefore, that the initial stages of the decomposition are endothermic.

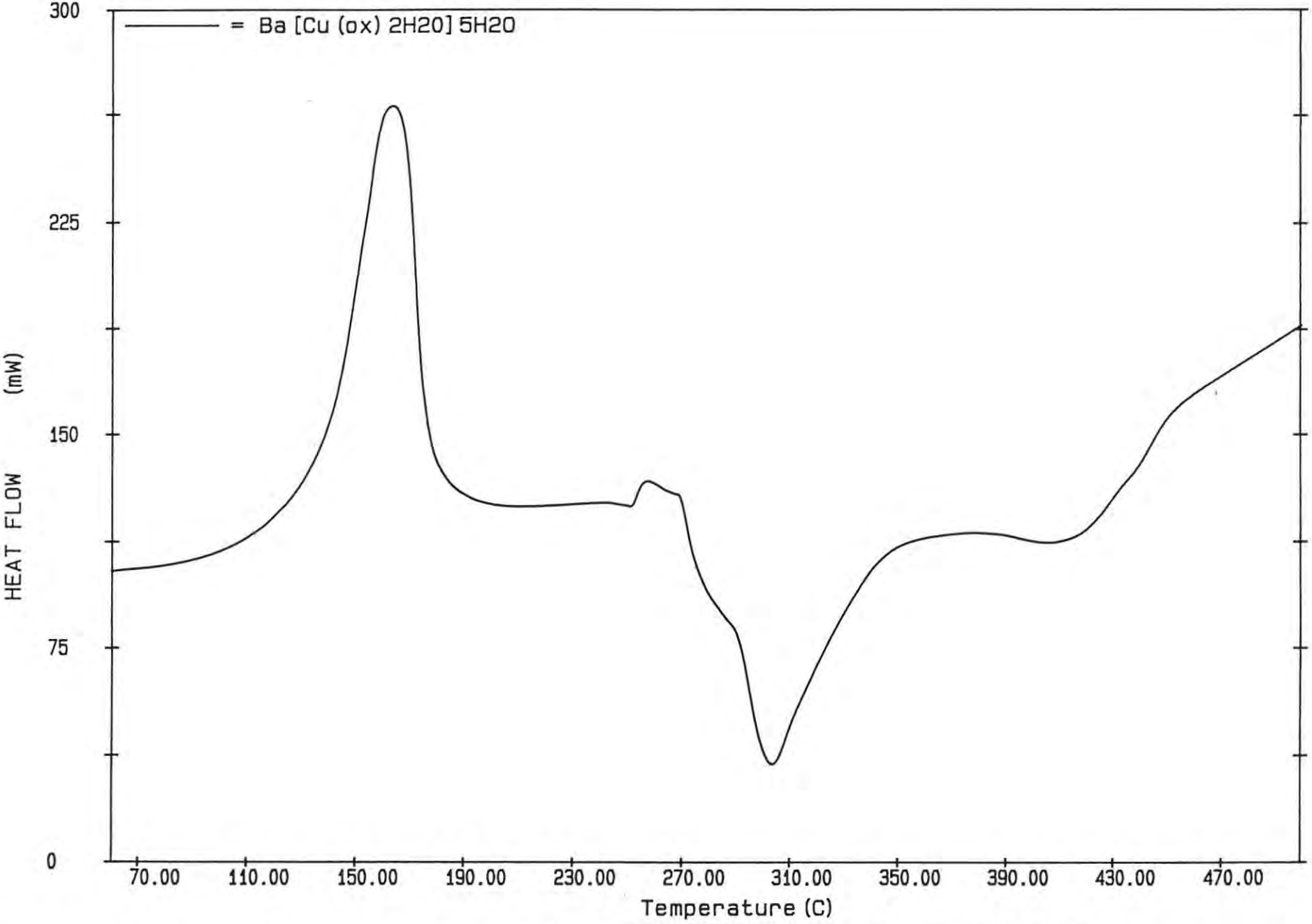

Figure 7.7 A DSC curve for $Ba[Cu(C_2O_4)_2(H_2O)].5H_2O$ heated at 20°C min^{-1} in flowing N_2

The small endothermic peak was also present in the DSC curve for barium oxalate hemihydrate.

The overall exothermic nature of the decomposition reaction is of interest since the decomposition of barium oxalate to barium carbonate (which is one of the reactions occurring in this decomposition) is known to be endothermic.

From the TG results, the first stage of the decomposition, and therefore the exothermic peak, was suggested to be largely due to the reaction:

$Ba[Cu(C_2O_4)_2](s) \rightarrow BaC_2O_4(s) + Cu(s) + 2CO_2(g)$ (mass loss = 18.1%)

The decomposition of copper oxalate is strongly exothermic with onset at about 290°C [1] which supports the reaction proposed above, although the exotherm observed for pure copper oxalate is much narrower, and less intense (-33 kJ mol^{-1} compared to -347 kJ mol^{-1}) [1]. The decomposition of dioxalato copper(II) ($[Cu(C_2O_4)_2]^{2-}$) is far more exothermic than monooxalato copper(II) ($[Cu(C_2O_4)]$).

The subsequent reaction:

$BaC_2O_4(s) \rightarrow BaCO_3(s) + CO(g)$ (mass loss = 5.8%)

is known to be endothermic. The thermal decomposition of pure BaC_2O_4 begins at 330°C and is complete at 550°C. The strong exothermic nature of reaction (1) would swamp any indication of the endothermic reaction. Also, the oxalate ion might be decomposing in a matrix different to that of pure barium oxalate. The TG results show that at 450°C the sample has reached its stable final mass corresponding to the formation of barium carbonate and copper metal. Since the thermal decomposition of $Ba[Cu(C_2O_4)_2]$ is complex with many overlapping processes (both exothermic and endothermic), accurate estimates of the enthalpy changes of the stages could not be made. An estimate of the overall enthalpy change was made by measuring the combined area of the overlapping peaks. This estimate of ΔH for the decomposition of $Ba[Cu(C_2O_4)_2]$ in N_2 is -347 kJ mol^{-1}.

The DSC curve for $Ba[Cu(C_2O_4)_2(H_2O)].5H_2O$ heated in O_2 is shown in Figure 7.8. The complex nature of the decomposition is again apparent from this curve, which shows many similarities to the curve obtained in N_2. The dehydration and the initial stages of

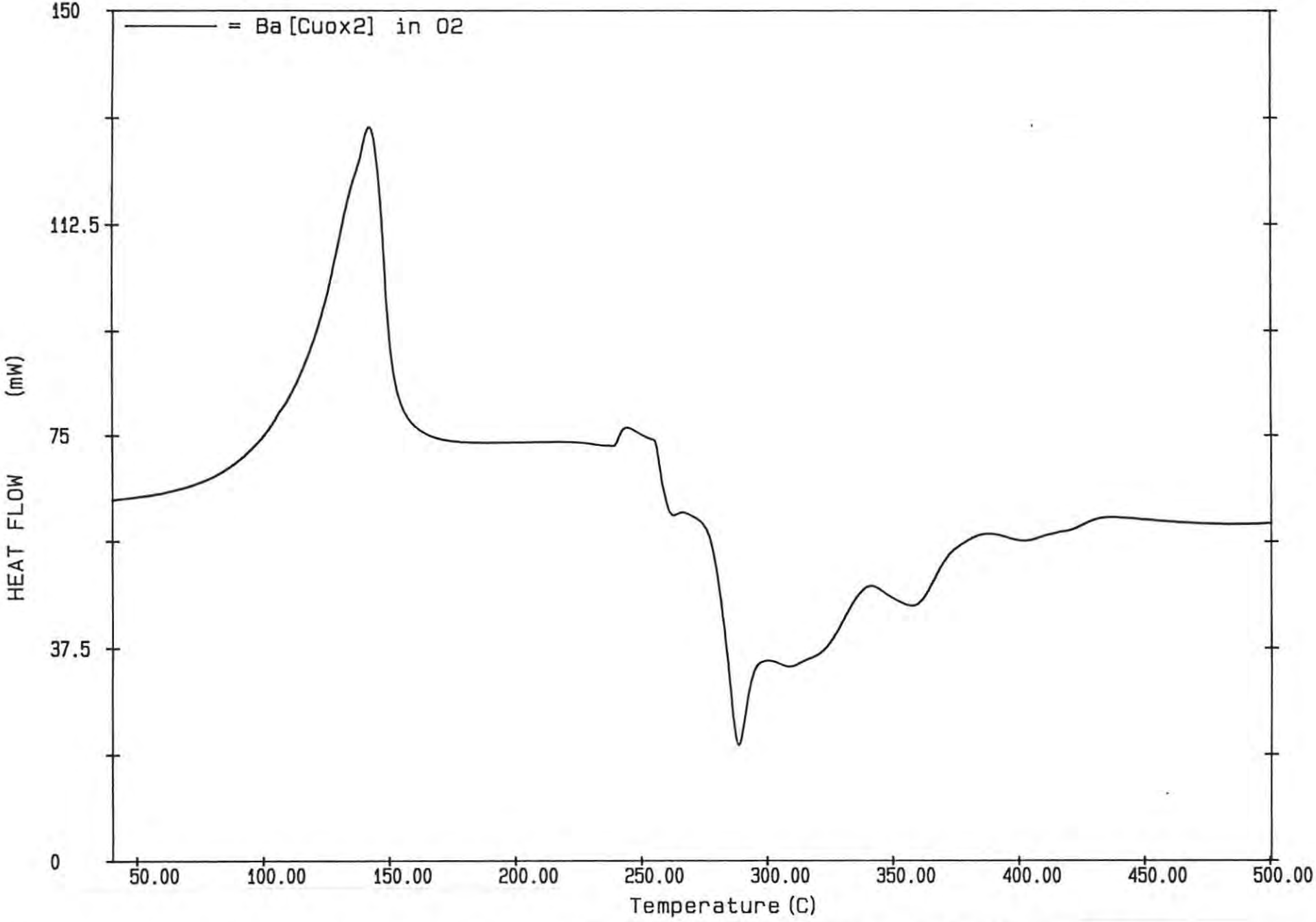

Figure 7.8 A DSC curve for $Ba[Cu(C_2O_4)_2(H_2O)].5H_2O$ heated at 20°C min^{-1} in flowing O_2

the decomposition appear to be similar in N_2 and in O_2 and are endothermic in both atmospheres. As found in N_2, the initial endothermic process is soon swamped by the main exothermic process, but, in O_2, the maximum is reached sooner. The later stages of the decomposition in O_2 are different to those in N_2. The main decomposition exotherm observed for the run in O_2 is much narrower than the one observed for N_2.

From the TG results, the first stage of the decomposition, and hence this exothermic peak, was suggested to be largely due to the reaction:

$Ba[Cu(C_2O_4)_2](s) + 0.5O_2(g) \rightarrow BaC_2O_4(s) + CuO(s) + 2CO_2(g)$

(calculated loss = 14.8 %, measured loss = 14.5 %)

Subsequently, the DSC curve becomes more complex with several broad overlapping exothermic peaks differing in intensity. It is possible that these exotherms mask any endothermic processes. An estimate of the overall enthalpy change for the thermal decomposition of $Ba[Cu(C_2O_4)_2]$ in O_2 was made by measuring the combined area of the overlapping peaks corresponding to the decomposition processes. This estimate of ΔH for the decomposition of $Ba[Cu(C_2O_4)_2]$ in O_2 is -457 kJ mol^{-1}, compared with -347 kJ mol^{-1} estimated in N_2.

7.4 Thermochemistry

The overall chemical reaction occurring during the thermal decomposition of $Ba[Cu(C_2O_4)_2]$ in N_2 is:

$Ba[Cu(C_2O_4)_2](s) \rightarrow BaCO_3(s) + Cu(s) + CO(g) + 2CO_2(g)$ (1)

which takes place via two steps:

$Ba[Cu(C_2O_4)_2](s) \rightarrow BaC_2O_4(s) + Cu(s) + 2CO_2(g)$ (2)

$BaC_2O_4(s) \rightarrow BaCO_3(s) + CO(g)$ (3)

Step (3) is known to be endothermic. Step (2) will be exothermic. The enthalpies of formation for various possible products and/or intermediates of the thermal decomposition of $Ba[Cu(C_2O_4)_2]$ are shown in Table 7.2 [35]. The value for the enthalpy of formation of anhydrous barium oxalate was estimated. The enthalpies of formation of $BaC_2O_4.2H_2O$ and $BaC_2O_4.1/2H_2O$ are -1970 and -1522 kJ mol^{-1}, respectively. The enthalpy of formation of anhydrous barium oxalate was taken to be somewhat less than

that of barium oxalate hemihydrate.

Table 7.2 The enthalpies of formation of various intermediates and products of the thermal decomposition

Substance	$-\Delta_f H^\ominus$ /kJ mol^{-1}
$BaC_2O_4.0.5H_2O(s)$	1522
$BaC_2O_4(s)$ (estimated)	1500
$BaCO_3(s)$	1219
Cu(s)	0
$CO_2(g)$	394
CO(g)	111
CuO(s)	155
$Cu_2O(s)$	167

For the overall reaction:

$$\Delta H(1) = \Delta_f H^\ominus BaCO_3(s) + \Delta_f H^\ominus Cu(s) + \Delta_f H^\ominus CO(g) + 2\Delta_f H^\ominus CO_2(g) - \Delta_f H^\ominus Ba[Cu(C_2O_4)_2](s)$$

For step (2):

$$\Delta H(2) = \Delta_f H^\ominus BaC_2O_4(s) + 2\Delta_f H^\ominus CO_2(g) + \Delta_f H^\ominus Cu(s) - \Delta_f H^\ominus Ba[Cu(C_2O_4)_2](s)$$

For step (3):

$$\Delta H(3) = \Delta_f H^\ominus BaCO_3(s) + \Delta_f H^\ominus CO(g) - \Delta_f H^\ominus BaC_2O_4(s)$$
$$= [-1219 - 111 -(-1500)] \text{ kJ mol}^{-1}$$
$$= +170 \text{ kJ mol}^{-1}$$

The value of ΔH for the overall decomposition of $Ba[Cu(C_2O_4)_2]$ in N_2 was estimated from the DSC curve and is -347 kJ mol^{-1}. The intense exothermic nature of the decomposition was surprising since the transformation of barium oxalate to barium carbonate is endothermic. Since the enthalpy of formation for $Ba[Cu(C_2O_4)_2]$ is not known, the enthalpy change for the overall reaction (1) and step (2) cannot be calculated, but the measured values of enthalpies of reaction can be used to estimate $\Delta_f H$ of the complex as described below.

7.4.1 Estimating the enthalpy of formation of $Ba[Cu(C_2O_4)_2]$

DSC runs in O_2 were used to estimate the enthalpy of formation of $Ba[Cu(C_2O_4)_2]$ because there are no uncertainties in the oxidation states of the products. The oxalate groups were completely oxidised to carbon dioxide and the copper was converted to copper(II) oxide. The overall reaction in O_2 is:

$$Ba[Cu(C_2O_4)_2](s) + O_2(g) \rightarrow BaCO_3(s) + CuO(s) + 3CO_2(g) \quad (4)$$

Again, the above reaction can be divided into two steps:

$$Ba[Cu(C_2O_4)_2](s) + 0.5O2(g) \rightarrow BaC_2O_4(s) + CuO(s) + 2CO_2(g) \quad (5)$$

$$BaC_2O_4(s) + 0.5O_2(g) \rightarrow BaCO_3(s) + CO_2(g) \quad (6)$$

For step (6):

$$\Delta H(6) = \Delta_f H^{\ominus} BaCO_3(s) + \Delta_f H^{\ominus} CO_2(g) - \Delta_f H^{\ominus} BaC_2O_4(s)$$

$$= -113 \text{ kJ mol}^{-1}$$

The thermal transformation of barium oxalate to barium carbonate in O_2 is thus predicted to be exothermic.

The enthalpy change for the overall reaction (4) in O_2 was estimated from the DSC curve as -457 kJ mol^{-1}. From the enthalpy change in O_2 an estimate of the enthalpy of formation of $Ba[Cu(C_2O_4)_2]$ was made:

$$\Delta_f H^{\ominus} Ba[Cu(C_2O_4)_2](s) = -\Delta H + \Delta_f H^{\ominus} BaCO_3(s) + \Delta_f H^{\ominus} CuO(s) + 3\Delta_f H^{\ominus} CO_2(g)$$

$$= -2099 \text{ kJ mol}^{-1}$$

Similarly in N_2:

$$\Delta_f H^{\ominus} Ba[Cu(C_2O_4)_2](s) = -\Delta H(1) + \Delta_f H^{\ominus} BaCO_3(s) + \Delta_f H^{\ominus} Cu(s) + \Delta_f H^{\ominus} CO(g) + 2\Delta_f H^{\ominus} CO_2(g)$$

$$= -1771 \text{ kJ mol}^{-1}$$

The discrepancy between the two estimates is due to the uncertainties in the enthalpy values measured from the DSC curves and possible uncertainties in the oxidation states of the products in N_2.

Chapter 8

CHARACTERISATION OF THE SOLID DECOMPOSITION PRODUCTS FROM THE THERMAL DECOMPOSITION OF $Ba[Cu(C_2O_4)_2(H_2O)].5H_2O$

8.1 Possible solid intermediates and products

According to the reaction scheme given in Chapter 7, the following compounds might appear as either intermediates or as stable products from the decomposition: $Ba[Cu(C_2O_4)_2]$, BaC_2O_4, $BaCO_3$, Cu, Cu_2O, CuO, CO and CO_2.

The products at the following stages of the decomposition were characterised by IR spectroscopy: the stage where the decomposition was complete (450°C) and the stage where step (1) of the decomposition was thought to be complete and where step (2) was thought to begin (380°C). The residue from one of the isothermal runs reported in Chapter 10 was also analysed. In addition to infrared spectroscopy, the XRD pattern of the final residue (450°C) was measured.

The XRD and IR data of the solid compounds suspected as being intermediates is set out in Tables 8.1 to 8.7. These tables were used to identify the various intermediates in the samples.

Table 8.1 XRD pattern of $BaCO_3$ [36]

d/Å	*I*/*Io*	*h k l*
4.56	9	1 1 0
4.45	4	0 2 0
3.72	100	1 1 1
3.68	53	0 2 1
3.215	15	0 0 2
3.025	4	0 1 2
2.749	3	1 0 2
2.656	11	2 0 0
2.628	24	1 1 2
2.590	23	1 3 0
2.281	6	2 2 0

Table 8.1 XRD pattern of $BaCO_3$ (continued)

d/Å	*I*/*Io*	*h k l*
2.226	2	0 4 0
2.150	28	2 2 1
2.104	12	0 4 1
2.048	10	2 0 2
2.019	21	1 3 2
1.940	15	1 1 3
1.859	3	0 4 2
1.677	5	3 1 1
1.649	4	133,241
1.633	4	1 5 1
1.563	3	2 2 3
1.521	4	3 3 0
1.375	6	3 3 2, 2 0 4
1.366	4	1 3 4
1.348	4	3 1 3, 0 6 2
1.335	3	2 4 3
1.328	4	4 0 0, 1 5 3
1.295	3	2 6 0

Table 8.2 XRD pattern for Cu (calculated)

d/Å	*I*/*Io*	*h k l*
2.0873	100	1 1 1
1.8076	43	2 0 0
1.2782	17	2 2 0
1.0901	13	3 1 1
1.0436	3	2 2 2

Table 8.3 XRD pattern of CuO [36]

d/Å	*I*/*Io*	*h k l*
2.751	12	1 1 0
2.530	49	0 0 2
2.523	100	-1 1 1
2.323	96	1 1 1
2.312	30	2 0 0
1.959	3	-1 1 2
1.866	25	-2 0 2
1.778	2	1 1 2
1.714	8	0 2 0
1.581	14	2 0 2
1.505	20	-1 1 3
1.418	12	0 2 2
1.410	15	-3 1 1,3 1 0
1.375	19	2 2 0, 1 1 3
1.304	7	3 1 1, -3 1 2, 2 2 1
1.265	6	0 0 4
1.262	7	-2 2 2
1.196	2	-2 0 4, -1 1 4

Table 8.4 XRD pattern of Cu_2O (cuprite) [36]

d/Å	*I*/*Io*	*h k l*
3.020	9	1 1 0
2.465	100	1 1 1
2.135	37	2 0 0
1.743	1	2 1 1
1.510	27	2 2 0
1.287	17	3 1 1
1.233	4	2 2 2
1.067	2	4 0 0

Table 8.5 Infrared absorptions of $BaCO_3$ [37]

ν/cm^{-1}	Assignment
1444	asymmetric stretch
861	out of plane bend
695	stretch and bend

Table 8.6 Infrared absorptions of BaC_2O_4

ν/cm^{-1}	Assignment
1610	ν_a(CO)
1334	ν_s(CO) + ν(C-C)
1316	ν_s(CO)
873	ν_s(CO) + δ(OCO)
777	δ(OCO) + ν(Ba-O)
532	ν(Ba-O)

Table 8.7 Infrared absorptions of $Ba[Cu(C_2O_4)_2(H_2O].5H_2O$

ν/cm^{-1}	Assignment
1680	ν_{as}(CO)
1638	ν_{as}(CO)
1425	ν_s(C-O) + ν(C-C)
1300	ν_s(C-O) + δ(OCO)
905,880	ν_s(C-O) + δ(OCO)
812	δ(OCO) + ν(Cu-O)
540	ν(Cu-O) + ν(C-C)
500	ring deformation
342	out of plane bend

8.2 Characterisation of the residue from non-isothermal TG

T = 500°C

This residue was assumed to be the final product of the decomposition. The mass loss, from the TG (46.3 %), was interpreted in terms of the residue being $BaCO_3$ and Cu (calculated loss = 46.2 %). If this were so, the only IR active material present would be the CO_3^{2-} ion. The CO_3^{2-} ion has three IR active modes of vibration. Two of these modes are degenerate and split on coordination to a metal ion. The infrared spectrum of the residue showed three peaks due to vibrations of the CO_3^{2-} ion. The positions and intensities of these three peaks are almost identical to those of $BaCO_3$. This is strong evidence that this sample contains $BaCO_3$.

Table 8.8 Infrared spectroscopic data for the solid residue from the thermal decomposition of $Ba[Cu(C_2O_4)_2(H_2O)].5H_2O$

$BaCO_3$	residue	Assignment
1450	1444	asymmetric stretch
860	861	out of plane bend
695	695	stretch and bend

The XRD pattern of the solid residue was of poor quality, with weak bands and large backround noise. The poor quality was probably due to scattering by carbon and amorphous material. The positions and intensities of the lines that could be measured are set out in Table 8.9. The values of the *d*-spacings as well as the intensities of all the reflections were very similar to those of the diffraction pattern of $BaCO_3$ (Table 8.1). The exception was a line at 1.37 Å.

Table 8.9 XRD pattern of the final residue from the decomposition of $Ba[Cu(C_2O_4)_2(H_2O].5H_2O$ from non-isothermal TG. The indexed lines are reflections from $BaCO_3$.

d/Å	*I*/*Io*	*h k l*
4.49	10	0 2 0
3.70	100	1 1 1
3.21	15	0 0 2
3.02	5	0 1 2
2.63	30	1 1 2
2.28	5	2 2 0
2.15	30	2 2 1
2.06	10	2 0 2
2.02	20	1 3 2
1.94	20	1 1 3
1.52	5	3 3 0
1.37	10	?
1.33	5	4 0 0, 1 5 3

Lines from diffraction by Cu (Table 8.2) could not be detected in the above pattern. The copper crystallites may be too small to scatter the X-rays efficiently.

T = 380°C

The mass of this sample (59.5 % of the initial mass) corresponded to the formation of BaC_2O_4 and Cu. The IR spectrum of this sample is shown in Table 8.10.

Table 8.10 Infrared absorptions of the residue from non-isothermal TG

ν/cm^{-1}	Assignment
1610	$\nu_a(CO)$
1420	$\nu_a(CO)$, $BaCO_3$
1310	$\nu_s(CO) + \nu(C-C)$, BaC_2O_4
855	out of plane bend, $BaCO_3$
845	$\nu_s(CO) + \delta(OCO)$
775	$\delta(OCO) + \nu(Ba-O)$, BaC_2O_4
750	$\delta(OCO) + \nu(Ba-O)$
695	CO_3^{2-}, stretch and bend
520	$\nu(M-O)$, probably Ba-O

The above spectrum contains a band at 695 cm^{-1}, which, of the possible products considered here, is unique for barium carbonate. An intense broad band at 1435 cm^{-1}, was thought to be due to the assymetric stretching mode of the carbonate ion. Thus barium carbonate is probably present in this sample.

This spectrum also contained bands similar to those of the spectrum of barium oxalate (1310, 775, 520 cm^{-1}).

Another substance was also present which was thought that to be unreacted $Ba[Cu(C_2O_4)_2]$. However, the strong absorption bands of $Ba[Cu(C_2O_4)_2]$ overlap with those of either barium carbonate or barium oxalate. The appearance of some of these bands, particularly the one at 1310 cm^{-1}, suggests that there are unresolved combinations of two or more bands.

There is no evidence for the presence of copper(II) oxalate in the sample.

8.3 The residue from an isothermal TG experiment (260°C)

The final mass attained, after heating a sample for 30 minutes, at 260°C, was 61.5 % of the initial mass of the hydrate. On the basis of this information it was thought that the sample consists mainly of BaC_2O_4 and Cu (i.e. 59.6 % of the initial mass). The infrared spectrum of this sample (Table 8.11) contained the same bands as the infrared spectrum of barium oxalate (Table 8.6) as well as an additional band which was thought to be due to the assymetric stretching mode of the CO_3^{2-} ion.

Table 8.11 Infrared absorptions of the residue from the decomposition of $Ba[Cu(C_2O_4)_2(H_2O].5H_2O$ from an isothermal run at 260°C

ν/cm^{-1}	Assignment
1615	BaC_2O_4, $\nu_a(CO)$
1435	CO_3^{2-}, $\nu_a(CO)$
1313	BaC_2O_4, $\nu_s(CO) + \nu(C-C)$
1310	BaC_2O_4, $\nu_s(CO) + \delta(OCO)$
770	BaC_2O_4, $\delta(OCO) + \nu(Ba-O)$
690	CO_3^{2-}, $\nu(OCO)$ stretch and bend

These infrared results show that barium oxalate is an intermediate in the thermal decomposition. Unlike $Ba[Cu(C_2O_4)_2(H_2O)].5H_2O$ and CuO which have a strong absorption band at 500 cm^{-1} due to copper(II)-oxygen stretching modes, absorption bands due to copper(II)-oxygen stretches were not observed for this sample. This provides strong evidence that the copper is not present as copper(II) oxide.

8.4 Conclusions

The infrared and XRD studies suggest that the decomposition is complex and cannot be clearly separated into two steps. The formation of carbonate appears to take place at quite early

stages of the reaction.

Barium oxalate appears to be a stable intermediate in the reaction, whereas copper(II) oxalate did not appear to be produced, which is in agreement with the hypothesis that electron-transfer is in the rate-limiting step in the reaction (see Discussion).

The IR spectra and XRD pattern of the final residue showed that barium carbonate is a stable final product. The XRD pattern did not show what form the copper was present but, on the basis of the IR spectra, which did not show copper(II)-oxygen stretches, and the mass loss data, the copper appears to be present in the zero oxidation state.

CHAPTER 9

THE KINETICS AND MECHANISM OF THE ISOTHERMAL DEHYDRATION OF $Ba[Cu(C_2O_4)_2(H_2O)].5H_2O$.

9.1 Isothermal α-time curves

The kinetics and mechanism of the dehydration of $Ba[Cu(C_2O_4)_2(H_2O)].5H_2O$ were determined using isothermal thermogravimetry in the temperature range 85 to 105°C, in an atmosphere of flowing N_2. The isothermal dehydration curves showed smooth, continuous, deceleratory mass losses suggesting that no stable intermediate hydrates are formed. The dehydration curves were deceleratory throughout with the final stages of the reaction being very slow, even at higher temperatures. At low temperatures, the final stages were too slow to enable the reaction to approach completion in a reasonable time. As the temperature was increased, the initial region became virtually linear. This behaviour is typical of reactions controlled by diffusion. At the lowest temperature used, 85°C, the sample lost 11.1 % of its mass after 100 minutes, corresponding to loss of approximately three water molecules per formula unit. At the highest temperature used, 105°C, the extent of dehydration in 100 minutes had increased to 16.7 %, corresponding to the loss of approximately five water molecules (Figure 9.1).

The curves of mass loss against time were converted to α-time curves, where α is the fractional dehydration calculated on the removal of five H_2O molecules, i.e. 18.6 % of the original sample mass (Figure 9.2).

The dehydration curve of crystals ground to a fine powder had a similar appearance to that of the original crystals, except that the initial stages were not as rapid and constituted a larger mass loss than the long, slow final stage of the dehydration.

9.2 Kinetic analysis

The integral and derivative functions for models commonly used in solid state kinetics are shown in Table 9.1.

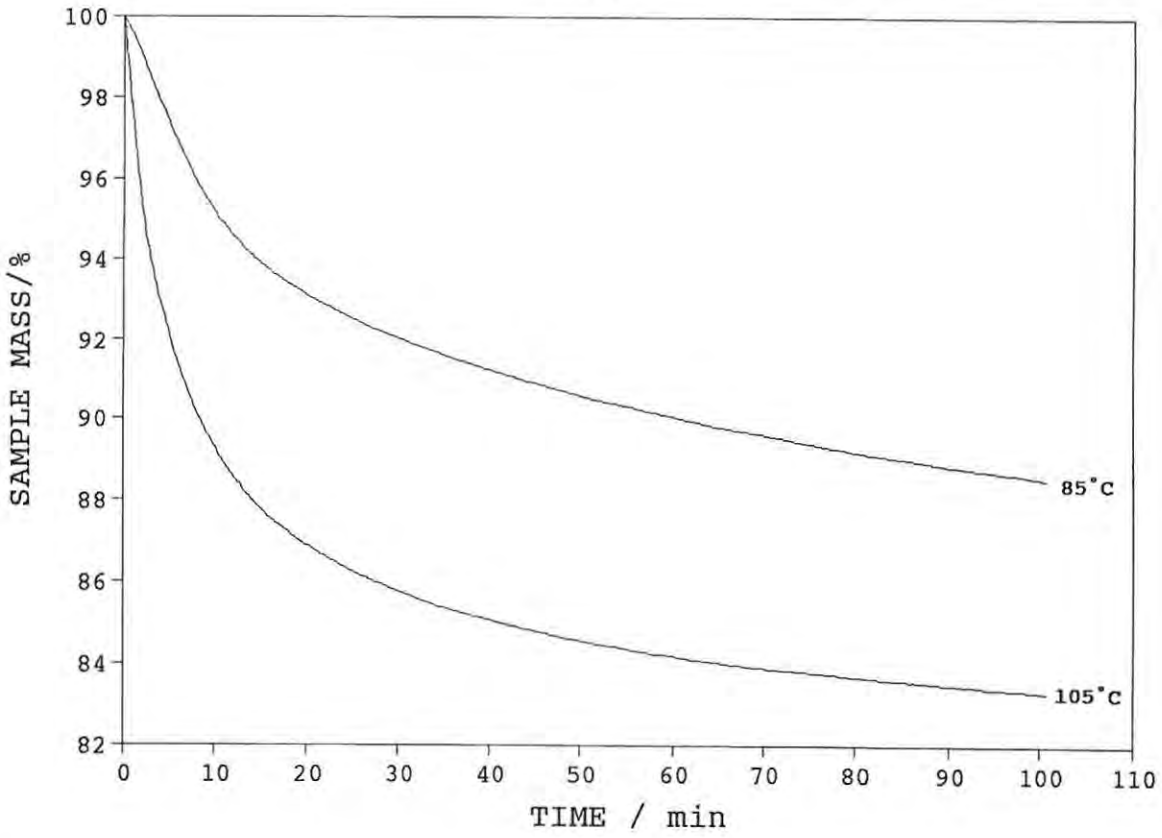

Figure 9.1 Isothermal TG curves for $Ba[Cu(C_2O_4)_2(H_2O)].5H_2O$ at 85 and 105°C in flowing N_2

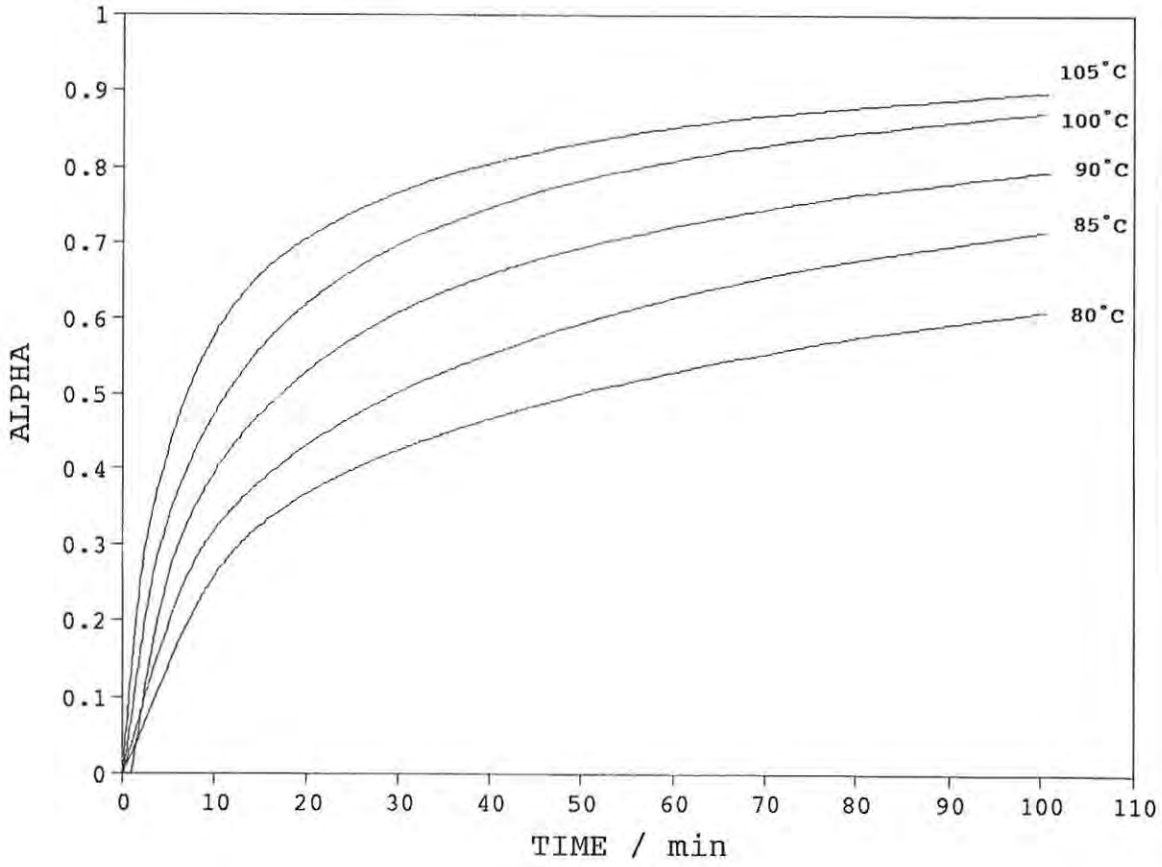

Figure 9.2 Fraction of reaction (α) against time curves from isothermal TG experiments at 85, 90, 95, 100 and 105°C

Table 9.1 The main rate equations for solid-state reactions

	$f(\alpha) = k(t' - t_o) = kt$	$g(\alpha) = 1/k\ d\alpha/dt$	$\alpha = h(t)$
1 Acceleratory			
P1 power law	$\alpha^{1/n}$	$n(\alpha)^{(n-1)/n}$	
E1 exponential law	$\ln\alpha$	α	
2 Sigmoid			
A2 Avrami-Erofeev	$[-\ln(1 - \alpha)]^{1/2}$	$2(1 - \alpha)(-\ln(1 - \alpha))^{1/2}$	
A3 Avrami-Erofeev	$[-\ln(1 - \alpha)]^{1/3}$	$3(1 - \alpha)(-\ln(1 - \alpha))^{2/3}$	
A4 Avrami-Erofeev	$[-\ln(1 - \alpha)]^{1/4}$	$4(1 - \alpha)$	
B1 Prout-Tompkins	$\ln[\alpha/(1 - \alpha)]$	$\alpha(1 - \alpha)$	$(1 + 1/\exp(kt)))^{-1}$
3 Deceleratory α-time curves			
3.1 Geometrical models			
R2 contracting area	$1 - (1 - \alpha)^{1/2}$	$2(1 - \alpha)^{1/2}$	$1 - (1 - kt)^n$
R3 contracting volume	$1 - (1 - \alpha)^{1/3}$	$3(1 - \alpha)^{2/3}$	
3.2 Diffusion models			
D1 one-dimensional	α^2	$1/2\alpha$	$(kt)^{1/2}$
D2 two-dimensional	$(1 - \alpha)\ln(1 - \alpha) + \alpha$	$(-\ln(1 - \alpha))^{-1}$	
D3 three-dimensional	$[1 - (1 - \alpha)^{1/3}]^2$	$3/2(1 - \alpha)^{2/3}(1 - (1 - \alpha)^{1/3})^{-1}$	$1 - (1 - (kt)^{1/2})^3$
D4 Ginstling-Brounshtein	$(1 - (2\alpha/3) - (1 - \alpha)^{2/3})$	$3/2(1 - \alpha)^{-1/3} - 1)^{-1}$	
3.3 'Order of reaction'			
F0 zero order	α	1	kt
F1 first order	$-\ln(1 - \alpha)$	$1 - \alpha$	$1 - \exp(-kt)$
F2 second order	$[1/(1 - \alpha)] - 1$	$(1 - \alpha)^2$	$1 - 1/(kt + 1)$
F3 third order	$[1/(1 - \alpha)^2] - 1$	$(1 - \alpha)^3$	$1 - (1/(kt + 1))^{1/2}$

NOTES: (1) Rate coefficients, k are different in each expression and times, t, are assumed to have been corrected for any induction period, t_o.

(2) The units of k are always expressed as $(\text{time})^{-1}$. In those equations incorporating an exponent, the correct notation is $\alpha = k^n t^n$ and not $\alpha = kt^n$.

The most appropriate rate law which described the dehydration was determined by judging the linearity of the plots of the linear form of the standard deceleratory models (f(α)) against time. The diffusion models gave the best fits. Plots for the Jander equation [38] (the three-dimensional diffusion or D3 model) were the most linear for all the isothermal dehydrations studied here. The goodness-of-fit, measured by the square of the correlation coefficient, r, for the linear regression and the associated rate constants for the different diffusion models, for the α-range 0.10 - 0.77, are shown in Table 9.2.

Table 9.2 The rate constants and goodness-of-fit (r^2) for the diffusion models at different temperatures for the isothermal dehydration of $Ba[Cu(C_2O_4)_2(H_2O)].5H_2O$ (α range: 0.10 to 0.77)

Model	r^2	Rate constant (k x 10^{-3} min^{-1})
T = 85°C		
D1	0.9606	3.54 ± 0.03
D2	0.9755	2.37 ± 0.02
D3	0.9997	0.73 ± 0.04
D4	0.9980	0.56 ± 0.04
T = 90 °C		
D1	0.9731	3.60 ± 0.02
D2	0.9908	2.73 ± 0.02
D3	0.9998	1.38 ± 0.01
D4	0.9953	0.71 ± 0.01
T = 95 °C		
D1	0.9769	5.34 ± 0.01
D2	0.9799	4.03 ± 0.05
D3	0.9999	2.57 ± 0.01
D4	0.9965	2.05 ± 0.06
T = 100 °C		
D1	0.9762	10.7 ± 0.2
D2	0.9928	8.04 ± 0.05
D3	0.9999	4.13 ± 0.01
D4	0.9968	3.08 ± 0.02

Table 9.2 (Continued)

Model	r^2	Rate constant (k x 10^{-3} min^{-1})
T = 105 °C		
D1	0.9601	30.3 ± 0.3
D2	0.9972	22.5 ± 0.2
D3	0.9962	6.78 ± 0.01
D4	0.9882	5.54 ± 0.03

The rate constants determined from the plots of the different diffusion models against time were used to calculate the theoretical curves of fractional dehydration (α) against time. A comparison of the calculated α-time curve, based on the Jander (D3) model, with the experimental $\alpha(t)$ curve for the experiment at 85°C is shown in Figure 9.3.

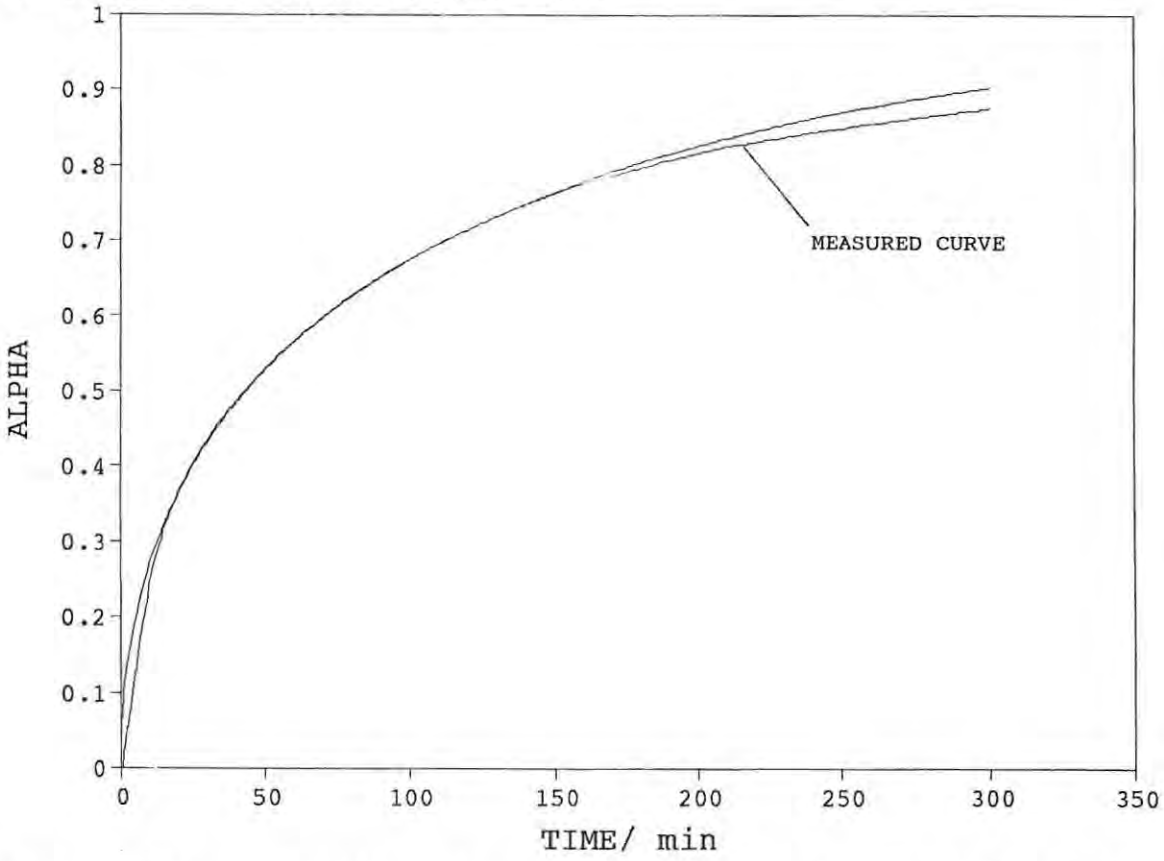

Figure 9.3 Comparison between the calculated and the measured α-time curves at 85°C

The D3 model produces an α-time curve which is almost identical to the actual reaction curve for the α-range 0.20 to 0.77. The dehydration kinetics were not as well described by the other diffusion models.

The rate coefficients from the D3 model were then used in an Arrhenius plot (Figure 9.4, Table 10.1).

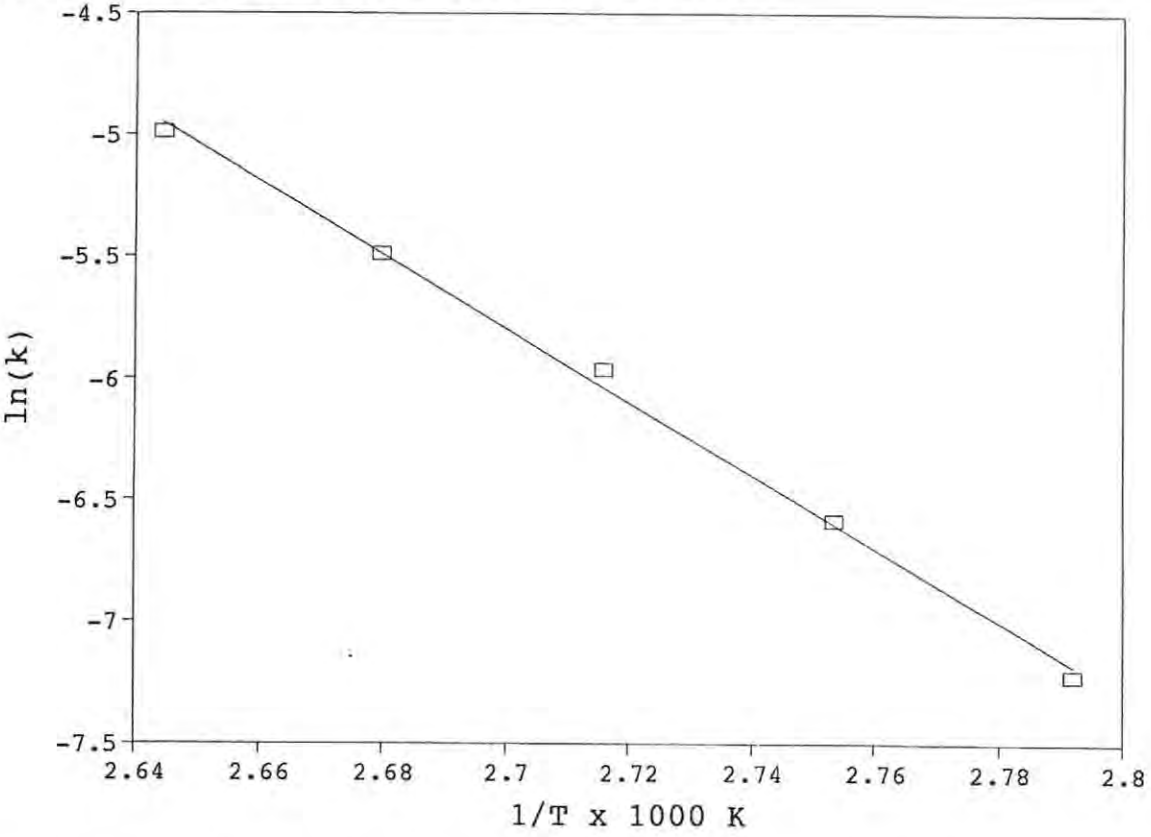

Figure 9.4 Arrhenius plot for the dehydration of $Ba[Cu(C_2O_4)_2(H_2O)].5H_2O$ using rate constants from the D3 model

The apparent activation energy, obtained from the above plot, was 125 ±4 kJ mol^{-1} and the pre-exponential factor was $(1.38 \pm 0.08) \times 10^{15}$ min^{-1}.

9.3 Discussion

The results of the kinetic analysis, suggest that the rate determining step in the dehydration of $Ba[Cu(C_2O_4)_2(H_2O)].5H_2O$ is the three-dimensional diffusion of water vapour through the layer of solid product. The X-ray diffraction results have shown that $Ba[Cu(C_2O_4)_2(H_2O)].5H_2O$ contains water molecules in two different

environments. One water molecule is directly bonded to the copper(II) ion, the five remaining water molecules are weakly held to the barium ion. The barium-water distances vary. The water molecules which are not complexed to the copper(II) take part in hydrogen bonding to each other and to the dioxalato-anion. Since the positions of the hydrogen atoms could not be located during the structure refinement, the details of the hydrogen bonding, as well as the interactions between the water molecules and the anions and barium ions could not be determined.

The rate limiting step in the overall process of dehydration is the diffusion of the product gases through the layer of solid product, so differences in the way the water molecules are held in the crystal will not show up in the isothermal dehydration. This could be visualised in terms of a build up of water, already dissociated from its original sites, in pockets or chambers in the crystal, waiting to escape.

The activation energy for the dehydration (125 ±4 kJ mol^{-1}) of $Ba[Cu(C_2O_4)_2(H_2O)].5H_2O$ is significantly less than the enthalpy of reaction (ΔH = 311 ±30 kJ (mol of complex)$^{-1}$). According to the transition state reaction profile of an endothermic reaction, the activation energy, E_a, for an endothermic process cannot be less than the enthalpy of reaction, ΔH. The problem, however, lies in reconciling the definitions of the amount of substance referred to in the E_a and ΔH values. The mole upon which the E_a value is based arises through the use of the gas constant, R and hence, in terms of transition state theory, would refer to "mole of activated complexes". Enthalpy values, however, are based upon a stated stoichiometry which can be adjusted as required. On the presumption that $E_a \geq \Delta H$ when the mole referred to is the same amount of material, it may be necessary to divide ΔH by a factor n. In this case $\Delta H/6$ is equal to 51.8 kJ mol^{-1}. This value may be compared with the enthalpy of vaporisation of water (40.7 kJ mol^{-1}). The isothermal dehydration of copper(II) sulphate pentahydrate has been described as being analogous to the evaporation of water [39]. However, as mentioned above, the rate determining step is not the process of breaking the bonds which hold the water molecules (hydrogen bonds etc.) in the

crystal lattice, but the transport of the dissociated water molecules through the solid. Therefore, on this basis alone, the complete process of the isothermal dehydration of $Ba[Cu(C_2O_4)_2(H_2O)].5H_2O$ is not analogous to the evaporation (although certain steps in the overall process may be similar).

The activation energy for the isothermal dehydration of $K_2[Cu(C_2O_4)].2H_2O$ was reported to be 116 kJ mol^{-1} [13].

Insausti *et al.* [40] prepared $Sr_2[Cu(C_2O_4)_3(H_2O)_2].5H_2O$ as a possible precursor to the mixed oxide Sr_2CuO_3. TG studies showed that dehydration occured in three consecutive endothermic steps (2:2:3). The ΔH for the overall dehydration was 54 kJ mol^{-1}.

Chapter 10

THE KINETICS OF THE THERMAL DECOMPOSITION OF $Ba[Cu(C_2O_4)_2]$

10.1 Isothermal α-time curves

Isothermal TG experiments in N_2 at a series of temperatures between 230 and 260°C were carried out to determine the kinetics and the mechanism of the decomposition. Each sample was dehydrated under the same conditions before each run: heated to 180°C at a rate of 20°C min^{-1} and held at that temperature for 10 minutes, before increasing the temperature at 20°C min^{-1} to the value used to study the decomposition. The last traces of water were very difficult to remove and, even when the sample reached the decomposition temperature, there was always a small amount of water trapped in the solid. Removal of these last traces of water coincided with the decomposition and care had to be taken when deciding where the dehydration ended and where the decomposition began.

The decomposition (after the preliminary dehydration) was thought to take place in two stages:

1) $Ba[Cu(C_2O_4)_2](s) \rightarrow BaC_2O_4(s) + Cu(s) + 2CO_2(g)$

2) $BaC_2O_4(s) \rightarrow BaCO_3(s) + CO(g)$

As discussed in Chapters 7 and 8, these two reactions overlap, with step (2) occurring slowly at first and becoming more significant at 380°C. Although the temperature range of these isothermal runs is significantly lower than the temperatures reported at which the decomposition barium oxalate → barium carbonate takes place, IR spectroscopy of the solid residues showed that barium carbonate was present in the reaction product in significant proportions.

Examples of typical mass-time curves at high temperatures (260°C) and at low temperatures (235°C) are shown in Figure 10.1.

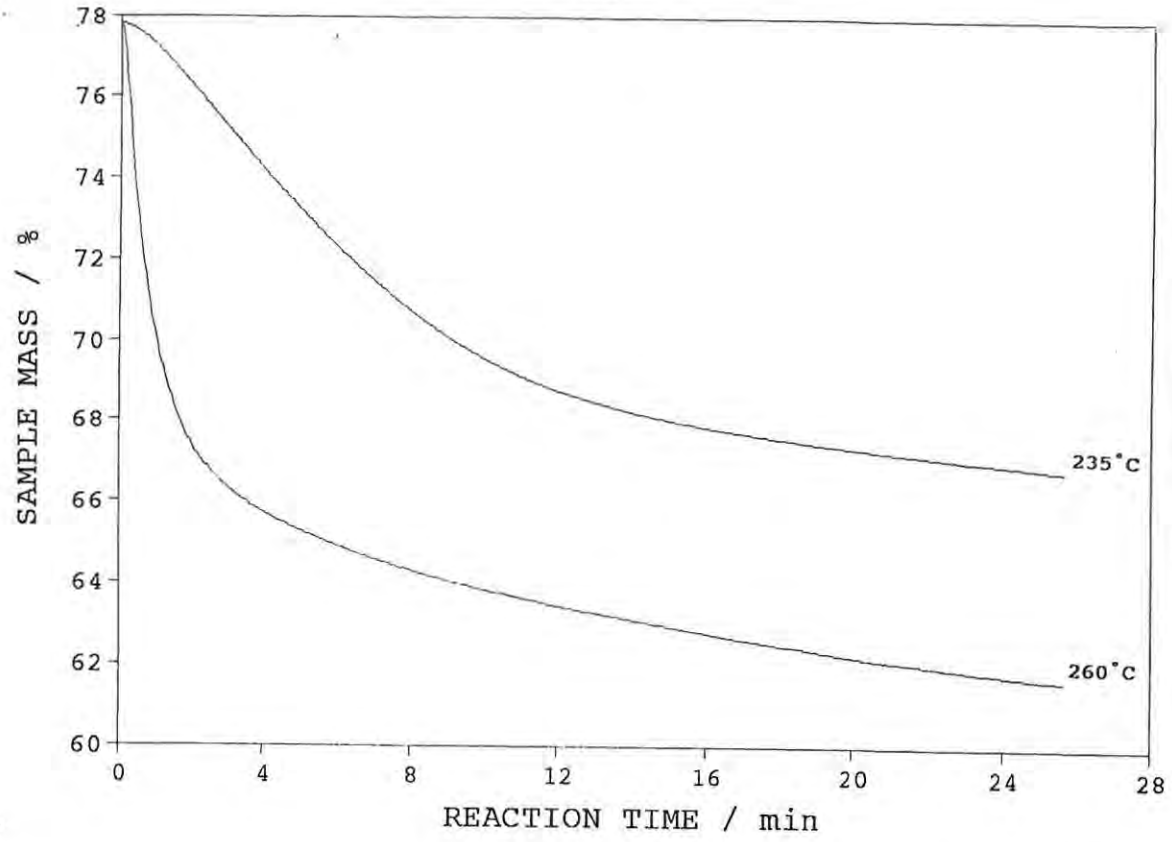

Figure 10.1 Isothermal TG curves for $Ba[Cu(C_2O_4)_2(H_2O)].5H_2O$ at 235 and 260°C in flowing N_2

The curves consist of at least three stages:
(a) an initial acceleratory stage
(b) a deceleratory stage
(c) a slow final stage.
Stages (a) and (b) are far more rapid than the final stage. The mass-time curves are smooth and the different reaction steps do not show up in the isothermal decomposition. There is a thus a problem in defining the extent of decomposition, α. At the highest isothermal temperatures used (260°C, Figure 10.1), the mass appears to be tending towards a final value of 61 %. Formation of barium oxalate and copper metal corresponds to a residue of 59.6 % of the initial mass of the of the hydrate. The α-time curves were calculated on the basis of α = 1.00 when the mass of the final solid residue is 59.6 % of the initial mass of the hydrate. The α-time curves for the runs at 235, 240 and 250°C are shown in Figure 10.2.

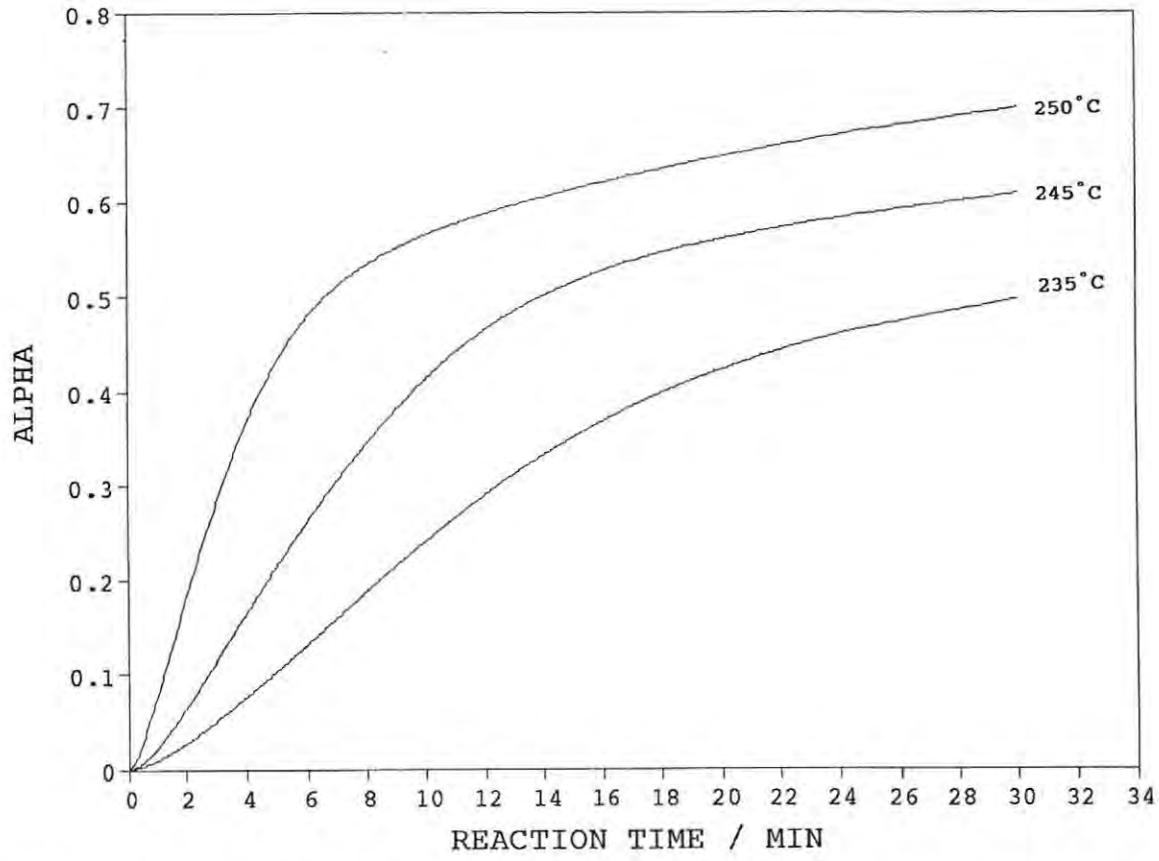

Figure 10.2 Fraction of reaction (α) against time curves from isothermal TG experiments at 235, 240, and 250°C

It is immediately qualitatively apparent that the initial stages (a) and, especially (b), have significant temperature dependences, whereas the final stage (c) has a lesser temperature dependence, remaining relatively slow over the whole temperature range and becoming negligibly slow, on the time scale used, at the low temperature end of the range (235°C).

In attempting a kinetic analysis of the α-time curves given in Figure 10.2., several simplifications were necessary. The initial acceleratory process which accounts for only a small portion of the decomposition was ignored. Its acceleratory nature is only clearly evident at the lower temperatures and, as the temperatures used were increased, this stage merges with the main stage (b). As a very approximate estimate of the kinetic parameters of stage (b), the slopes of the approximately linear regions of the α-time curves were used as a measure of the rate

coefficients. This is equivalent to assuming zero-order kinetic behaviour:

$d\alpha/dt = k_o$

Since many deceleratory curves may be described by the "order of reaction" type rate equations:

$d\alpha/dt = k_n(1 - \alpha)^n$

k_o is a good approximation for k_n when α is small.

Values of k_o, when used in an Arrhenius plot (Figure 10.3) gave an activation energy, E_a, of 215 ±22 kJ mol^{-1} and pre-exponential factor, A = (6.4 ±0.5) x 10^{21} min^{-1}.

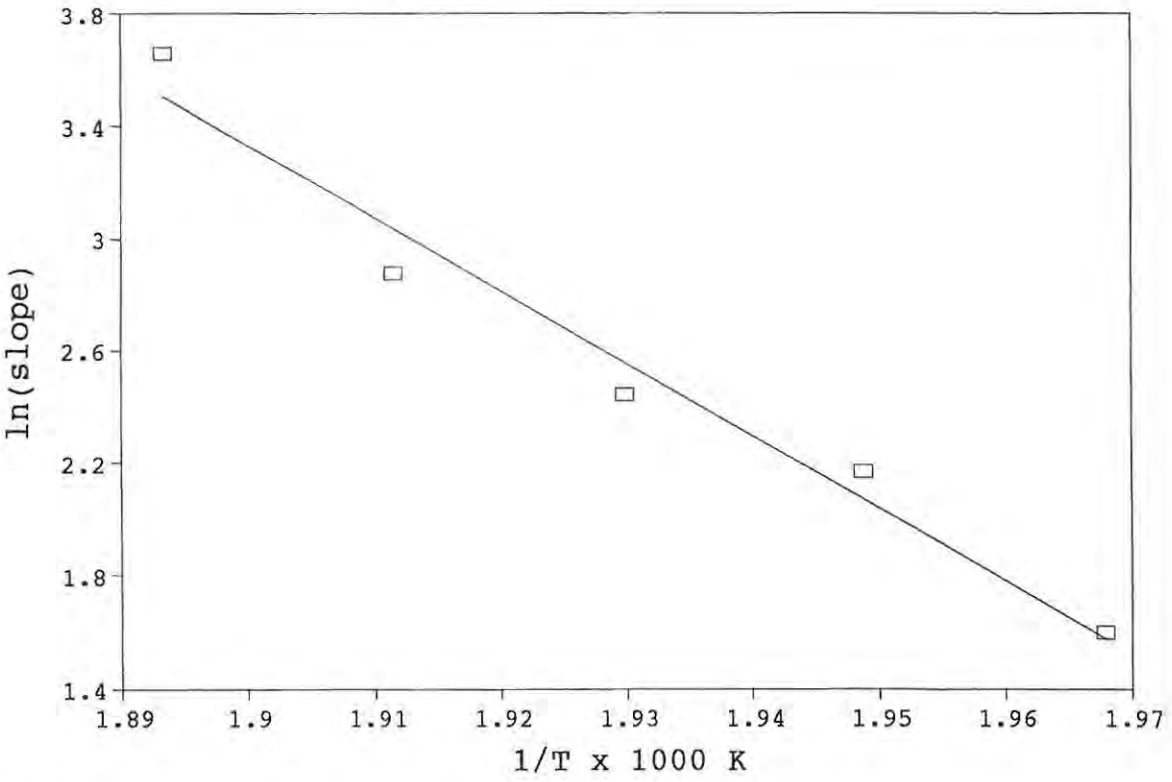

Figure 10.3 Arrhenius plot for the decomposition of $Ba[Cu(C_2O_4)_2(H_2O)].5H_2O$ using rate constants estimated from the slopes of the the initial regions of the α-time curves

To make a more detailed kinetic analysis, it is necessary to attempt to separate the contribution of the final process (c) from that of (b). There are two possibilities for process (c): (i) it is a concurrent process, starting at t = 0 and proceeding independently of (a) and (b);

(ii) it is a consecutive process, dependent on the previous occurrence of some reaction, e.g.,

$A \rightarrow P \rightarrow Q$

The second alternative (consecutive reactions) is chemically more attractive because of the evidence for the two processes:

1) $Ba[Cu(C_2O_4)_2](s) \rightarrow BaC_2O_4(s) + Cu(s) + 2CO_2(g)$

2) $BaC_2O_4(s) \rightarrow BaCO_3(s) + CO(g)$

The following kinetic analysis was applied for each run. It was assumed that the decomposition could be described by a rate equation of the form:

$d\alpha/dt = k_1 f_1(\alpha) + k_2 f_2(\alpha)$

The rate ($d\alpha/dt$) against time (t) curves were calculated using a 9-point Savitzky-Golay algorithm [41]. Plots of rate ($d\alpha/dt$) against time for the experiments at 235 and 255°C are shown in Figures 10.4 and 10.5.

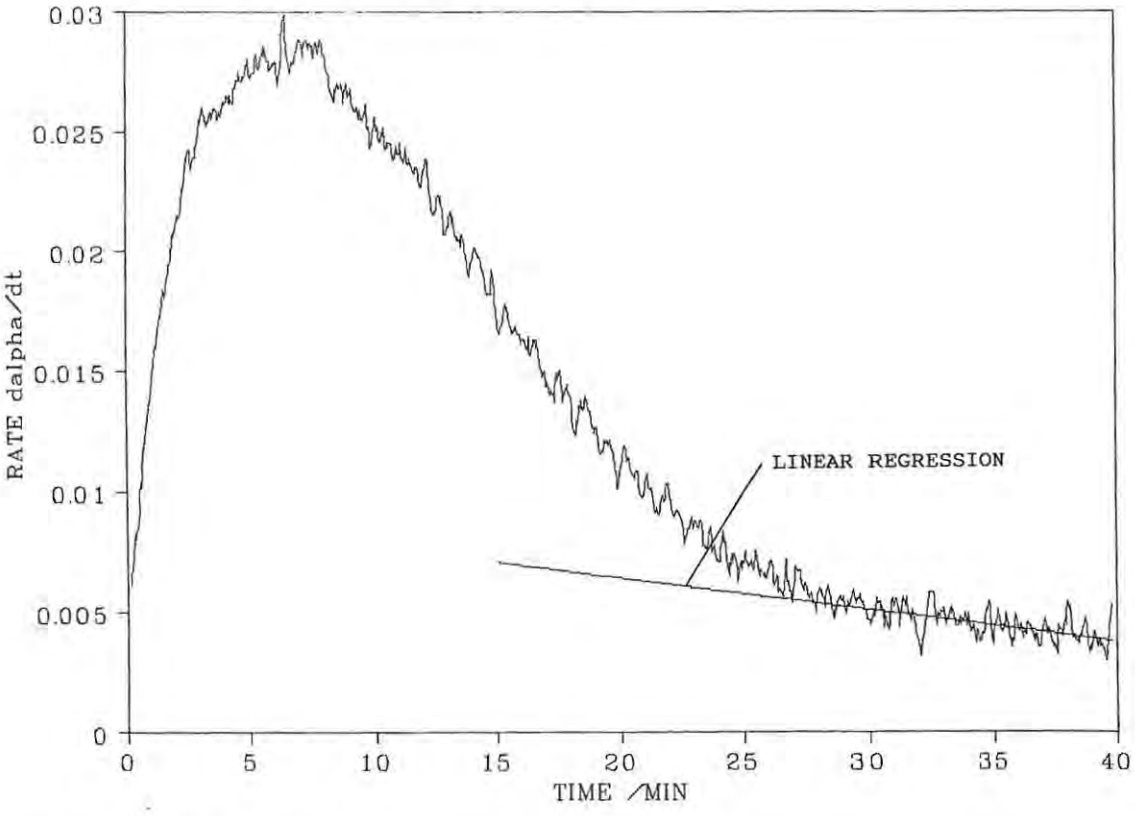

Figure 10.4 Rate of reaction ($d\alpha/dt$) against time for the isothermal experiment at 235°C

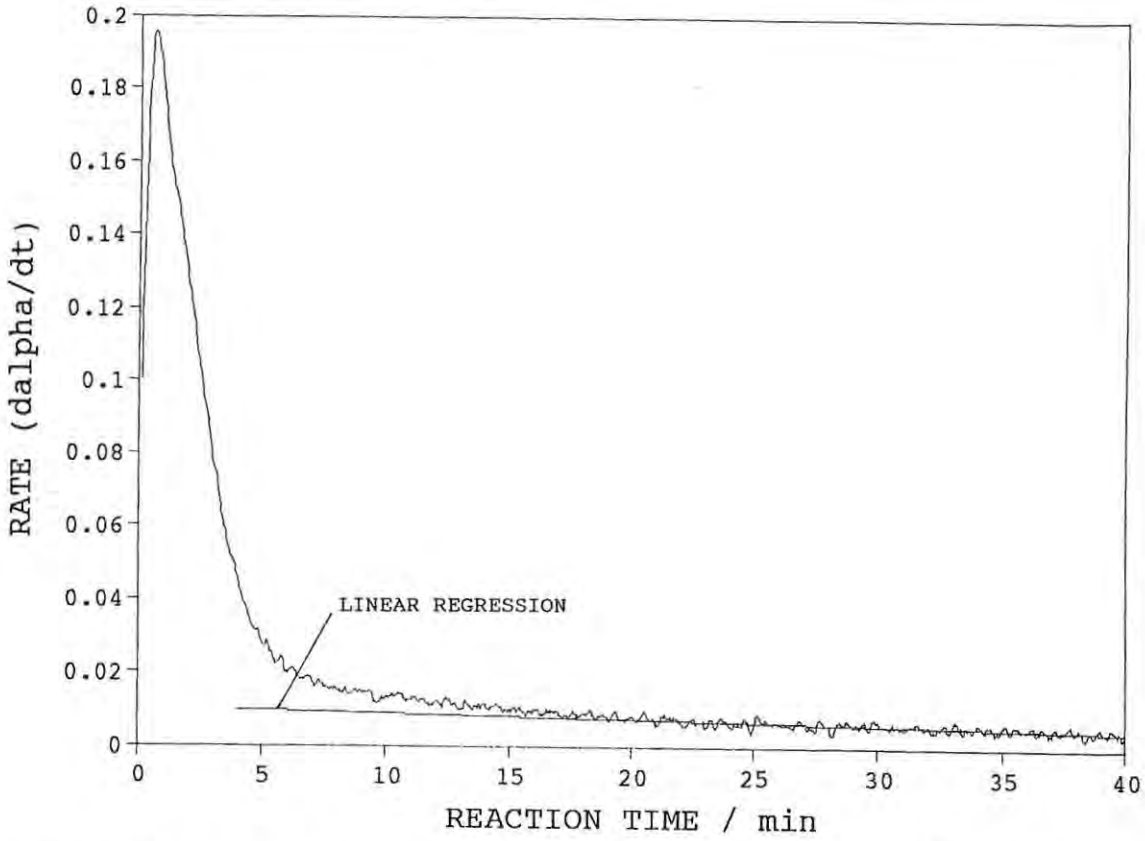

Figure 10.5 Rate of reaction ($d\alpha/dt$) against time for the isothermal experiment at 255°C

The later sections of the $d\alpha/dt$ curves are approximately linear. Such behaviour corresponds to the R2 model. The derivative form of the R2 model is:

$$d\alpha_2/dt = -2k_2(1 - kt)$$
$$= -2k_2 + 2k_2^2t$$

Linear regression was peformed on the linear region. The values of the slope ($2k_2^2$) and the intercept ($-2k_2$) were obtained from each regression. The rate constant, k_2, was estimated from both the slope and the intercept of the regression. The values from the slope, rather than the intercept, were used to calculate k_2. The slow process, $k_2f(\alpha)_2$, was then subtracted from the total rate to give $rate_1$. $Rate_1$ was then fitted empirically by an equation of the form

$$d\alpha/dt = n\ k_1(1 - k_1(t - t_o))^{(n-1)}$$

which for the case of $n = 2$ corresponds to the contracting-area equation (R2), and for $n = 3$ to the contracting volume equation

(R3). (t_o is a correction to the time scale to allow for the possibility that the model equation does not apply from the zero of the experimental curve.) As the value of n is increased, the concave-up shape of the resulting curve becomes more pronounced. k_1 was adjusted to bring the calculated curve into the required range.

Use of $n = 3$ did not produce sufficient curvature, so it was decided to fit the experimental curves by empirical adjustment of the three variables n, k and t_o using a sum of squares of the residual deviations, $\Sigma(\text{rate(expt.)} - \text{rate(model)})^2$ to optimize the fit.

An alpha-time curve was then reconstructed from the two contributions:

$d\alpha/dt = d\alpha_1/dt + d\alpha_2/dt$

By integration and weighting.

$\alpha_1 = \alpha(Rn) = 1 - (1 - k_1(t - t_o))^{(n+1)}$

$\alpha_2 = \alpha(R2) = 1 - (1 - k_2 t)^2$

$\alpha_{TOTAL} = w_1\alpha_1 + w_2\alpha_2$

Good matches were obtained by trial-and-error. The small correction, t_o, which was needed in the derivative curve was often not needed in the integrated curve.

Isothermal TG at 255°C

The $d\alpha/dt$ against time curve at the highest temperature used, 255°C, is shown in Figure 10.5. The $d\alpha/dt$ against time curve with α plotted on the same axis is shown in Figure 10.6. Linear regression over the time range 20 to 40 minutes gave a slope, $m_2 = -2k_2 = -1.51 \times 10^{-4}$ min^{-1} and therefore $k_2 = 8.7 \times 10^{-3}$ min^{-1}, and, an intercept, $c = 0.0105$. The value of k_2, from the intercept, is 5.2×10^{-3} min^{-1}. The value for k_2 obtained from the slope was used to calculate the slow process ($rate_2$). The slow process was then subtracted from the total rate to give $rate_1$. A plot of $rate_1$ against time is shown in Figure 10.7. The fit with $n = 5$, $k_1 = 0.078$, and $t_o = -1.42$ min is shown in Figure 10.8. By trial-and-error, a good match between experimental and calculated α-time curves was obtained with the following:
$w_1 = 0.5$, $k_1 = 0.078$, $t_o = 0$, $n = 5$, $w_2 = 0.6$, and $k_2 = 0.0087$
This is shown in Figure 10.9. A correction t_o (= -1.42 min) is needed in the derivative curve but not the integrated curve.

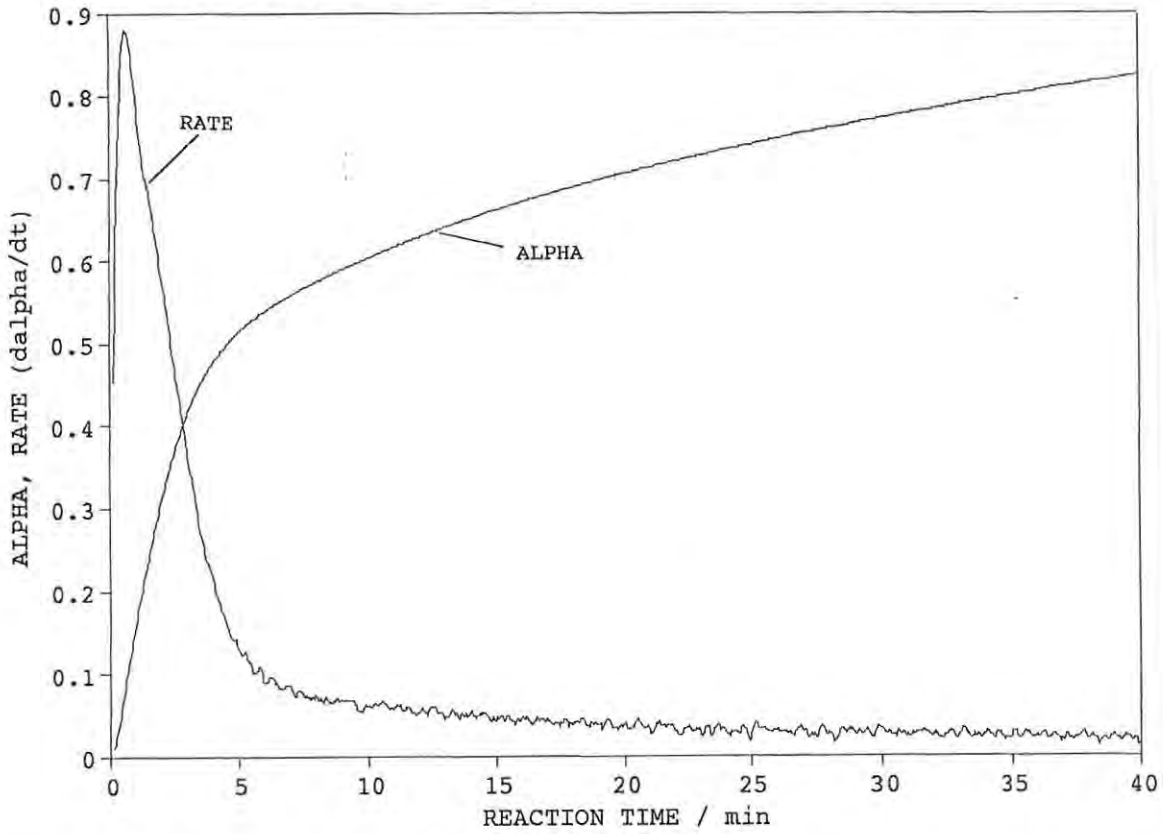

Figure 10.6 Rate of reaction ($d\alpha/dt$) against time, with α plotted on the same axis, for the isothermal experiment at 255°C

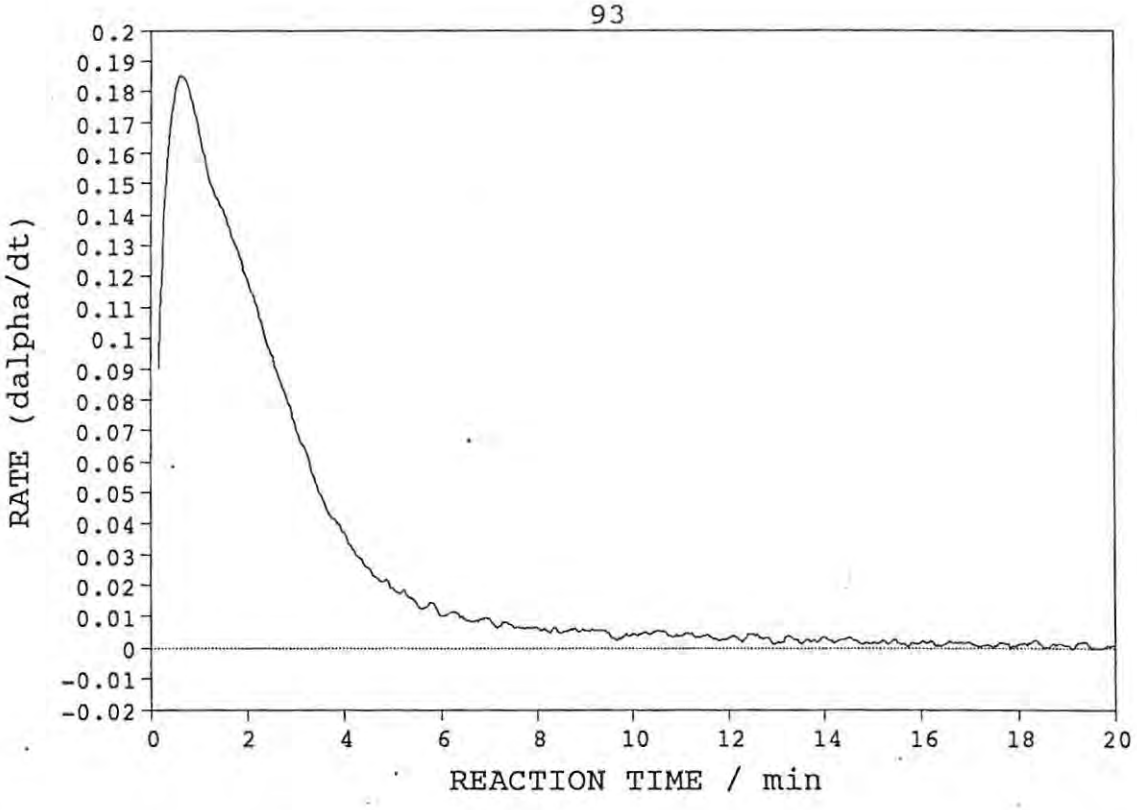

Figure 10.7 Corrected rate of reaction ($d\alpha_1/dt$) against time curve for the run at 255°C

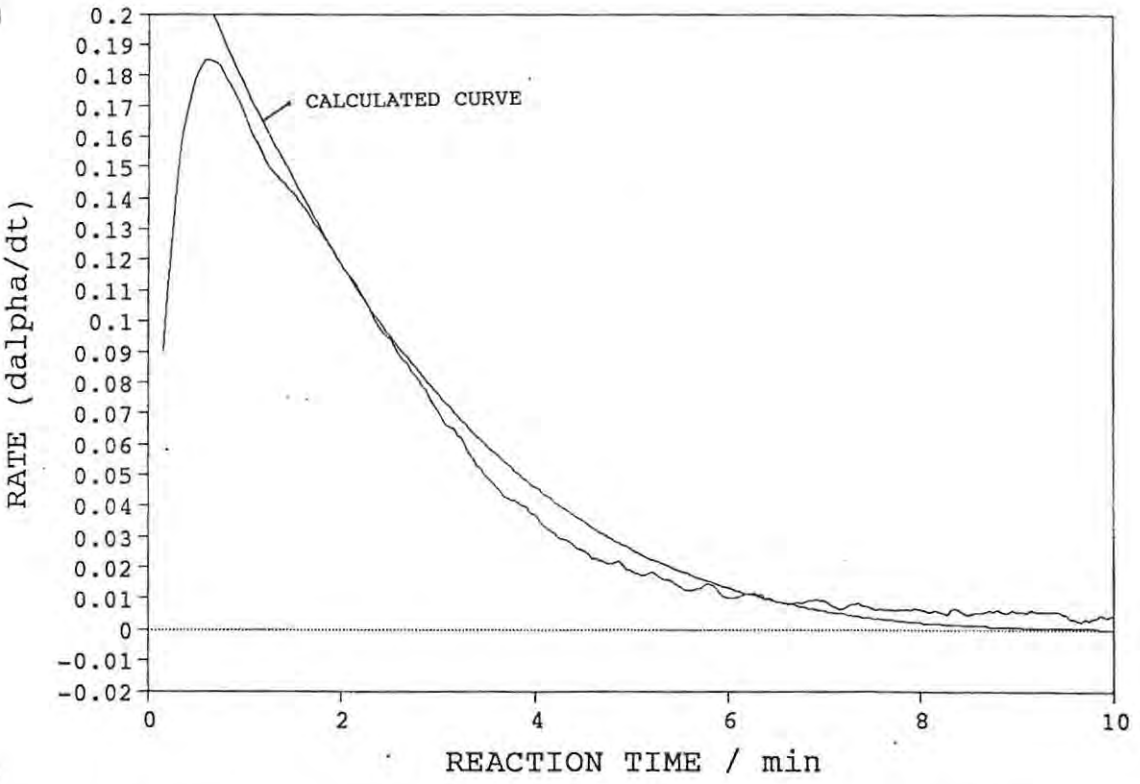

Figure 10.8 Comparison between the calculated $d\alpha_1/dt$ curve and the corrected $d\alpha/dt$ curve at 255°C. k_1 = 0.078 min^{-1}, n = 5, and t_o = -1.42 min

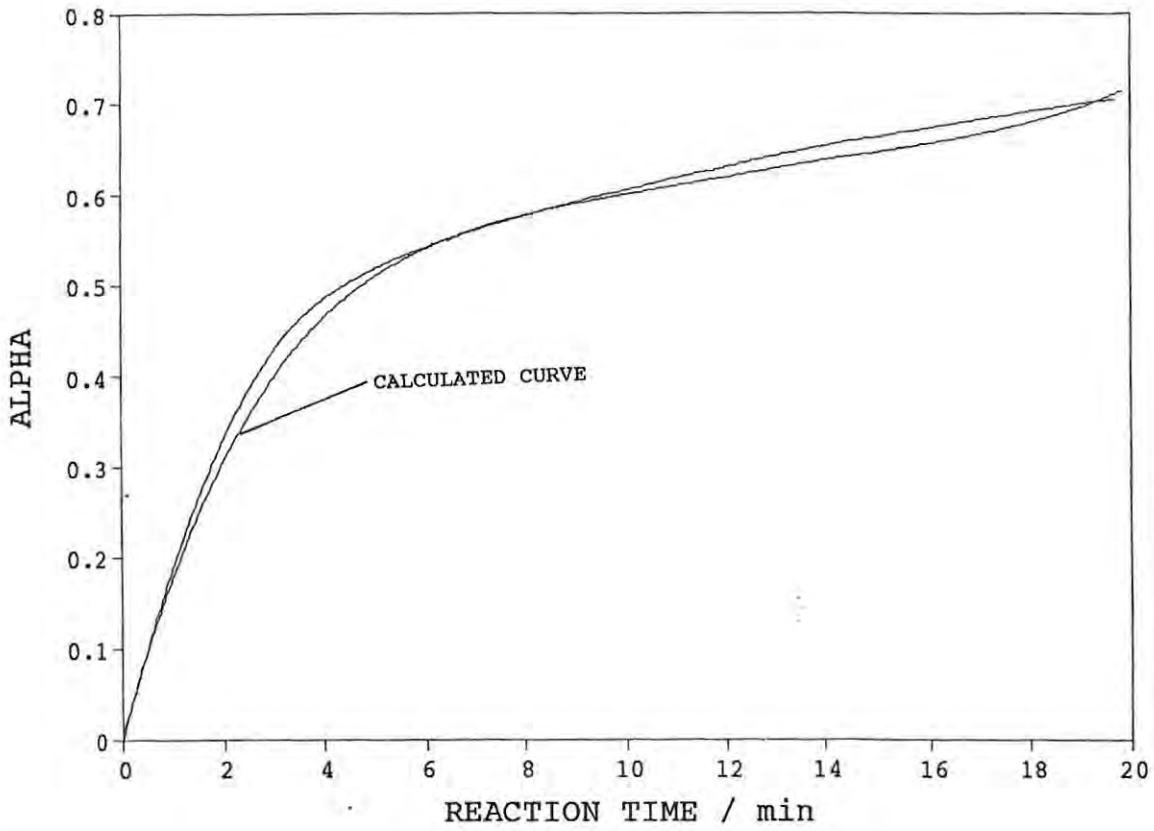

Figure 10.9 Comparison between the calculated and the measured α-time curve at 255°C. k_1 = 0.078 min^{-1}, n = 5, t_o = -1.42 min, k_2 = 0.00087 min^{-1}

Isothermal TG at 235°C

At the low temperature end of the isothermal range used, the acceleratory region, which has been ignored in the kinetic analysis, is more pronounced (Figure 10.10). Only the deceleratory regions can be fitted by the method described above. Linear regression over the time range 30 to 40 minutes gave a slope, m_2 = -1.2 x 10^{-4} and an intercept, c_2 = 8.57 x 10^{-3}. The value for k_2 was estimated from m_2. The rate against time curve was calculated only in terms of process 1. A comparison between the calculated and experimental rate time curve is shown in Figure 10.11 using k_1 = 0.015, n = 5, and t_o = -5.0 min.
An alpha-time curve was calculated using these values. The resulting curve had a similar shape to the experimental curve, but had to be multiplied by a weighting factor, w_1 = 0.5 to improve the fit. Including a contribution from process 2, with w_2 = 0.5, resulted in a better α-time curve. The calculated and experimental α-time curve is shown in Figure 10.12.

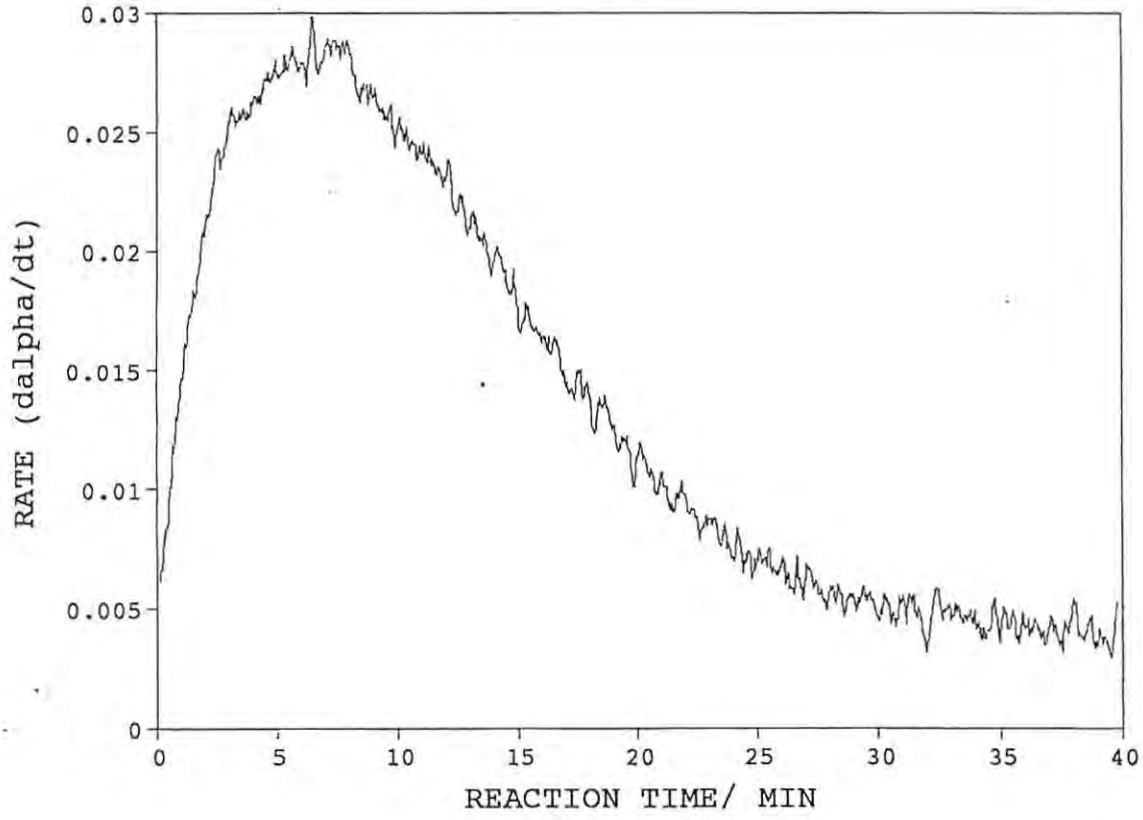

Figure 10.10 Rate of reaction ($d\alpha/dt$) against time for the isothermal experiment at 235°C

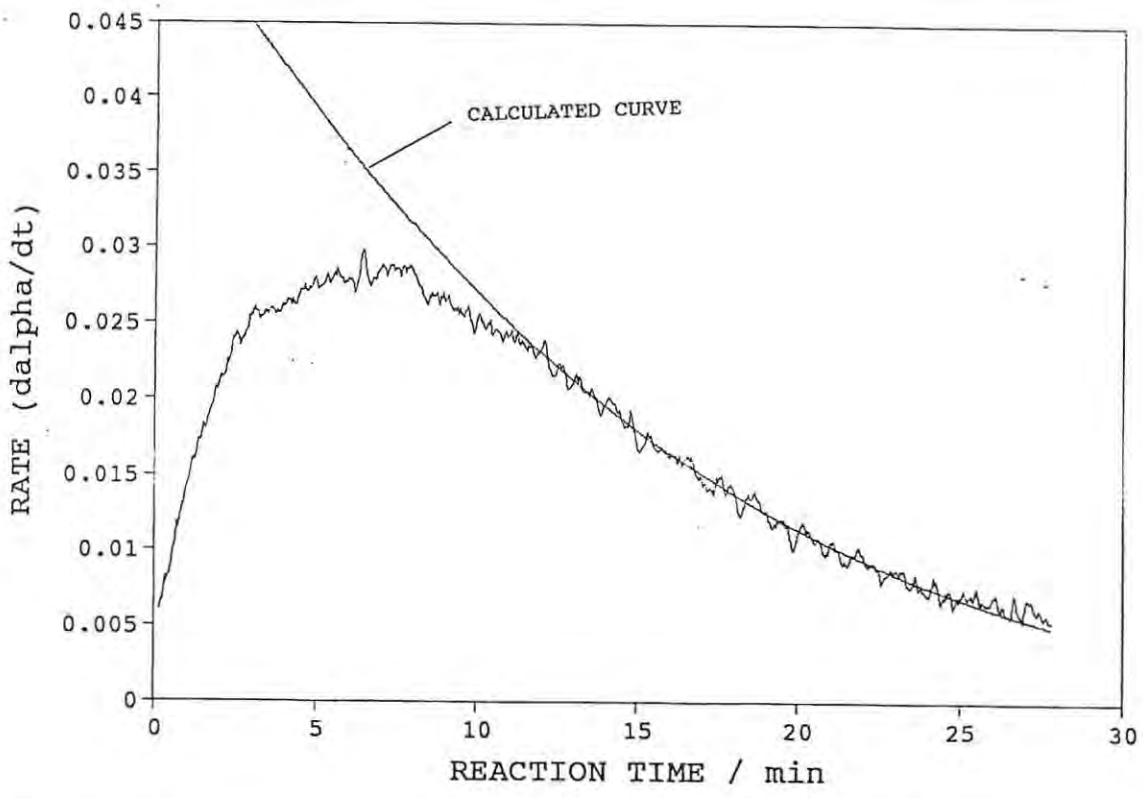

Figure 10.11 The calculated $d\alpha_1/dt$ curve and the corrected $d\alpha/dt$ curve at 235°C. k_1 = 0.017 min^{-1}, n = 5, and t_o= -9 min

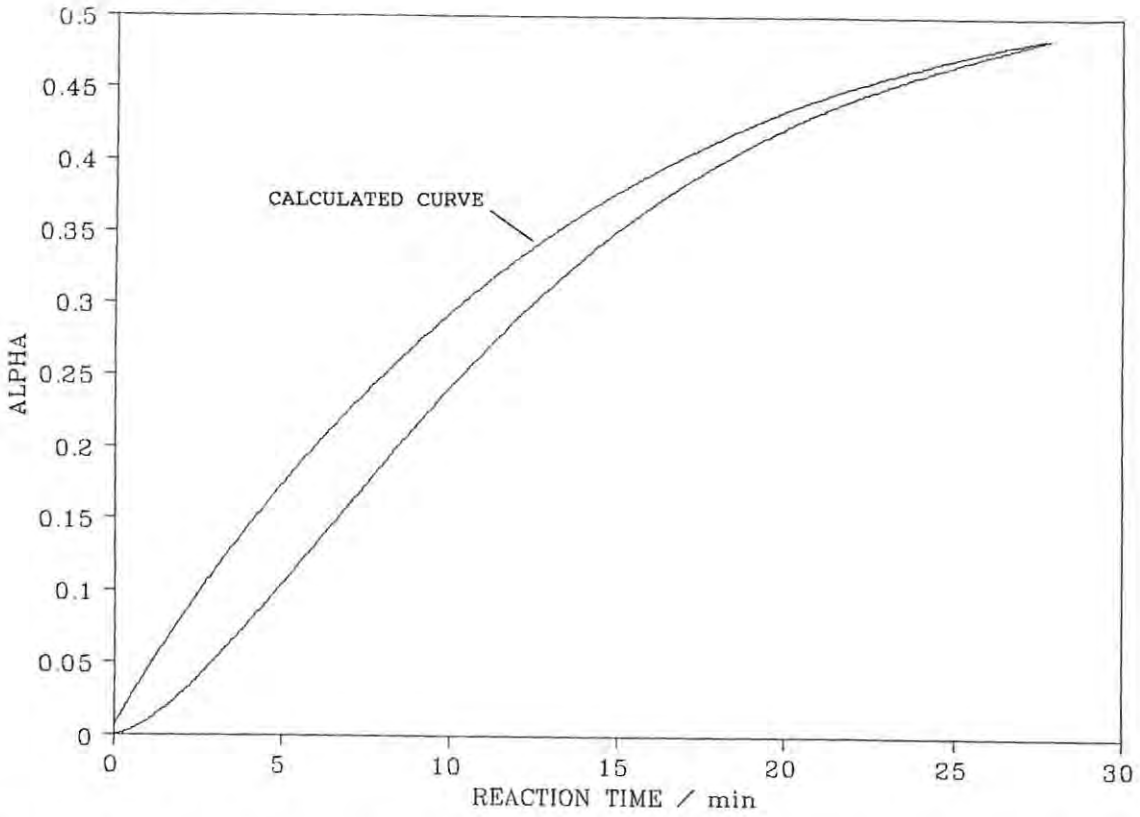

Figure 10.12 Comparison between the calculated and the measured α-time curves at 235°C. k_1 = 0.017 min^{-1}, n = 5, t_o = -5 min^{-1}, k_2 = 0.00012 min^{-1}

Isothermal decomposition at the intermediate temperatures

The isothermal TG experiments at the intermediate temperatures: 240 and 250, as well as at 260°C, were analysed in a similar manner. Brief individual comments follow.

240°C

The $d\alpha/dt$-time curve is shown in Figure 10.13. The contribution from process 2 was initially assumed to be negligible at this low temperature end of the scale and the rate-time curve was analysed only in terms of process 1. After obtaining an approximate fit, introduction of a small contribution from process 2 gave improved agreement between the model and experiment. A comparison is shown in Figure 10.14, using k_1 = 0.029 min^{-1}, n = 5, t_o = 2.0 min, k_2 = 0.0030 min^{-1}. A calculated α-time curve was constructed using w_1 = 0.5, w_2 = 0.6 and t_o = 2.0 min and the result is shown in Figure 10.15.

250°C

The $d\alpha/dt$-time curve is shown in Figure 10.16. Linear regression over the time range 17 to 30 minutes gave a slope, m_2 = -1.1 x 10^{-4} and intercept, $c_2 = 2k_2$ = 1.5 x 10^{-2}. The rate constant, k_2 was estimated from the slope of the regression (k_2 = 7.4 x 10^{-3} min^{-1}). This value for k_2 was used to calculate, and hence subtract, $rate_2$ from the overall rate to give $rate_1$. The plot of $rate_1$ against time is shown in Figure 10.17. The optimised fit occurred when n = 5, k_1 = 0.056 min^{-1}, and t_o = -1.45 min and this is shown in Figure 10.18. The α-time curve was then reconstructed from the two contributions, $rate_1$ and $rate_2$. A good match between the experimental and calculated α-time curves was obtained with the following: w_1 = 0.48, k_1 = 0.056 min^{-1}, t_o = 0 min, n = 5, and w_2 = 0.62, k_2 = 0.0073. This is shown in Figure 10.19.

260°C

Although possibly less reliable, kinetic analysis of an isothermal TG run at 260°C was attempted, to add to the above data. The enlarged $d\alpha/dt$-time curve is shown in Figure 10.20. Linear regression over the time range 5 to 10 minutes gave a slope, m_2 = -0.00207, and intercept, c_2 = 3.16 x 10^{-2}. The rate constant for the slow process, k_2, estimated from m_2 was 3.22 x 10^{-2} min^{-1}. The corrected first-process was fitted approximately by the same model which applied at 240°C and 250°C. The fit with k = 0.19 min^{-1} and t_o = -0.48 min is shown in Figure 10.20. Using the rate constants, determined above, for processes 1 and 2, the overall calculated α-time curve was calculated and is compared with experiment in Figure 10.21.

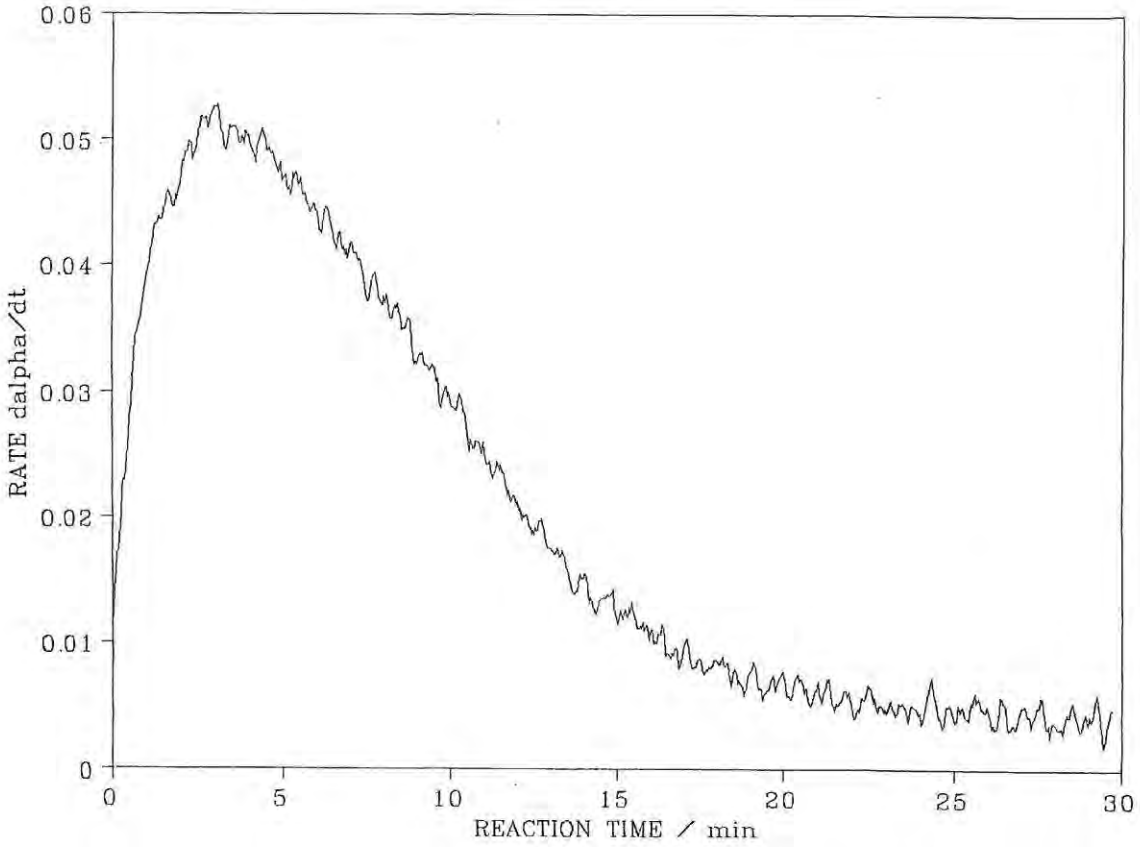

Figure 10.13 Rate of reaction ($d\alpha/dt$) against time at 240°C

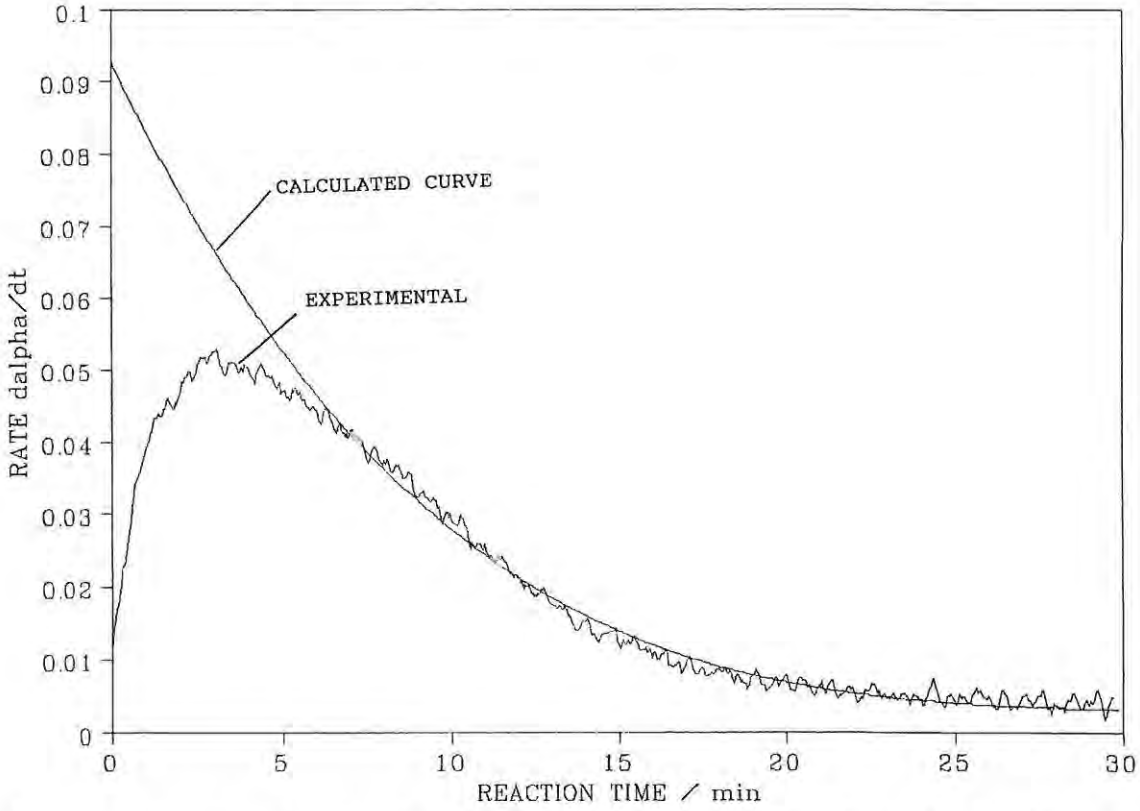

Figure 10.14 Comparison between the calculated $d\alpha_1/dt$ curve using $k_1 = 0.029\ min^{-1}$, $n = 5$, $t_o = 2.0$ min and $k_2 = 0.0030\ min^{-1}$ and the corrected $d\alpha/dt$ curve at 240°C

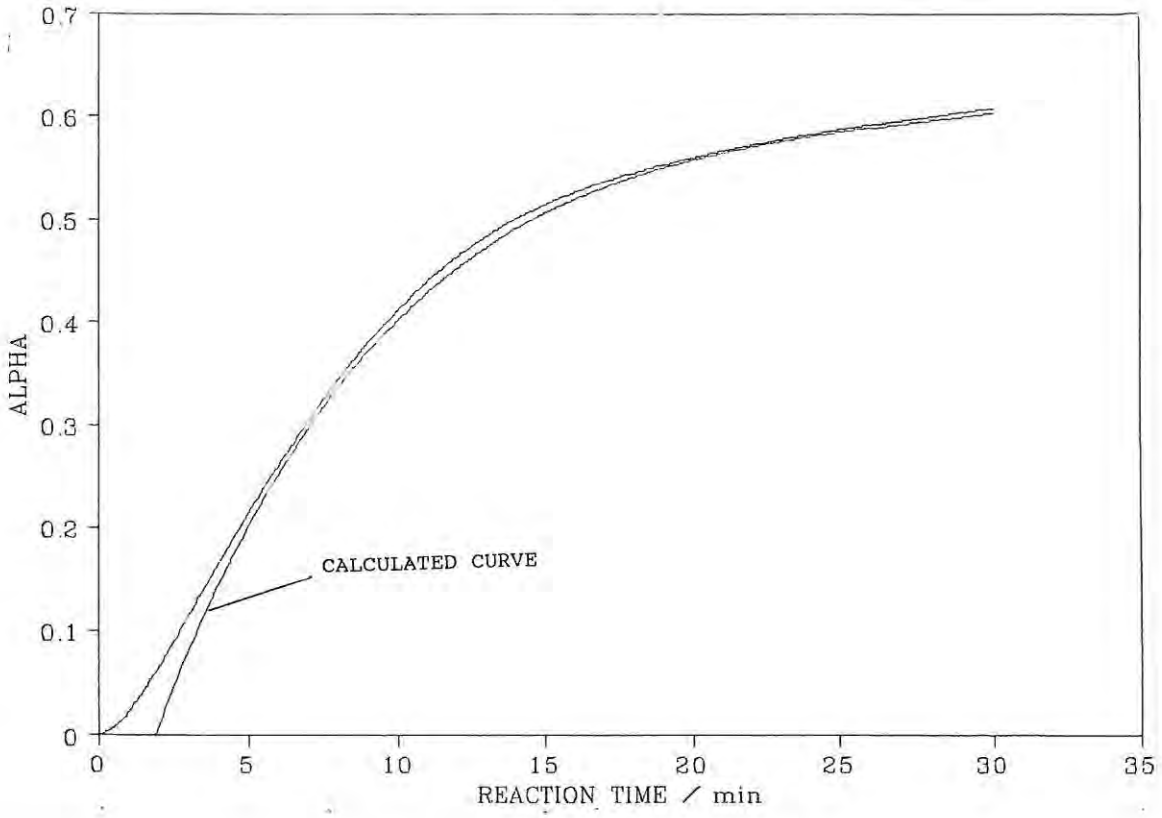

Figure 10.15 Comparison between the calculated α-time curve using k_1 = 0.029 min^{-1}, n = 5, t_o = 2.0 min, k_2 = 0.0030 min^{-1}, w_1 = 0.5 and w_2 = 0.6 and the measured α-time curve at 240°C

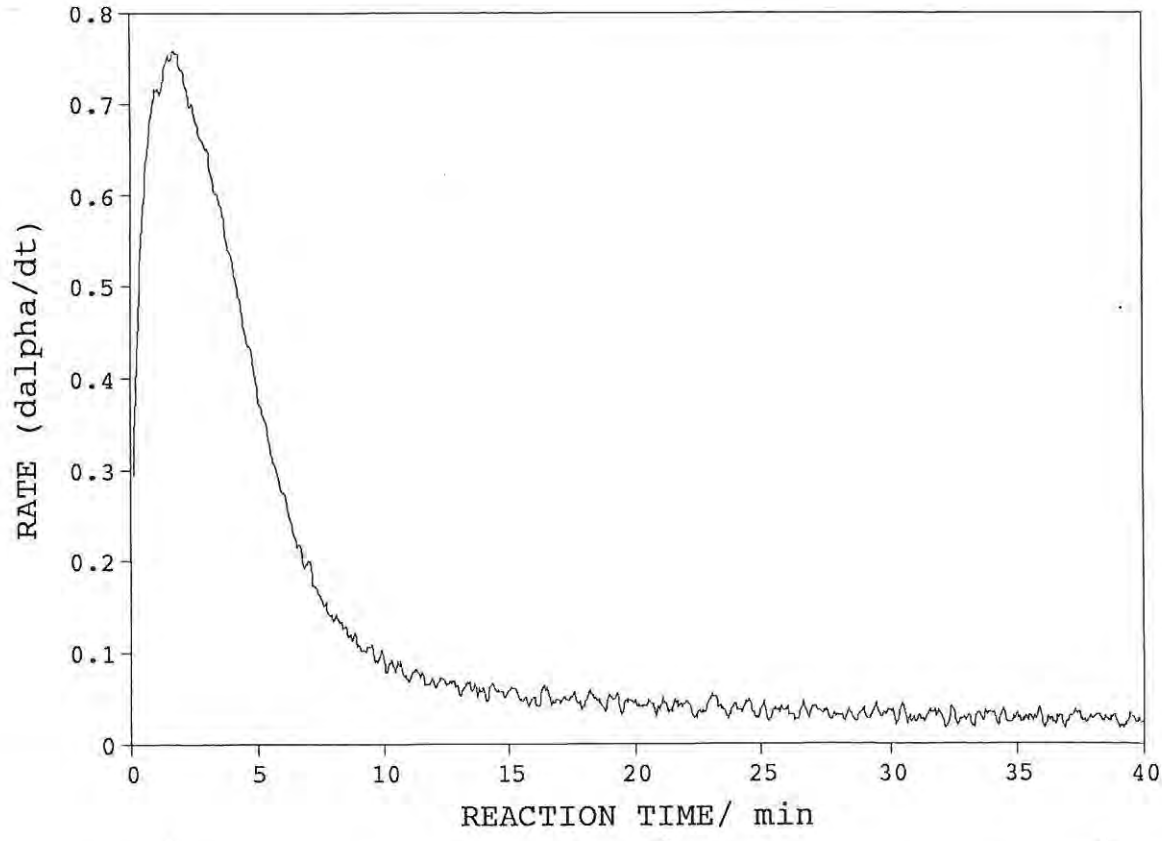

Figure 10.16 Rate of reaction ($d\alpha/dt$) against time at 250°C

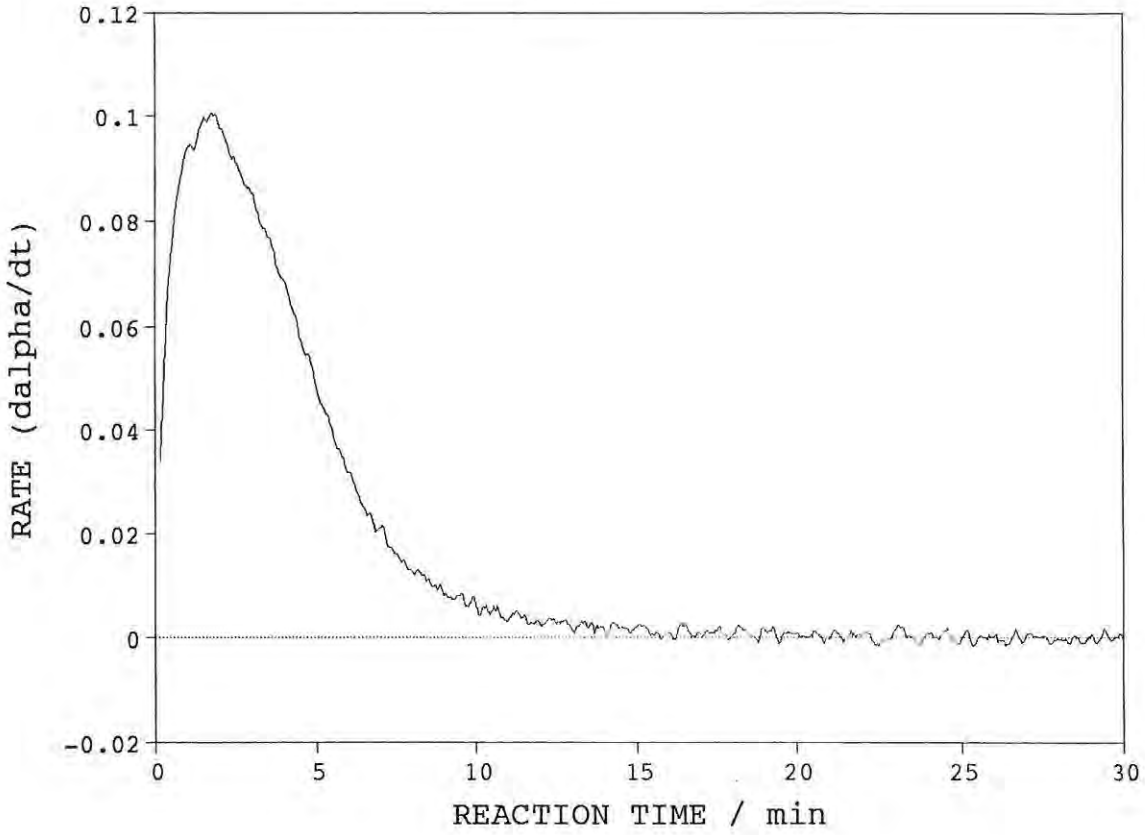

Figure 10.17 Corrected rate of reaction ($d\alpha_1/dt$) against time curve for the experiment at 250°C

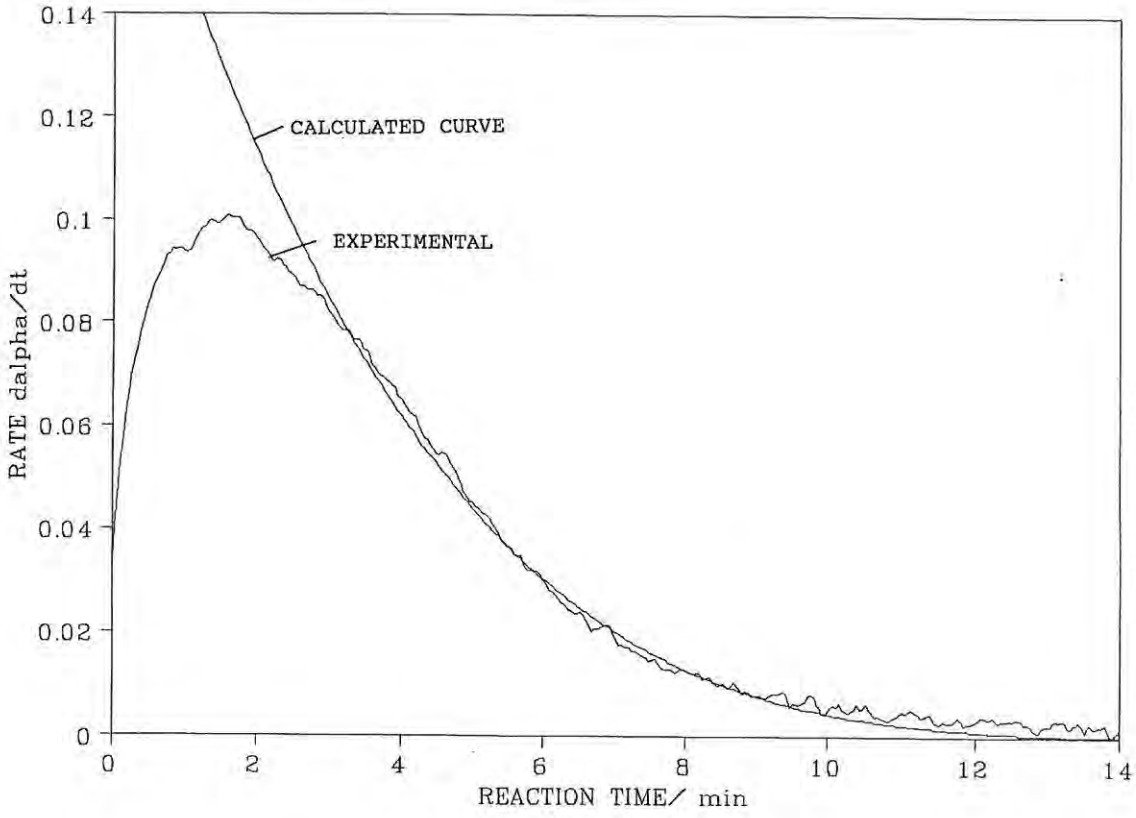

Figure 10.18 The calculated $d\alpha/dt$ against time curve using k_1 = 0.056 min^{-1}, n = 5, t_o = -1.45 min

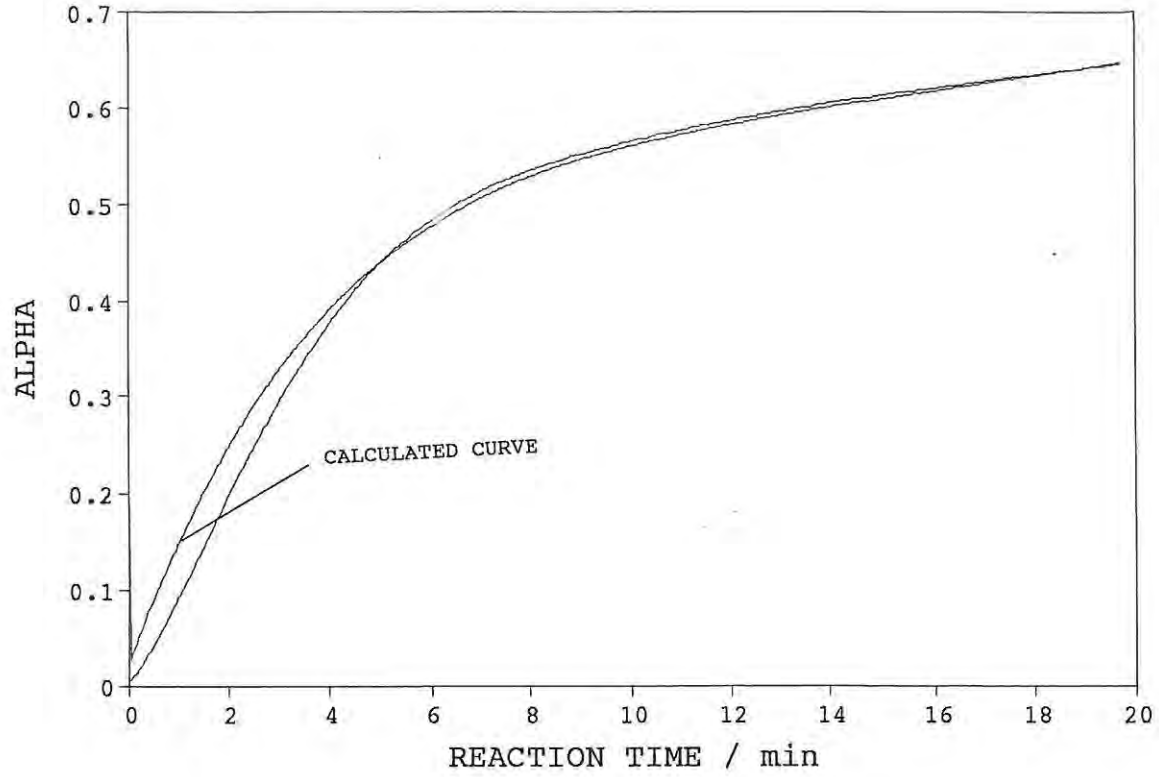

Figure 10.19 Comparison between the calculated and experimental α-time curves at 250°C

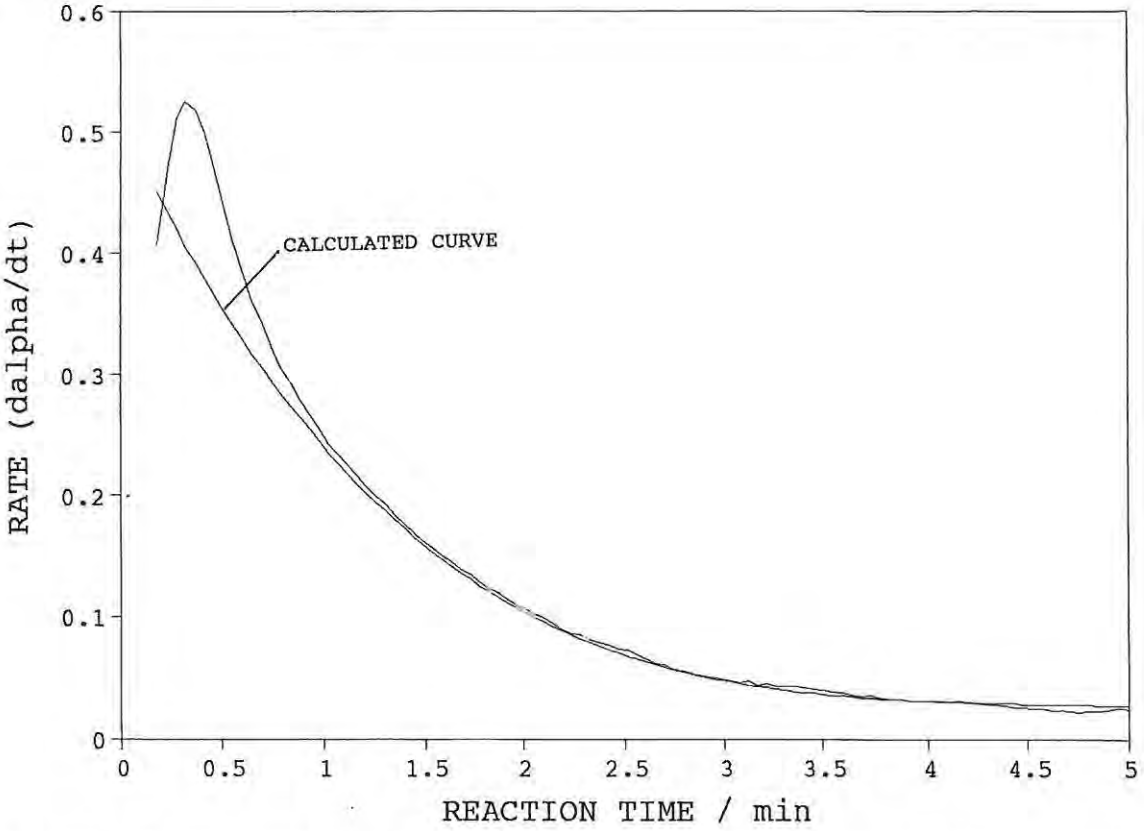

Figure 10.20 Rate of reaction ($d\alpha/dt$) against time curve at 260°C. (The time scale has been expanded).

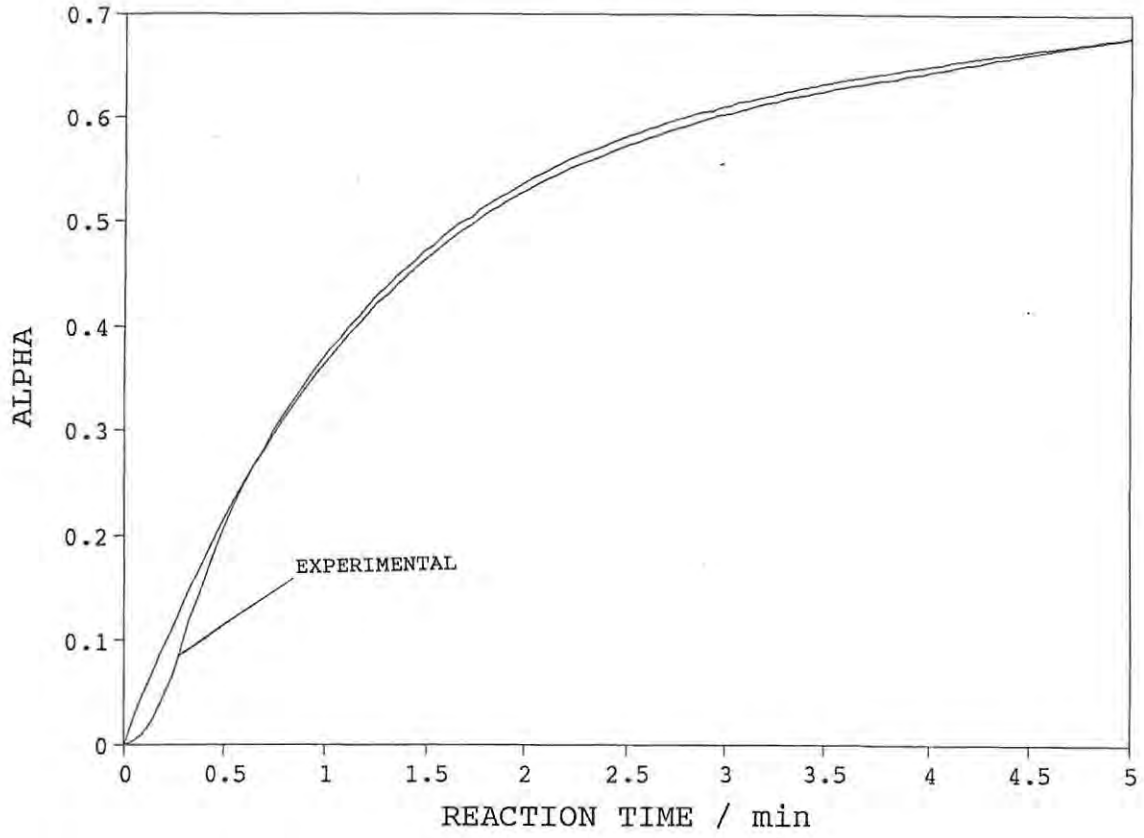

Figure 10.21 Comparison between the calculated and experimental α-time curves at 260°C. k_1 = 0.19 min^{-1}, t_o = -0.48 min, and k_2 = 0.0322 min^{-1}

The kinetic parameters obtained in these isothermal experiments are summarized in Table 10.1.

Table 10.1 Kinetic parameters for the thermal decomposition

T/°C	n	t_o/min	k_1/min^{-1}	k_2/10^{-3} min^{-1}	w_1	w_2
235	5	-5	0.015	1.2	0.5	0.6
240	5	2.0	0.029	3.0	0.5	0.6
250	5	-1.5	0.056	7.4	0.5	0.6
255	5	0	0.078	8.7	0.5	0.6
260	5	-0.48	0.19	32.2	0.5	0.5

The rate constants for the fast process (k_1) and the slow process (k_2) were used in Arrhenius plots (Figure 10.22).

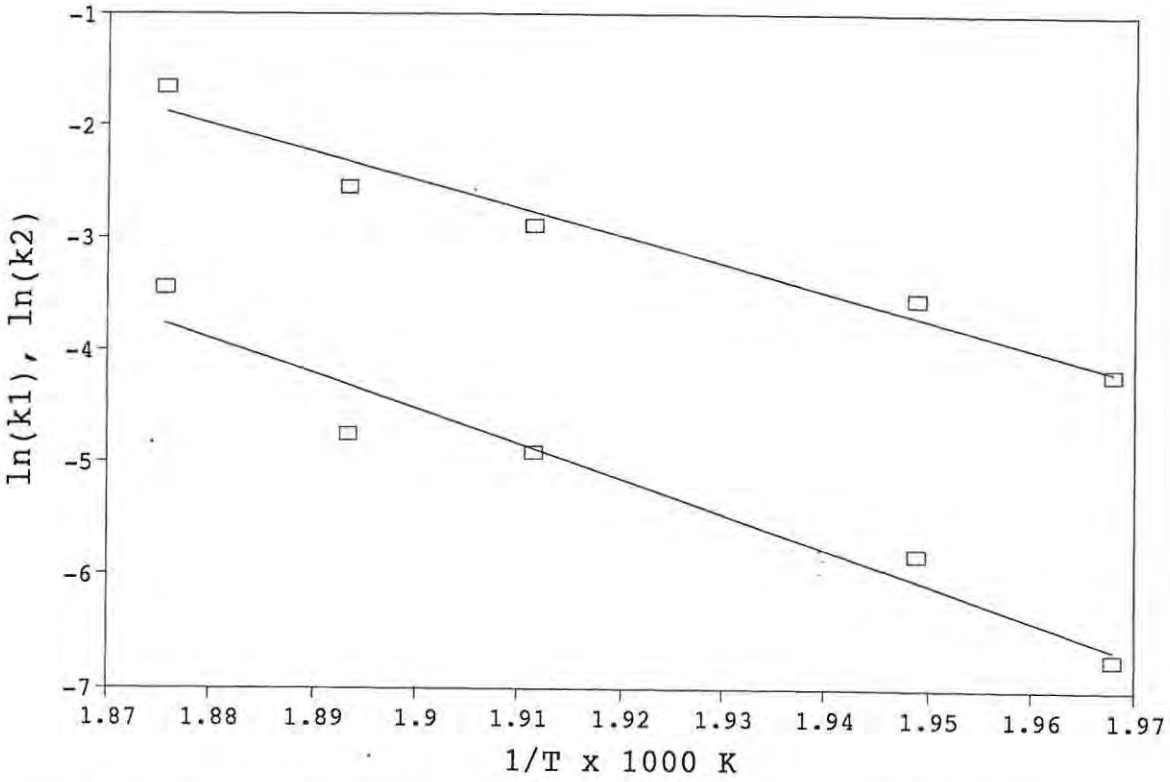

Figure 10.22 Arrhenius plot for the decomposition of $Ba[Cu(C_2O_4)_2(H_2O)].5H_2O$ using k_1 and k_2 (as defined in the text)

The scatter of the points in this plot is very similar to that of the Arrhenius plot based on the slopes of the linear regions of the α-time curves (Figure 10.3). The values of E_a and A were 206 ±23 kJ mol^{-1} and (2.2 ±0.5)x10^{19} min^{-1}, for the fast process, and 259 ±37 kJ mol^{-1} and (6.3 ±1.8)x10^{23} min^{-1} for the slow process.

10.3 Discussion of kinetic analysis

The kinetic analysis described here is more empirical than is usually desirable or necessary. It could be argued that it is not worthwhile to attempt a kinetic analysis of a complex process. An empirical analysis does, however, provide a compact description of complex behaviour, with a certain amount of predictive ability when the kinetic scheme does not differ greatly from one isothermal experiment to another. The Arrhenius parameters, even if they are not identifiable with a specific chemical step, still give a description of observed and expected behaviour on varying the temperature within reasonable limits.

Kinetic analyses of consecutive or concurrent solid state reactions have been attempted, [42], even using non-isothermal experiments.

The concurrent processes considered here are reasonably separable through their differences in rate and their different temperature dependences.

The slow process can be described in terms of the conventional contracting-area model (R2). Applicability of such a model is compatible with the kinetics of the dehydration process and could indicate progress of the reactant/product interface for this decomposition process along similar paths to those followed during removal of water from the hydrate. The prior removal of water would create pores or pathways which could be used, at higher temperatures, for the relatively unhindered removal of decomposition products.

The more rapid concurrent process, after the contribution from the slow process had been subtracted, was not readily describable by the conventional set of kinetic models (Table 9.1).

The empirical model used to describe the faster process:

$d\alpha/dt = nk_1(1 - k_1(t - t_o))^{(n-1)}$

with $n = 5$ and very small values of t_o corresponds then to an α,time relationship of the form

$\alpha = 1 - (1 - kt)^5$

The α,time curve is similar in shape to the other contracting geometry equations. A comparison of the R5 model with the R3 model is shown in Figure 10.23. The comparison is based on $\alpha = 0.98$ for the R3 model at $t = 100$ min. The R5 curve is slightly more sharply deceleratory than the R3 curve but is not as deceleratory as the diffusion models e.g. D3 which is also shown for comparison in Figure 10.23. The D3 model expression is

$\alpha = 1 - [1 - (kt)^{1/2}]^3$

No reference to the use of a value of $n > 3$ for the contracting-geometry model (Rn) was found, but a possible justification for such a value may arise for a system where diffusion and geometric factors are fairly evenly balanced and neither is totally dominant.

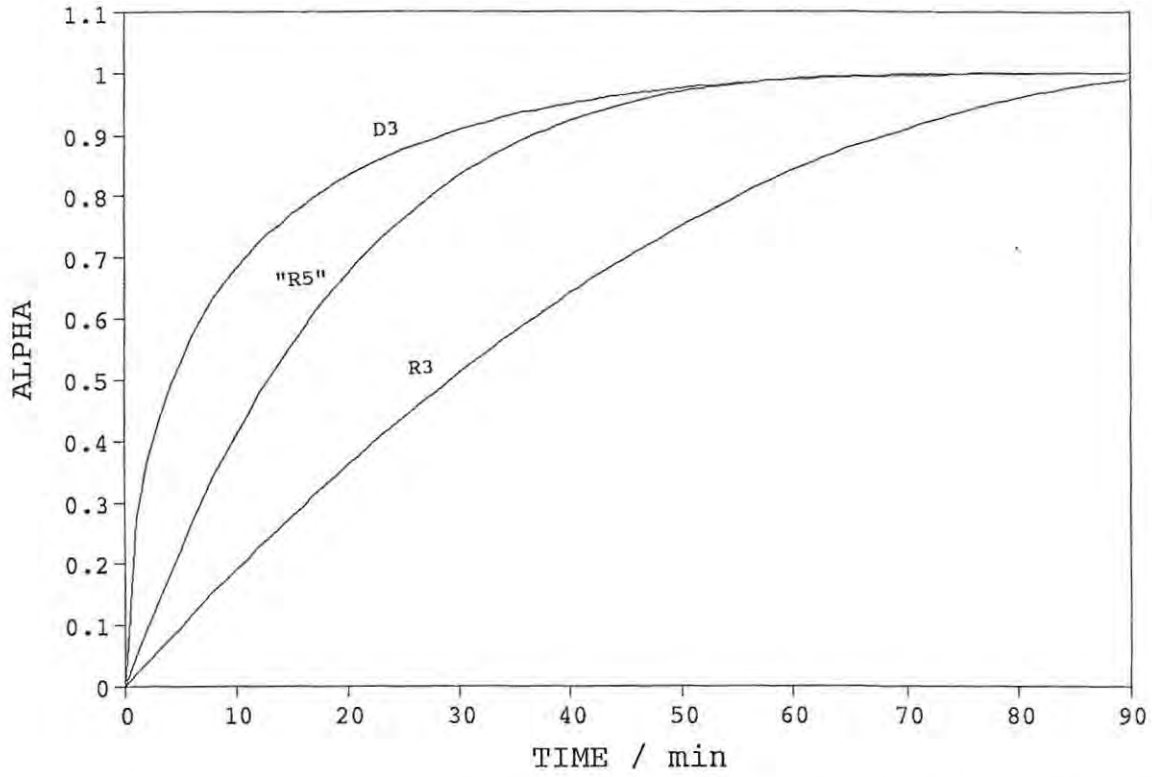

Figure 10.23 Comparison between the R3, "R5", and D3 models. k = 0.010 min^{-1} and t_o = 0 min

Chapter 11

GENERAL DISCUSSION AND CONCLUSIONS

The X-ray diffraction results showed that the structures of the monooxalates ($[M(C_2O_4)(H_2O)_2]_n$ M = Mg, Mn, Fe, Co, Ni, and Zn) are isomorphous. The two complexes, $[Fe(C_2O_4)(H_2O)_2]_n$ and $[Zn(C_2O_4)(H_2O)_2]_n$, were found to be isostructural and nearly identical. Replacing the zinc ion with a larger iron ion results in an increase of the metal-oxygen distances by approximately 3% and a corresponding increase of the unit cell volume by 3.8%.

Electronic spectroscopy shows that the coordination of the metal ions in all of the monooxalates is octahedral, and is similar to the coordination in hexaaqua complexes.

The water content of copper(II) oxalate ranges from 0 to 1 mole per mole of hydrate. The X-ray diffraction pattern of copper oxalate is different to all the other monooxalates.

The kinetics of the dehydration of the monooxalates could be described by the contracting-area (R2) model. This mechanism for the dehydration is consistent with their crystal structures. The water molecules were found to be positioned on the planes (200) and the dehydration conceivably takes place on these planes as a contracting-area reaction. The mixed oxalates ($MCu(C_2O_4)_2.3H_2O$) adopt the structure of $[M(C_2O_4)(H_2O)_2]_n$, and the dehydration also takes place as a contracting-area reaction.

The structures of the dioxalato complexes of copper(II), $M_x[Cu(C_2O_4)_2(H_2O)_y].z(H_2O)$, are complex networks, consisting of dioxalato units bridged by M^{n+} ions. If the metal ion, M^{n+}, interacts covalently with the ligands, then there will no longer be discrete molecules of dioxalato units but covalent polymeric networks. An intermediate compound might be envisaged where M^{n+} has intermediate character and is not clearly covalently or electronegatively bound. There are at least two types of water molecules in these structures, one or two water molecules coordinated to the copper(II) ion, water molecules held to the M^{n+} ion and the oxalate ion, and lattice water.

The X-ray analysis of $Ba[Cu(C_2O_4)_2(H_2O)].5H_2O$ showed that the crystal consists of linear chains of monomeric units of dioxalato copper(II) weakly bridged by barium ions. The barium ions are

surrounded by 9 oxygen atoms. Two of these atoms (O(10) and O(12)) were closer than the sum of the covalent radius of O^{2-} and ionic radius of Ba^{2+}. The coordination geometry of the copper(II) ion could be considered to be square pyramidal with some trigonal distortion. The equatorial positions were occupied by the oxalate ions, and the axial position by a water molecule.

Electronic spectroscopy showed that the overall energy separation of the d-orbitals is smaller in $Ba[Cu(C_2O_4)_2(H_2O)].5H_2O$ than in $Na_2[Cu(C_2O_4)_2].2H_2O$. Thus the amount of Jahn-Teller distortion of the coordination polyhedron of the copper(II) ion is greater in $Na_2[Cu(C_2O_4)_2].2H_2O$.

The dehydration of $Ba[Cu(C_2O_4)_2(H_2O)].5H_2O$ took place at lower temperatures (~90°C) than the monooxalates (typically >140°C). This is because most of the water which is lost is weakly bound to the barium ions, whereas in the monoxalates the water is directly coordinated to the metal ions. During the dehydration, the number of water molecules stabilising the positive charge of the barium ion is decreased. Insausti *et al.* [40] suggest that the dehydration is probably accompanied by the rearrangment of the ligands (oxalate ions and remaining water molecules) about the metal centres.

The kinetics of the isothermal dehydration of $Ba[Cu(C_2O_4)_2(H_2O)].5H_2O$ were strongly deceleratory and could be described by the three-dimensional diffusion (D3) model. The different environments of the water molecules did not appear to influence the kinetics of the isothermal dehydration. The activation energy measured was 125 ±4 kJ mol^{-1} and the pre-exponential factor was 1.38 ±0.08x10^{15} min^{-1}. The onset of the decomposition coincided with the loss of the final traces of water.

The overall enthalpy change for the dehydration, measured from the DSC curves, was 311 ±30 kJ mol^{-1} of complex. This value is substantially larger than the activation energy for the dehydration (125 ±4 kJ mol^{-1}).

From non-isothermal TG, the decomposition of $Ba[Cu(C_2O_4)_2(H_2O)].5H_2O$, in N_2, appeared to take place two stages:

1) $Ba[Cu(C_2O_4)_2](s) \rightarrow BaC_2O_4(s) + Cu(s) + 2CO_2(g)$ (280°C)

2) $BaC_2O_4(s) \rightarrow BaCO_3(s) + CO(g)$ (390°C)

XRD confirmed that $BaCO_3$ was a final product, and IR spectroscopy

showed that BaC_2O_4 is an intermediate of the thermal decomposition. The presence of ionic (barium) carbonate could be detected at temperatures below 390°C. There is some evidence to suggest that the rate-limiting step in the decomposition of copper oxalate is electron transfer from the oxalate ions to the copper ions [21]. In $Ba[Cu(C_2O_4)_2(H_2O)].5H_2O$, electron transfer can concievably take place from the oxalate ions to the copper(II) ions or the barium ions. The barium ion is a very poor electron acceptor compared to the copper(II) ion so electron transfer to the copper(II) ion is more probable. One of the two oxalate groups is positioned more closely to the barium ion and it is thus more likely to be more stable with respect to electron transfer. The C-C bond of the oxalate group which is further away from the barium ion may thus break and release carbon dioxide, while the second oxalate group, positioned more closely to the barium ion, remains intact. At higher temperatures, the second oxalate ion decomposes but, since the barium ion is such a poor electron acceptor, the oxalate decomposition is associated with the formation of barium carbonate.

The DSC curves for the decomposition had several overlapping peaks which indicated that the decomposition was a complex process. The overall decomposition in N_2 was substantially more exothermic than the decomposition of copper(II) oxalate (-331 kJ mol^{-1} compared to -33 kJ mol^{-1}).

The kinetics of the decomposition of copper(II) oxalate are complex, with no single rate law adequately describing the entire decomposition [21].

The kinetics of the decompositions of the mixed metal oxalates ($MCu(ox)_2.3H_2O$) [11] were also complex and the isothermal rate-time curves could be described in terms of several concurrent sigmoid and deceleratory processes. The isothermal rate-time curves for the decomposition $Ba[Cu(C_2O_4)_2(H_2O)].5H_2O$ consisted of concurrent processes, which were separated into a slow process and a fast process. The fast process could not be described by the conventional geometrical models, but the contracting-geometry model, with $n = 5$, gave a good description. The slow process could be described by the conventional contracting-area (R2) model. The α-time curves of all the mixed metal oxalates showed an initial fast process and

a second, slower process ($0.5 < \alpha < 0.8$). The slow process (an overlap of two sigmoidal processes) was deceleratory and could be described by the contracting-volume (R3) equation. Since the later stages of the decomposition of the mixed metal oxalates ($MCu(C_2O_4)_2$), and $Ba[Cu(C_2O_4)_2]$ could be described by the contracting-geometry (R*n*) equation, the Arrhenius parameters for the later stages of all the decompositions are comparable. Arrhenius plots for the second stage of the decompositions of the mixed metal oxalates, $MCu(C_2O_4)_2$, gave activation energies of 155 ±40, 101 ±16 and 91 ±2 kJ mol^{-1} for M = Fe, Co and Ni. An Arrhenius plot for the second, deceleratory process of the decomposition of $Ba[Cu(C_2O_4)_2]$ gave an activation energy of 259 ±37 kJ mol^{-1}.

It is suggested that removal of the bulkier gaseous products of the decomposition (CO_2 and CO) occurs through channels made by the prior dehydration, and that the kinetic behaviour is on the borderline between control by geometrical progression of the reactant/product interface and control by diffusion.

REFERENCES

1. A. Coetzee, D.J. Eve and M.E. Brown, *J. Thermal Anal.*, **39** (1993) 947

2. S. Caric, *Bull. Soc. Franc. Miner. Crist.*, 82 (1959) 50

3. J.P. Lagier, H.P. Pezerat and J. Dubernat, *Rev. Chim. Miner.*, 6 (1969) 1081

4. A. Michalowicz, J.J Girerd and J.Goulon, *Inorg. Chem.*, 18 (1979) 3004

5. S. Emori and K. Todoko, *Bull. Chem. Soc. Japan*, 66 (1993) 3513

6. H. Schmittler, *Monatsh. Deut. Akad. Wiss. Berlin*, 10 (1968) 581

7. A. Gliezes, F. Maury and J. Galy, *Inorg. Chem.*, 19 (1980) 2074

8. M. A. Viswamitra, *J. Chem. Phys.*, 37 (1962) 1408

9. J.H. Ammeter, H.B. Burgi, E. Gamp, V. Meyer-Sandrin and W.P. Jensen, *Inorg. Chem.*, 18 (1979) 733

10. Y. Masuda, K. Iwata, R. Ito and Y. Ito, *J. Phys. Chem.*, 91 (1987) 6543

11. A. Coetzee, D.J. Eve, M.E. Brown and C.A. Strydom, *J. Therm. Anal.*, 41 (1994) 357

12. H. Ellis, R.D. Harrison and H.D.B. Jenkins (Eds), "Revised Nuffield Advanced Science Book of Data", Longman Limited, Essex, 1986

13. J.E. House and L.A. Marquadt, *J. Solid State Chem.*, 89 (1990) 155

14. D.A. Dominey, H. Morely and D.A. Young, *Trans. Faraday Soc.*, 61 (1965) 1246

15. I.A. Kahwa and A.M. Mulokozi, *J. Thermal Anal.*, 24 (1982) 265

16. E.D. Stevens and P. Coppens, *Acta Cryst.*, *B*36 (1980) 1864

17. H. Kuppers, *Acta Cryst.*, *B*29 (1973) 318

18. T.C.W. Mak and G-D Zhou, "Crystallography in Modern Chemistry: A Resource Book of Crystal Structures", pp 291-296, John Wiley & Sons, New York, 1992

19. A.H. Verdonk and A. Broersma, *Thermochim. Acta*, 6 (1973) 95

20. N. Koga and H. Tanaka, *J. Thermal Anal.*, 32 (1987) 1521

21. M.A. Mohamed and A.K. Galwey, *Thermochim. Acta*, 213 (1993) 269

22. P.K. Gallagher, P.T. Chao, L. Zhong and J. Subramanian, *J. Thermal Anal.*, 39 (1993) 975

23. R.M. Clarke and I.R. Williams, *Min. Mag.*, 50 (1986) 295

24. G.M. Sheldrick, SHELX-76, Program for Crystal Structure Determination, University of Cambridge, UK, 1976

25. S. Motherwell, PLUTO, Program for Molecular Drawings, Cambridge, UK

26. F.L. Lee, Y. Le Page, M. Webster, J.P. Charland and E.J. Gabe, NRC VAX CRYSTAL STRUCTURE SYSTEM, Chemistry Division, National Research Council, Ottawa, Canada, KIA OR6

27. K. Nakamoto, "Infrared Spectra of Inorganic Coordination Compounds", Second Edition, p 244, John Wiley & Sons, New York, 1970

28. R. Krishnamurthy and W.B. Schaap, *J. Chem. Ed.*, 46 (1969) 799

29. J.J. Alexander, B. Douglas, D.H. McDaniel, "Concepts and Models of Inorganic Chemistry", Second Edition, John Wiley and Sons, New York, 1983

30. J.E. Huheey, "Inorganic Chemistry: Principles of Structure and Reactivity", Third Edition, Harper & Row, New York, 1983

31. P. Luger, "Modern X-ray Analysis on Single Crystals", p 66, Walter de Gruyter, Berlin, 1980

32. D.T. Cromer and J.T. Waber, "International Tables of X-ray Crystallography", Vol.4, Kynoch, Birmingham, 1974

33. A.F. Wells, "Structural Inorganic Chemistry", 3rd Edition, Clarendon Press, Oxford, 1962

34. L.V. Azaroff, M.J. Buerger, "The Powder Method in X-ray crystallography", McGraw-Hill, London, 1958

35. F.D. Rossini, D.D. Wagman, W.H. Evans, S. Levine and I. Jaffe, "Selected Values of Chemical Thermodynamic Properties", Circular of National Bureau of Standards 500, United States Government Printing Office, Washington D.C., 1952

36. J.V. Smith (Ed), "Powder Diffraction File: Sets 1-5", American Society for Testing And Materials, Philadelphia, 1969

37. R.A. Nyquist and R.O. Kagel, "Infrared Spectra of Inorganic Compounds (3800-45 cm^{-1})", Academic Press, London, 1971

38. S.F. Hulbert, *J. Br. Ceram. Soc.*, 6 (1969) 11-20

39. W-L Ng, C-C Ho and S-W Ng, *J. inorg. nucl. Chem.*, 34 (1978) 459

40. M. Isausti, M.K. Urtiaga, R. Cortes, J.L. Mesa, M.I. Arriortua and T. Rojo, *J. Mater. Chem.*, 4 (1994) 1867

41. S. Vyazovkin, *Thermochim. Acta.*, 223 (1993) 201